TENSOR BASED ANALYSIS OF DIFFUSION WEIGHTED MAGNETIC RESONANCE IMAGES

by

Yonas Tesfazghi Weldeselassie

M.Sc., The Abdus Salam International Center for Theoretical Physics, 2004

B.Sc., University of Zimbabwe, 2002

A Thesis submitted in partial fulfillment
of the requirements for the degree of

Doctor of Philosophy

in the
School of Computing Science
Faculty of Applied Sciences

SIMON FRASER UNIVERSITY
Spring 2012

APPROVAL

Name: Yonas Tesfazghi Weldeselassie

Degree: Doctor of Philosophy

Title of Thesis: Tensor Based Analysis of Diffusion Weighted Magnetic Resonance Images

Examining Committee:

Dr. Anoop Sarkar
Associate Professor
Chair

Dr. M. Stella Atkins, Senior Supervisor
Professor

Dr. Mirza Faisal Beg, Supervisor
Associate Professor, School of Engineering Science

Dr. Manfred Trummer, Supervisor
Professor, Department of Mathematics

Dr. Torsten Möller, Internal Examiner
Professor

Dr. Kaleem Siddiqi, External Examiner
Professor, School of Computer Science
McGill University, Montreal, PQ, Canada

Date Approved: March 22, 2012

Partial Copyright Licence

Abstract

Diffusion Weighted Magnetic Resonance Imaging (DW-MRI) is a non-invasive and in vivo medical imaging technique that allows neural tissue architecture to be probed at a microscopic scale. This is possible due to the diffusion of hydrogen atoms within water molecules in the imaging body; thus capturing the microstructure of the underlying tissues. DW-MRI adds to conventional MRI the capability of measuring this diffusion of water molecules by applying strong magnetic field along several gradient directions in order to measure the apparent diffusion coefficients along those directions.

In this thesis, we look at modeling diffusion of water molecules with Cartesian Tensors: a model known as Diffusion Tensor Magnetic Resonance Imaging (DT-MRI). We begin with 2^{nd} order tensor model which results in an image where at each voxel the preferred direction of diffusion is locally modeled by a 3×3 symmetric positive definite matrix whose coefficients are estimated from the DW-MR data. After briefly reviewing anisotropy and distance measures of 2^{nd} order tensors, we extend these ideas to develop a novel anisotropy measure. Tensor distance measures are then used to extend scalar image segmentation algorithms in order to segment tensor images. Next, we present a clinical application of DT-MRI to investigate various features of white matter fiber tracts in the cortico-striatal region of the brain for the diagnosis of Parkinson's disease. Finally, we investigate the limitations of the 2^{nd} order tensor model and extend it to higher order tensors in order to correctly depict crossing fiber tracts. In particular, we develop a new technique to model fiber orientation distribution functions using higher order tensors and develop a novel anisotropy measure derived directly from fiber orientation distribution functions.

Keywords: Diffusion Weighted Magnetic Resonance Imaging; Diffusion Tensor Magnetic Resonance Imaging; Fractional Anisotropy; Shape Anisotropy; Cartesian Tensor Fiber Orientation Distribution

To my parents; for all your prayers from far away in Asmara, Eritrea.

"Look at a stone cutter hammering away at his rock, perhaps a hundred times without as much as a crack showing in it. Yet at the hundred-and-first blow it will split in two, and I know it was not the last blow that did it, but all that had gone before."

— *Jacob A. Riis*

Acknowledgments

This thesis would not have been possible without the guidance and help of several individuals who in one way or another contributed and extended their valuable assistance throughout my studies. First and foremost I owe my deepest gratitude to my senior supervisor, Dr. M. Stella Atkins, whose steadfast encouragement, guidance and support from the beginning to the end enabled me to complete my studies successfully. Dr. Stella, your firm conviction in my ability to do mathematically oriented scientific research has been the greatest driving force during my studies and it has opened doors that I never thought would be possible. Having you as my senior supervisor not only was it an unmatchable opportunity for my personal growth, but also it was the most exciting and enjoyable time of my life. For this, I thank you.

Next, I would like to thank Dr. Angelos Barmpoutis at Digital Arts and Sciences, University of Florida, Digital Worlds Institute for the best collaboration I had with you. Not only have you guided me to make such a beautiful and memorable contribution in my field but also opened my horizon to look far and beyond my local neighborhood. Angelos, your excellent fanDTasia matlab code deserves recognition for both its simplicity and complexity. Simple to understand and use but complex enough to do crazy stuff.

Thank you my professors Dr. Mirza Faisal Beg, Dr. Manfred Trummer, and Dr. Ghassan Hamarneh who have made valuable input during my studies. Equally important was your support in getting different datasets from other researchers. I thank Dr. Martin McKeown, Dr. Steven Miller, and Dr. Alexander Rauscher from University of British Columbia for your collaboration and for providing me datasets partially used in my research. My collaboration with you all have helped me deeper my understanding of human brain anatomy and to apply my computational knowledge to real problems like tissue classification and Parkinson's disease analysis. Special thanks also goes to my Professor Dr. Anoop Sarkar for all your

help during my stay at SFU. It was an honor to have you as the chair person during my thesis defence.

My friends Dr. Paul Wighton, Vinay Kotamraju, Bethelhem Mengesha, and soon to be both Dr. and Assistant Professor Usman Alim; you have been like my family pillars while I am far away from home. I don't have enough words to express my blessings to have had you on my side through cold and hot. Our support to one another and our crazy discussions regarding our research work, future perspectives, families, relationships and everything in life was quite remarkable and memorable. I also thank all members of our lab for our valuable discussions throughout my stay.

Let me also take this opportunity to thank Laboratory of Brain Anatomical MRI and Center for Imaging Science at Johns Hopkins University for providing free public DTI datasets and excellent software DTI Studio; Dr. Bennett Landman at Johns Hopkins University School of Medicine, Department of Biomedical Engineering, Image Analysis and Communications Laboratory for your publicly available Coregistration, Adjustment, and Tensor-solving a Nicely Automated Program (CATNAP) software tool; and Dr. Alexander Leemans at University Medical Center Utrecht, Image Sciences Institute, Department of Radiology, The Netherlands for your freely available ExploreDTI software that I have used throughout my studies. Thank you Jennifer Campbell, research associate of the McConnell Brain Imaging Centre, Montreal Neurological Institute, McGill University for generously providing me brain datasets; Dr. Yuri Boykov and Dr. Vladimir Kolmogorov for your publicly available Maximum Flow Minimum Cut software; Dr. Leo Grady for your Random Walker Algorithm; and many many other researchers whose software tools or datasets I have used during my studies. Thank you all.

Finally, I thank God for giving me such a blessed life.

Contents

List of Figures

Glossary

ADC Apparent Diffusion Coefficient. 1, 4, 13, 14, 20, 65, 68, 69, 77, 80, 83

AI Anisotropy Index. 35, 36, 69, 75–77, 79

CT-FOD Cartesian Tensor Fiber Orientation Distribution. 68, 69, 72–75, 77–80, 83

DIV Divergence. 62

DOT Diffusion Orientation Transform. 66, 67, 78

DSI Diffusion Spectrum Imaging. 66

DT-MR Diffusion Tensor Magnetic Resonance. 3, 4, 6, 11, 13, 16, 20, 21, 23, 32, 40–43, 46–49, 51, 54, 56, 57, 59, 62, 84, 85

DT-MRI Diffusion Tensor Magnetic Resonance Imaging. 3, 9, 16, 21, 22, 27, 38, 42, 49, 58, 69, 83–85

DTI Diffusion Tensor Imaging. 3, 4, 58–60, 62, 64

DW-MR Diffusion Weighted Magnetic Resonance. 3, 4, 6, 20, 65, 68, 69, 71–73, 76, 77

DW-MRI Diffusion Weighted Magnetic Resonance Imaging. 1–3, 6, 20, 67, 83–86

DWI Diffusion Weighted Images. 2, 5, 6, 8

EPI Echo Planar Imaging. 5, 21

FA Fractional Anisotropy. 12, 13, 19, 22–25, 28, 31, 32, 34–36, 38, 49, 57–60, 62, 64, 75–77, 84

FACT Fiber Assignment by Continuous Tracking. 16

FMM Fast Marching Method. 16

fMRI Functional Magnetic Resonance Imaging. 59

FOD Fiber Orientation Distribution. 3, 4, 67–69, 75, 77, 78, 83, 85

FOV Field of View. 32, 79

GA Generalized Anisotropy. 76, 77, 79, 80

HARDI High Angular Resolution Diffusion Imaging. 3, 66, 79

HOT Higher Order Tensor. 3, 4, 68–70, 73, 74, 83

LLS Linear Least Squares. 9

MD Mean Diffusivity. 13, 14, 19, 59, 62, 64

MNI Montreal Neurological Institute. 35

MR Magnetic Resonance. 2, 5, 65, 76, 77

MRI Magnetic Resonance Imaging. 1, 3, 21, 58, 68

NNLS Non-Negative Least Squares. 72, 73

ODF Orientation Distribution Function. 66–69, 83, 85

PD Parkinson's Disease. 4, 58, 59, 62, 64, 84, 85

PDF Probability Distribution Function. 66–68, 78

QBI Q-ball Imaging. 66–68, 78

RA Relative Anisotropy. 12, 13, 24, 35, 36

ROI Region of Interest. 59, 60

SA Shape Anisotropy. 32, 34, 35

SNR Signal to Noise Ratio. 13, 23, 24, 35, 36, 38, 84

SPD Symmetric Positive Definite. 3, 6, 9, 17, 22, 25, 26, 68, 70, 83

Chapter 1

Introduction

In their commentary titled "Backwardness of human neuroanatomy" to Nature Journal in 1993, Francis Crick and Edward Jones said that "To interpret the activity of living human brains, their neuroanatomy must be known in detail. New techniques to do this are urgently needed, since most of the methods now used on monkeys cannot be used on humans."

Who would have thought only a year later would a new imaging technique be widely used within the Magnetic Resonance Imaging (MRI) community to address this urgency? That is exactly what Peter Basser, James Mattiello, and Denis Le Bihan achieved with their seminal work titled "Estimation of the effective self-diffusion tensor from the NMR spin echo" [14]. They developed what is now termed Diffusion Weighted Magnetic Resonance Imaging (DW-MRI): a non-invasive and in vivo (occurring or made to occur within a living organism or natural setting) imaging technique that allows neural tissue architecture to be probed at a microscopic scale thanks to the random motion of hydrogen atoms within water molecules in all three dimensions in the human body; thus capturing the microstructure of the underlying tissues [27, 71, 15, 69].

Individual water molecules at temperatures above $0\,^{\circ}\mathrm{K}$ are constantly in motion, colliding with each other and with other molecules in tissues at high speeds. These high-speed collisions cause the water molecules to spread out randomly. DW-MRI adds to conventional MRI the capability of measuring this random motion of water molecules, called diffusion. This is achieved by applying a strong magnetic field along several gradient directions in order to measure the Apparent Diffusion Coefficient (ADC) along those directions at each voxel in the imaging body.

While DW-MRI technology provides new information about the state of many tissues

within the body, it is particularly useful in identifying the neural connectivity patterns of the human brain allowing us to distinguish between anatomical structures of the cerebral white matter such as the corpus callosum, the superior longitudinal fasciculus or the cortico-spinal fiber tracts [84, 79, 91, 16, 30, 58, 63, 70]. DW-MRI is also informative when imaging fibrous tissues such as tendons (a band of tough, fibrous, inelastic tissues made chiefly of collagen that connect a muscle to a bone) and ligaments (a sheet or band of tough, fibrous tissue connecting bones or cartilages at a joint or supporting an organ).

The inventors of DW-MRI [1], describe the success of DW-MRI as deeply rooted in the powerful concept that during their diffusion-driven random displacements, water molecules probe tissue structures at a microscopic scale well beyond the usual image resolution. During typical diffusion times of about 50 to 100 $msec$, water molecules move in the brain on average over distances around $10\mu m$ bouncing, crossing, or interacting with many tissue components such as cell membranes, fibers or macromolecules. The overall effect observed in a DW-MRI image voxel of several mm^3 reflects, on a statistical basis, the displacement distribution of the water molecules present within this voxel. The observation of this displacement distribution thus provides unique clues to the structure and geometric organization of tissues. It is now well established that the Magnetic Resonance (MR) measurement of an effective diffusion of water in tissues can provide unique biologically and clinically relevant information that is not available from other imaging modalities. This information includes parameters that help characterize tissue composition, the physical properties of tissue constituents, tissue microstructure and its architectural organization.

Once several Diffusion Weighted Images (DWI) are acquired, we may proceed either to analyze the images directly or we may opt to model diffusion at each voxel with certain functions whose parameters are estimated from the DWI data. Analyzing the DWI directly is not convenient as each image contains little information. Combining all the DWI in some way is therefore required in order to get optimal advantage from DW-MRI. Noting that diffusion of water molecules in the body would be spherical if no barriers were present, it therefore makes sense to model diffusion with spherical functions that reflect the presence or absence, and if present, the shape of barriers that hinder the diffusion. The two most commonly used frameworks for spherical function representations are Cartesian tensors [15] and spherical harmonics [107].

[1] A good text on the history of the development of DW-MRI can be found at [41].

The Cartesian tensor representation is a simple model first developed for single fiber reconstruction using second order tensors and has given rise to the research area known as Diffusion Tensor Imaging (DTI) [15]. As few as only six gradient directions are enough to reconstruct diffusion tensor images that enable us to generate fiber tracts in fibrous tissues. Recently, the DTI model has been extended to the Higher Order Tensor (HOT) model in order to address the limitation of the DTI model in regions containing intra-voxel orientational heterogeneity such as crossing and merging of fiber bundles by acquiring more Diffusion Weighted Magnetic Resonance (DW-MR) images [86].

The spherical harmonics representation on the other hand requires acquisition of high angular resolution diffusion images primarily developed to enable a precise angular characterization of the diffusion signal for multi-fiber reconstruction purposes, while keeping the acquisition time compatible with clinical constraints. This model, known as High Angular Resolution Diffusion Imaging (HARDI), is developed to address the limitation of the DTI model in regions containing intra-voxel orientational heterogeneity such as crossing and merging of fiber bundles [107]. This model, however requires acquisition of high angular resolution diffusion images which in turn requires advanced scanners and has become popular only recently. It was not a mature research topic when this thesis was started and therefore is not covered in the thesis. Previous work on HARDI is presented as an introduction in Chapter 6 of the thesis where we present the HOT model representation of Fiber Orientation Distribution (FOD) functions. See also [56] for comprehensive reference material on diffusion MRI.

The thesis therefore focuses at modeling of diffusion of water molecules with Cartesian Tensors and develops tools for processing and analysis of tensor images reconstructed from DW-MRI. Such a model has given rise to the research field referred to as Diffusion Tensor Magnetic Resonance Imaging (DT-MRI) or DTI for short. The high dimensional nature of Diffusion Tensor Magnetic Resonance (DT-MR) images, $3\mathbf{D}$ volume images with a 3×3 Symmetric Positive Definite (SPD) matrix at each voxel, requires some processing to visualize on conventional $2\mathbf{D}$ display devices. What relevant information to extract from diffusion tensors for the purpose of visualization, segmentation, interpolation, anisotropy measures, tensor similarity measures, fiber tractography, clinical applications, etc will be addressed in the thesis. We begin with the DTI model which results in a $3\mathbf{D}$ image where at each voxel the preferred direction of water diffusion is locally modeled by a Gaussian probability density function whose covariance matrix is a second order 3×3 SPD matrix, referred

to as a diffusion tensor. Towards the end of the thesis, we extend the DTI model to the HOT model [86] and examine the costs and benefits of such a model not only for modeling ADC but also FOD functions to correctly infer the underlying fiber orientations. The contributions of the thesis are: utilizing tensor similarity measures in order to perform tensor field images segmentation, utilizing tensor similarity measures to extract novel anisotropy measures, using tensor anisotropy and diffusivity measures as bio-markers for the diagnosis of Parkinson's disease, and utilizing tensor representation for the purpose of developing a novel model of fiber orientation distribution functions.

The thesis is organized as follows: we first review DW-MR image acquisition, diffusion tensor image reconstruction and several image processing and analysis techniques developed for DT-MR images in Chapter 2 followed by a closer look at tensor similarity measures and anisotropy indices induced by tensor distance measures in Chapter 3. Segmentation of DT-MR images utilizing tensor similarity measures is presented in Chapter 4. Chapter 5 looks at clinical applications of tractography in the classification of Parkinson's Disease (PD) subjects from controls. In Chapter 6, we review the HOT model, extend it to estimate FOD functions and develop a new anisotropy measure derived directly from FOD functions. Chapter 7 concludes the thesis.

Chapter 2

Selected Background

2.1 DW-MR Image Acquisition

Diffusion of water molecules in the presence of a strong magnetic field gradient results in a loss of MR signal due to de-phasing of spin coherence. The application of a pair of gradients to elicit differences in diffusion of water molecules among different biological tissues is known as diffusion weighting. The sequence most commonly used for DWI acquisition is Spin Echo Single Shot Echo Planar Imaging (EPI). It uses a pair of gradients, systematically positioned around a 180° refocusing pulse allowing for controlled diffusion weighting [101]. Fig. 2.1 shows a schematic diagram of Spin Echo Single Shot EPI [128].

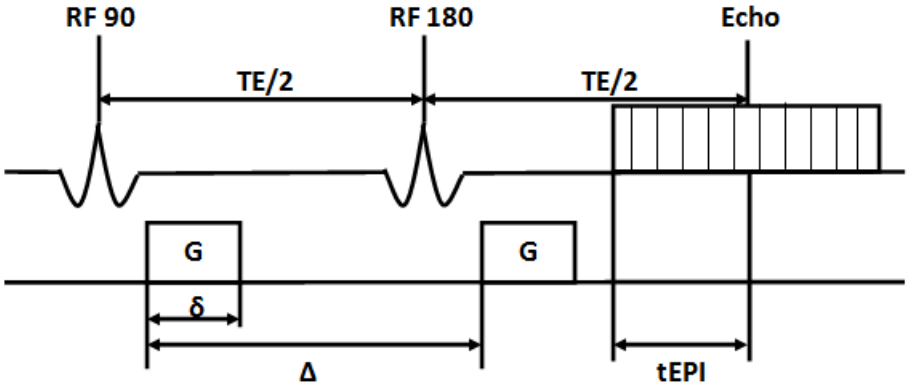

Figure 2.1: Spin Echo Single Shot EPI sequence with diffusion weighting gradients G. RF90 and RF180 are 90° excitation pulse and 180° refocusing pulse respectively. TE is the effective echo time and tEPI denotes the half time interval of the EPI readout. The duration of diffusion encoding gradients is δ and their separation is Δ.

DW-MRI consists of acquiring DWI $S_i, i = 1, 2, \ldots N$, reflecting the relative amount of diffusion along non-coplanar diffusion weighting gradient directions g_i that are uniformly distributed on a unit sphere and one image S_0 with no diffusion sensitizing gradient. Fig. 2.2 shows a typical example of distribution of gradient orientations that uniformly sample a unit sphere.[1] These encoding orientations can be defined by the electrostatic repulsion algorithm previously proposed by Jones et al. [57].

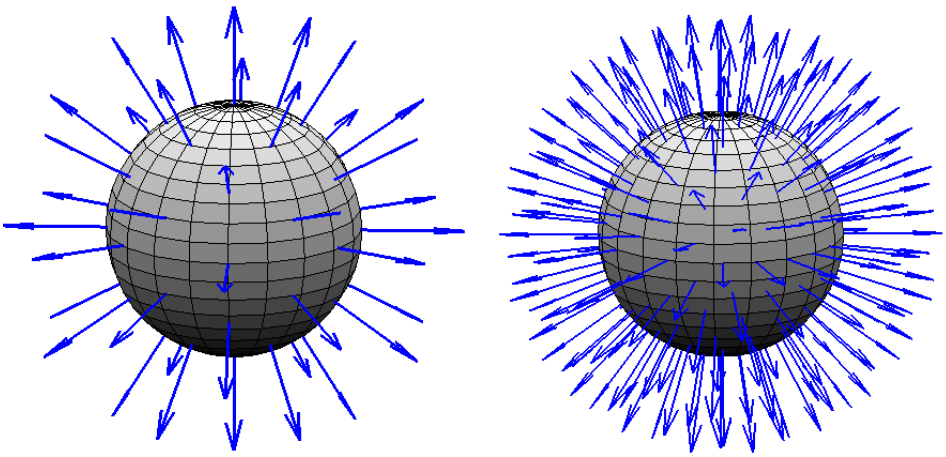

(a) 21 directions (b) 81 directions

Figure 2.2: Diffusion weighting encoding directions

The requirements that the diffusion weighting gradient directions be non-coplanar, uniformly distributed on a unit sphere, and the least number of gradient directions required will be evident in Section 2.2 below. In the meantime, a typical set of DW-MR images is shown in Fig. 2.3. As can be seen in this figure, the individual images don't seem to convey much information. However, as we will see in the next sections, quite good features can be reconstructed from DT-MR images.

2.2 Second Order Diffusion Tensor Reconstruction

The second order diffusion tensor D, i.e. a 3×3 SPD matrix, characterizing anisotropic water diffusion within a macroscopic voxel is estimated from the N DWI S_i and one image S_0

[1] Since diffusion of water molecules in the body is symmetric, we don't actually need to sample the gradient orientations from a unit sphere. It suffices to sample from a unit hemisphere. Thus the 21 and 81 gradient orientations in Fig 2.2(a) and 2.2(b) refer only to the upper half hemisphere.

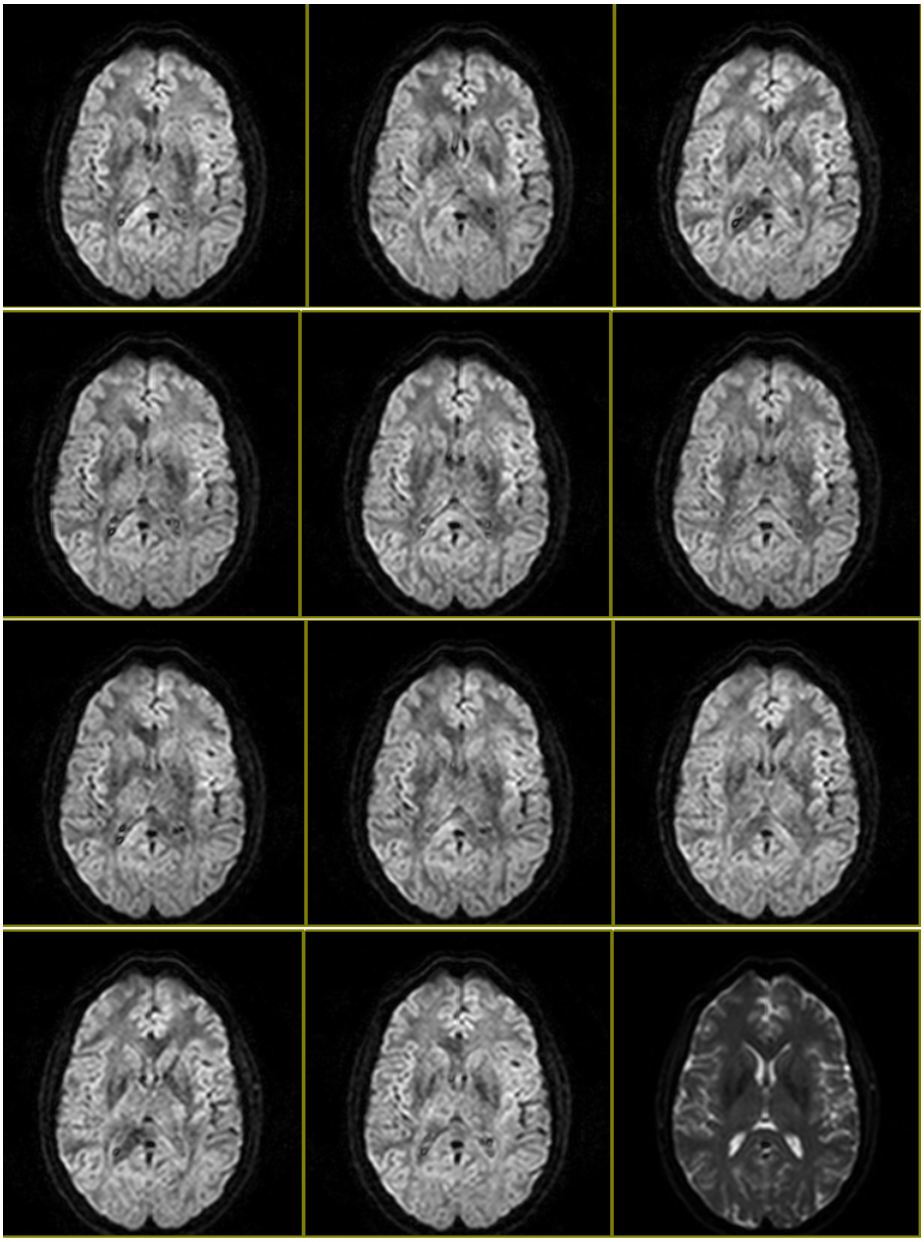

Figure 2.3: DWI for a human brain scan acquired using a Phillips Achieva 3.0 Tesla scanner with slices parallel to the anterior-commissure posterior-commissure line. The bottom right image corresponds to the image S_0 acquired with no diffusion sensitizing gradient.

acquired with no diffusion sensitizing gradient [120]. Using the Bloch-Torrey equation [103], Stejskal and Tanner derived the following formula to relate the DWI measured in the spin echo experiment to the diffusion tensor estimation D [101]:

$$S_i = S_0 e^{-b g_i^T D g_i}, \qquad i = 1, 2, \ldots N \tag{2.1}$$

where the b-value renders the amount of diffusion weighting and is determined by

$$b = \gamma^2 G^2 \delta^2 (\Delta - \delta/3) \tag{2.2}$$

where γ is the gyromagnetic ratio, G is the maximum diffusion encoding gradient strength and δ and Δ are as described in Fig. 2.1. Taking the natural logarithm of both sides of (2.1) and rearranging, we get

$$g_i^T D g_i = \frac{-1}{b} ln(\frac{S_i}{S_0}), \qquad i = 1, 2, \ldots N \tag{2.3}$$

The expression on the left, i.e., $g^T D g$, is known as the diffusivity function. Since D is symmetric, it has six degrees of freedom. Hence Eq.(2.3) results in a $N \times 6$ system of linear equations that is solved at each voxel independently. Denoting the diffusion tensor D as

$$D = \begin{pmatrix} D_{xx} & D_{xy} & D_{xz} \\ D_{xy} & D_{yy} & D_{yz} \\ D_{xz} & D_{yz} & D_{zz} \end{pmatrix}$$

and the gradient directions as $g_i = (g_{ix}\ g_{iy}\ g_{iz})^T$, the set of linear equations obtained from Eq.(2.3) will look like

$$\begin{pmatrix} g_{1x}^2 & g_{1y}^2 & g_{1z}^2 & 2g_{1x}g_{1y} & 2g_{1x}g_{1z} & 2g_{1y}g_{1z} \\ g_{2x}^2 & g_{2y}^2 & g_{2z}^2 & 2g_{2x}g_{2y} & 2g_{2x}g_{2z} & 2g_{2y}g_{2z} \\ \ldots & \ldots & \ldots & \ldots & \ldots & \ldots \\ g_{kx}^2 & g_{ky}^2 & g_{kz}^2 & 2g_{kx}g_{ky} & 2g_{kx}g_{kz} & 2g_{ky}g_{kz} \end{pmatrix} \begin{pmatrix} D_{xx} \\ D_{yy} \\ D_{zz} \\ D_{xy} \\ D_{xz} \\ D_{yz} \end{pmatrix} = \frac{-1}{b} \begin{pmatrix} ln(\frac{S_1}{S_0}) \\ ln(\frac{S_2}{S_0}) \\ \ldots \\ ln(\frac{S_k}{S_0}) \end{pmatrix}$$

When $N = 6$, this has a unique solution. However it will be very sensitive to noise because any measurement error even in only one direction will give rise to an incorrect diffusion

tensor. Therefore N is generally greater than 6; typically 60 - 100 [6]. In this case, Eq.(2.3) describes a set of over determined linear system of equations which can be solved using the Moore-Penrose pseudo-inverse or the Linear Least Squares (LLS) [68] solution. Denoting it as

$$Ax = B \tag{2.4}$$

we obtain the LLS solution to be

$$x = (A^T A)^{-1} A^T B \tag{2.5}$$

This equation has to be solved for each voxel in the image in order to obtain a tensor image. Moreover, while the LLS solution is the simplest and straight forward approach to solve Eq.(2.3), it does not guarantee that the solution obtained is an SPD matrix. Hence other sophisticated mathematical tools have been explored in the DT-MRI community in order to get an SPD matrix [56, 120, 26, 39, 75, 81, 90, 113, 10]. One may also estimate the diffusion tensor D in the presence of noise; as in [14] where the authors take into account a Gaussian noise model.

2.3 Visualization of DT-MR Images

One of the fundamental problems in DT-MRI is how to visualize these SPD second order tensors. Basser and Pierpaoli [15] used the geometric equivalence between SPD matrices and ellipsoids in order to visualize diffusion tensors as ellipsoids. Given a diffusion tensor D, it can be diagonalized as

$$D = \begin{pmatrix} D_{xx} & D_{xy} & D_{xz} \\ D_{xy} & D_{yy} & D_{yz} \\ D_{xz} & D_{yz} & D_{zz} \end{pmatrix} = \begin{pmatrix} v_{11} & v_{12} & v_{13} \\ v_{21} & v_{22} & v_{23} \\ v_{31} & v_{32} & v_{33} \end{pmatrix} \begin{pmatrix} \lambda_1 & 0 & 0 \\ 0 & \lambda_3 & 0 \\ 0 & 0 & \lambda_3 \end{pmatrix} \begin{pmatrix} v_{11} & v_{12} & v_{13} \\ v_{21} & v_{22} & v_{23} \\ v_{31} & v_{32} & v_{33} \end{pmatrix}^T$$

where each $\lambda_i > 0$ is the eigenvalue of D with corresponding normalized eigenvector $v_{i,j}, i = 1, 2, 3$ and T stands for matrix transposition. The matrix of eigenvectors is an orthogonal matrix (i.e. $VV^T = V^T V = I$). This spectral decomposition can be achieved numerically [94] or analytically [49]. When the eigenvalues are sorted in decreasing order, their corresponding eigenvectors are usually referred to as major, medium and minor eigenvectors respectively.

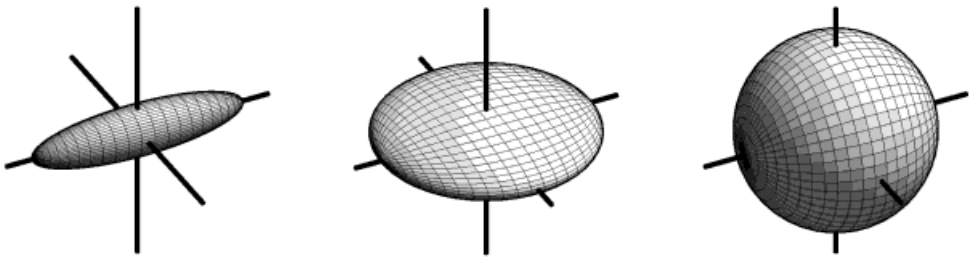

(a) Linear anisotropy $\lambda_1 \gg \lambda_2 \approx \lambda_3$

(b) Planar anisotropy $\lambda_1 \approx \lambda_2 \gg \lambda_3$

(c) Spherical (isotropic) $\lambda_1 \approx \lambda_2 \approx \lambda_3$

Figure 2.4: Ellipsoidal visualization of second order diffusion tensors.

In this visualization method, the eigenvalues of the diffusion tensor correspond to the radii of the ellipsoid while the eigenvectors determine the axes' orientations as shown in Fig. 2.4. This visualization technique reveals the shape of diffusion of water molecules from a given data point in a fixed amount of time. Fig. 2.4(a) reveals linear anisotropic diffusion where $\lambda_1 \gg \lambda_2 \approx \lambda_3$, which typically occurs along white matter fiber bundles, Fig. 2.4(b) reveals planar anisotropic diffusion $\lambda_1 \approx \lambda_2 \gg \lambda_3$ which is typical in regions where fibers are crossing in a plane and Fig. 2.4(c) reveals isotropic (spherical) diffusion $\lambda_1 \approx \lambda_2 \approx \lambda_3$ which is typical of brain gray matter and homogeneous materials such as water.

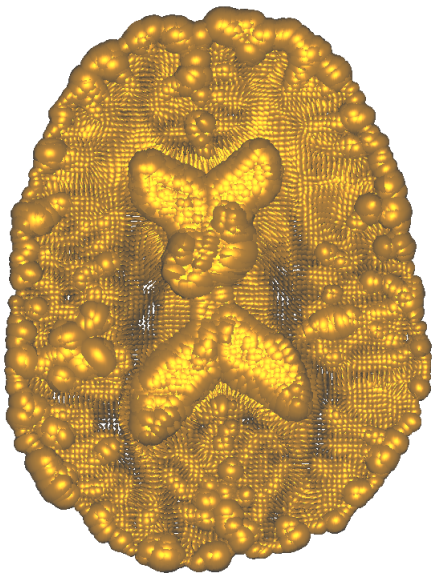

Figure 2.5: Ellipsoidal visualization of a brain image.

Fig. 2.5 shows an ellipsoidal visualization of a brain image slice plotted using ellipsoids [11]. It is clear from this figure that while ellipsoidal visualization gives a qualitative measure of the type of diffusivity (linear, planar or spherical) for individual tensors, it is not convenient for the visualization of a whole image as occlusion is inevitable for large images. It is therefore necessary to extract features from diffusion tensors suitable for visualization and assessment of diffusivity, anisotropy and connectivity of brain regions.

2.4 Diffusion Anisotropy Quantitative Measures

2.4.1 Linear, Planar and Spherical Anisotropy Indices

A quantitative description of anisotropy measures was first presented by Westin et al. [120] by defining coefficients of linear (c_l), planar (c_p) and spherical (c_s) anisotropy indices. Given a diffusion tensor, the authors first decomposed the tensor to its eigenvalues and eigenvectors in such a way that the eigenvalues are sorted so that $\lambda_1 \geq \lambda_2 \geq \lambda_3$ and then defined the following anisotropy measures:

$$c_l = \frac{\lambda_1 - \lambda_2}{\lambda_1}, \qquad c_p = \frac{\lambda_2 - \lambda_3}{\lambda_1}, \qquad c_s = \frac{\lambda_3}{\lambda_1} \tag{2.6}$$

where all measures lie in the range $[0, 1)$ and their sum is equal to 1. These anisotropy indices are rotationally invariant and the values do not depend on the chosen frame of reference of the diffusion tensor. c_l is large where there is linear diffusion as in the brain white matter, and is an indicator of presence of fibrous structures. c_s is an indicator for isotropic diffusion as in the gray matter of the brain. Finally c_p is large where there is planar diffusion which is typical where there is presence of crossing, fanning, kissing and merging of fibrous structures. Fig. 2.6 shows an axial slice of human brain DT-MR image using these three scalar anisotropy indices. White matter and gray matter in the brain are revealed with high intensities on the linear and spherical index images respectively.

While these anisotropy indices are good indicators of anisotropy of diffusion, they are very sensitive to noise. Thus more stable measures were sought and we discuss two such anisotropy indices in the following sections.

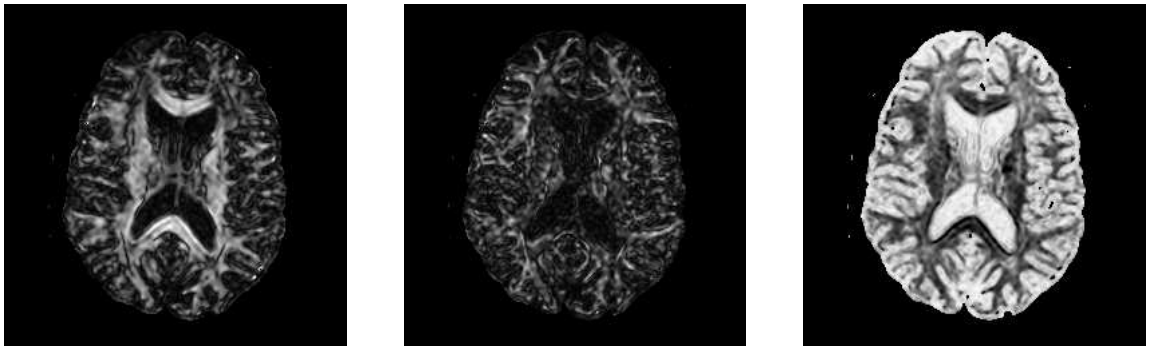

(a) Linear anisotropy index (b) Planar anisotropy index (c) Spherical anisotropy index

Figure 2.6: Linear, planar and spherical indices images.

2.4.2 Fractional and Relative Anisotropy Indices

Another way of looking at anisotropy of diffusion tensors is by first decomposing the tensor to its isotropic and anisotropic parts, and then looking at their proportions. Given a diffusion tensor D, Basser and Pierpaoli [17] proposed decomposing D as

$$D = D_{iso} + D_{an} \tag{2.7}$$

with

$$D_{iso} = \bar{\lambda}\ I \quad \text{and} \quad D_{an} = D - \bar{\lambda}\ I \tag{2.8}$$

where $\bar{\lambda}$ is the arithmetic mean of the eigenvalues of D and $\mathbf{I}$ is a 3×3 identity matrix. The authors then defined two anisotropy measures as follows:

1. Fractional Anisotropy (FA): The ratio of the Frobenius norm of D_{an} to the Frobenius norm of D

$$FA = \sqrt{\frac{3}{2}} \frac{\|D_{an}\|_F}{\|D\|_F} = \sqrt{\frac{3}{2}} \frac{(\lambda_1 - \bar{\lambda})^2 + (\lambda_2 - \bar{\lambda})^2 + (\lambda_3 - \bar{\lambda})^2}{\lambda_1^2 + \lambda_2^2 + \lambda_3^2} \tag{2.9}$$

2. Relative Anisotropy (RA): The ratio of the Frobenius norm of D_{an} to the Frobenius norm of D_{iso}

$$RA = \frac{1}{\sqrt{2}} \frac{\|D_{an}\|_F}{\|D_{iso}\|_F} = \sqrt{\frac{3}{2}} \frac{\sqrt{(\lambda_1 - \bar{\lambda})^2 + (\lambda_2 - \bar{\lambda})^2 + (\lambda_3 - \bar{\lambda})^2}}{\lambda_1 + \lambda_2 + \lambda_3} \tag{2.10}$$

The leading normalizing coefficients are inserted so that the values of FA and RA will fall in the range $[0, 1)$. For both FA and RA indices, values close to 1 indicate highly anisotropic diffusion while values close to 0 indicate isotropic diffusion. These measures are rotationally invariant and scale and sorting independent [120]. Moreover, Hasan et al. [48] have demonstrated analytically that FA maps have a higher Signal to Noise Ratio (SNR) than RA maps for any value of diffusion anisotropy. Fig. 2.7(a) and 2.7(b) show an axial slice of a brain DT-MR image visualized with these measures. As expected, the images show higher intensity on the white matter of the brain. The trace image (see Section 2.5 below) is also displayed for comparison purposes.

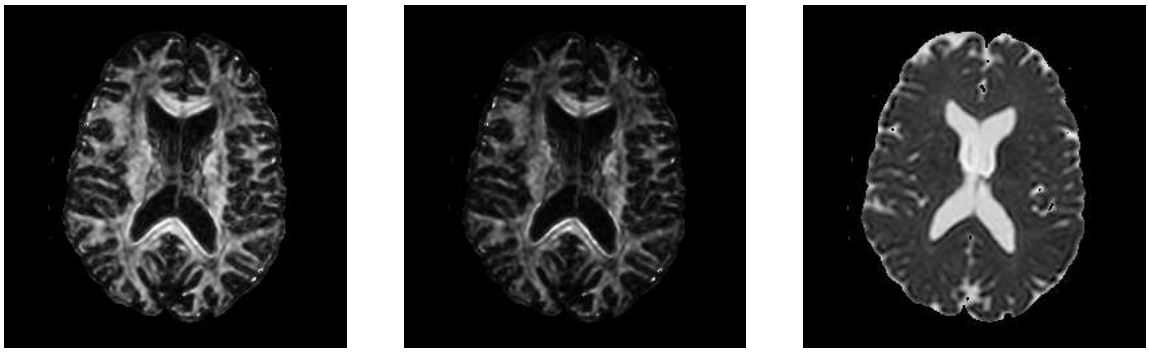

(a) FA (b) RA (c) Trace

Figure 2.7: FA and RA maps reveal high intensity at regions of high anisotropy such as brain white matter but low intensity at isotropic regions such as brain gray matter. The trace image reveals similar intensities at both isotropic and anisotropic regions of the brain.

2.5 Bulk Diffusivity Measures

The measures described above characterize the anisotropic nature of diffusion but do not give information regarding the amount of diffusion because they are all scale invariant. As will be discussed in Chapter 5, the amount of diffusion measurements have been found to be useful for clinical purposes. Such measures of bulk diffusivities include the trace of diffusion tensors, Mean Diffusivity (MD) and ADC defined as:

$$\begin{aligned} Trace(D) &= D_{xx} + D_{yy} + D_{zz} = \lambda_1 + \lambda_2 + \lambda_3 \\ MD(D) &= \frac{Tr(D)}{3}, \ and \\ ADC(D)_i &= g_i^T D g_i \end{aligned} \tag{2.11}$$

The ADC is measured along a given direction. Physically, an estimate of MD can be obtained by taking the arithmetic average of ADCs acquired in all possible directions [60]. In fact, it is shown in [88] that the trace can be expressed as the integral of the quadratic form of the tensor as

$$Trace(D) = \frac{3}{4\pi} \int_S g^T Dg \; dg \tag{2.12}$$

where g is the unit gradient vector and S is the unit sphere. This integral can be evaluated by first expressing the unit vector $g = (x, y, z)^T$ in its polar coordinates with the transformation

$$x = r\sin(\theta)\cos(\varphi) \tag{2.13}$$
$$y = r\sin(\theta)\sin(\varphi) \tag{2.14}$$
$$z = r\cos(\theta) \tag{2.15}$$

We have $r = 1$, θ runs from 0 to π, and φ runs from 0 to 2π. The integral can then be easily calculated as

$$Trace(D) = \frac{3}{4\pi} \int_{\theta=0}^{\pi} \int_{\varphi=0}^{2\pi} g^T Dg \; |J| d\varphi d\theta \tag{2.16}$$

where $|J|$ is the determinant of the Jacobian matrix of the transformation from (x, y, z) coordinate to (r, φ, θ) coordinate and is given by

$$|J| = \begin{vmatrix} \frac{\partial x}{\partial r} & \frac{\partial x}{\partial \theta} & \frac{\partial x}{\partial \varphi} \\ \frac{\partial y}{\partial r} & \frac{\partial y}{\partial \theta} & \frac{\partial y}{\partial \varphi} \\ \frac{\partial z}{\partial r} & \frac{\partial z}{\partial \theta} & \frac{\partial z}{\partial \varphi} \end{vmatrix} = r^2 \sin(\theta) = \sin(\theta)$$

Hence

$$
\begin{aligned}
Trace(D) &= \frac{3}{4\pi}\int_{\theta=0}^{\pi}\int_{\varphi=0}^{2\pi} g^T D g \; |J| d\varphi d\theta \\
&= \frac{3}{4\pi}\Bigg[D_{xx}\int_{\theta=0}^{\pi}\int_{\varphi=0}^{2\pi} \sin^3(\theta)\cos^2(\varphi) d\varphi d\theta + \\
&\qquad D_{yy}\int_{\theta=0}^{\pi}\int_{\varphi=0}^{2\pi} \sin^3(\theta)\sin^2(\varphi) d\varphi d\theta + \\
&\qquad D_{zz}\int_{\theta=0}^{\pi}\int_{\varphi=0}^{2\pi} \sin(\theta)\cos^2(\theta) d\varphi d\theta + \\
&\qquad 2D_{xy}\int_{\theta=0}^{\pi}\int_{\varphi=0}^{2\pi} \sin^3(\theta)\sin(\varphi)\cos(\varphi) d\varphi d\theta + \\
&\qquad 2D_{xz}\int_{\theta=0}^{\pi}\int_{\varphi=0}^{2\pi} \sin^2(\theta)\cos(\theta)\cos(\varphi) d\varphi d\theta + \\
&\qquad 2D_{yz}\int_{\theta=0}^{\pi}\int_{\varphi=0}^{2\pi} \sin^2(\theta)\cos(\theta)\cos(\varphi) d\varphi d\theta \Bigg] \\
&= \frac{3}{4\pi}\Big[\frac{4\pi}{3}D_{xx} + \frac{4\pi}{3}D_{yy} + \frac{4\pi}{3}D_{zz} + 0 + 0 + 0\Big] \\
&= D_{xx} + D_{yy} + D_{zz} \qquad (2.17)
\end{aligned}
$$

Pierpaoli et al. [92] have shown that the trace image exhibits uniform distribution within normal adult brain parenchyma and has similar intensities in both the white and gray matters of the brain even though these tissues are so different histologically. This spatial uniformity has contributed to the increasing clinical utility of the trace image in disease assessment and monitoring since it makes diseased regions more conspicuous when juxtaposed against the homogeneous background of normal parenchyma. Basser and Jones [13] report that questions still remain why the trace image is so uniform in normal adult brain white and gray matters; and more importantly, why it appears so similar between and among normal human subjects. In fact, it appears to be quite similar across a range of normal mammalian brains including mice, rats, cats, monkeys and humans. It is worth considering whether mammalian brains are designed to force the trace image to lie within such a narrow range of values and, if so, what these optimal design criteria are.

2.6 Fiber Tractography

Fiber tractography is a relatively new technique that has generated much enthusiasm and high expectations because it presently is the only approach available to non-invasively study the three-dimensional architecture of white matter tracts in the central nervous system [12]. Assuming that the orientation of the major eigenvector of the diffusion tensor represents the orientation of dominant axonal tracts, DT-MRI can provide a 3**D** vector field in which each vector presents the dominant fiber orientation. Currently, there are several different approaches to reconstruct white matter tracts from DT-MR images. They can roughly be divided into two groups: line propagation algorithms and global energy minimization techniques. An alternative characterization is that the former approach is a deterministic approach while the latter is a probabilistic approach.

The first category uses local tensor information for each step of the propagation. Such methods employ varieties of line convolution integral algorithms that are common in vector field visualizations. The tractography starts at a seed point and propagates along the major eigenvector field by taking time steps proportional to the magnitude of the major eigenvalue. The main differences among techniques in this class stem from the way information from neighboring voxels is incorporated to define smooth trajectories or to minimize noise contributions which may involve diffusion tensor interpolation. The propagation stops when diffusion approaches isotropy or when the turning angle between successive major eigenvectors exceeds a certain threshold (usually when $FA < 0.25$ and $turning\ angle > 45°$). This linear propagation approach, which was dubbed Fiber Assignment by Continuous Tracking (FACT), was used for the first successful tract reconstruction, which was accomplished for a fixed rat brain and showed good agreement with histological knowledge [12]. Fig. 2.8 shows fiber tractography of whole human brain computed via the FACT approach using *ExploreDTI* software [72].

The second category finds the energetically most favorable path between two predetermined pixels. These methods include the Fast Marching Method (FMM) [100], streamtubes and streamsurfaces [127], the diffusion spectrum approach [115], probabilistic approaches [52], etc.

For any fiber tractography algorithm to succeed, it is clear that an interpolation scheme for diffusion tensors has to be developed. Such an interpolation scheme needs to have the key property that the result of interpolating diffusion tensors should be a diffusion tensor,

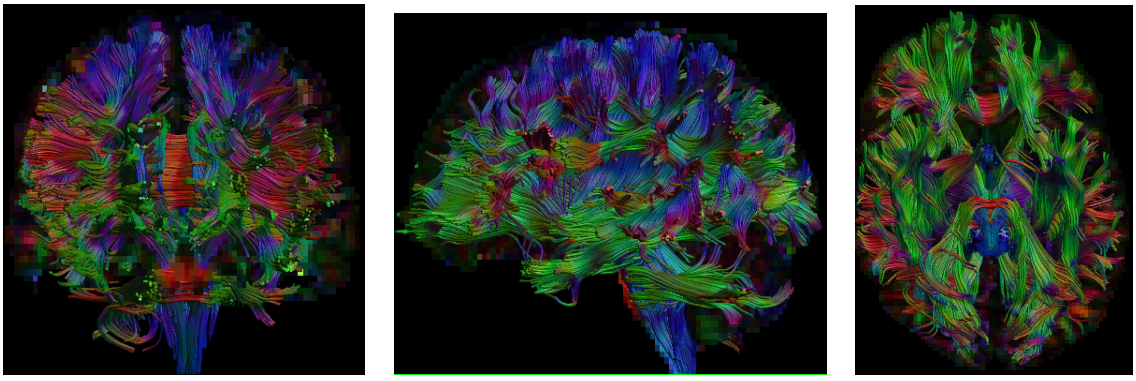

(a) Coronal view (b) Sagittal view (c) Axial view

Figure 2.8: Human brain fiber tracts reconstructed via the FACT algorithm.

i.e., an SPD matrix. This in turn brings the need for a proper diffusion tensor similarity measure to be developed.

While it is tempting to use the Euclidean distance of matrices in order to measure the similarity of diffusion tensors, it has been shown that it has drawbacks. The main shortcoming is that the Euclidean distance does not take into account the fact that diffusion tensors are SPD matrices and thus do not span the whole 9**D** (or even 6**D**) space (See Chapter 3 for details). Actually, the space of 3×3 SPD matrices is an open convex cone. More importantly, performing extrapolation of tensor data along a straight line, whose length is what the Euclidean distance measures, may result in an invalid tensor: a symmetric matrix with zero or negative eigenvalues. A zero eigenvalue is physically impossible for there is always diffusion of water molecules above 0 °K; while a negative eigenvalue is meaningless. In addition, Euclidean distance based averaging of tensors normally results in a mean tensor with larger determinant than the original determinants. However, as a tensor is a covariance matrix of the Gaussian distribution of diffusion of water molecules, the value of its determinant is a direct measure of the dispersion of the associated multivariate Gaussian distribution and thus a larger determinant of the mean corresponds to more diffusion which is physically impossible. This is referred to as the tensor swelling effect, see Fig. 2.10 below. Lastly, the Euclidean distance is not symmetric with respect to matrix inversion in that the average between a tensor and its inverse is not an identity matrix which one would normally expect [5].

2.7 Diffusion Tensor Dissimilarity Measures

Several diffusion tensor dissimilarity measures have been proposed including the Frobenius norm [116], Log-Euclidean distance metric [5], J-divergence dissimilarity measure [112], and Riemannian metric [19, 18]. See Chapter 3 for more details. These tensor distance are appealing because they give closed form solutions and will be used throughout the thesis. A slightly different approach of measuring tensor distances is using geodesic-loxodromes proposed by Kindlmann et al. [62]. However, this method which employs differential geometry does not have a closed solution, thus requires numerical methods to solve and will not be used in our work. Having tensor dissimilarity measures helps to group similar tensors together (segmentation), interpolate tensors, spatially register tensor images, etc.

2.8 Segmentation, Interpolation and Registration

Once a proper tensor dissimilarity measure is defined, segmentation of diffusion tensor images can be performed using any of the methods developed for scalar images segmentation such as level sets, graph cuts, spatial clustering, or PDE based geometric flow methods [112, 22, 96, 74]. Fig. 2.9 shows segmentation of a cardiac wall with graph cuts using the J-divergence tensor dissimilarity measure[2].

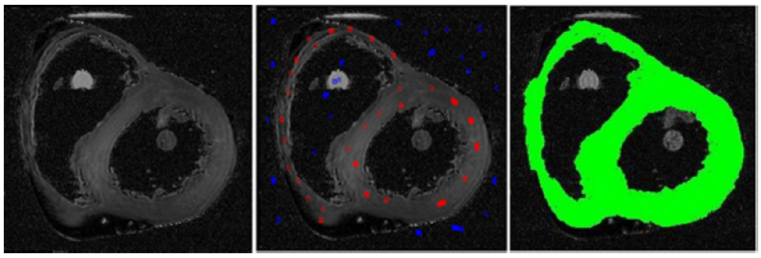

Figure 2.9: Cardiac Wall Segmentation using graph cuts. Left: Visualization using Trace. Middle: Seed points for graph cut segmentation algorithm. Right: Segmentation result.

Similarly, interpolation of diffusion tensors can be achieved using linear, bilinear, splines or other methods that are common in processing and analysis of scalar images. Fig. 2.10

[2]See Chapter 4 for details.

shows the result of Euclidean, Log-Euclidean [5] and Rotational [118] linear interpolation of second order diffusion tensors. In this experiment, the left most diffusion tensor is given by $D_1 = diag([1.2\ 0.4\ 0.4])$ and the right most diffusion tensor is given by $D_2 = diag([0.4\ 1.2\ 0.4])$. The intermediate diffusion tensors are results of interpolating between these tensors. Tensor swelling effect is clearly visible when interpolating in the Euclidean space, Fig. 2.10(a). Interpolating in the Log-Euclidean space minimizes the tensor swelling effect, Fig. 2.10(b). However, it is clear in this specific experiment that all that needs to be interpolated is the rotation matrix that smoothly rotates D_1 until it aligns itself with D_2. This is true because D_1 and D_2 have the same eigenvalues, albeit corresponding to different eigenvectors. In such a scenario, interpolating the rotation matrix makes more sense as shown in Fig. 2.10(c). Also note that since both D_1 and D_2 have the same trace and determinant, Euclidean interpolation preserves only the trace while Log-Euclidean interpolation preserves only the determinant. The Rotational interpolation on the other hand preserves both the trace and the determinant. Similarly, the authors of geodesic-loxodromes approach [62] claim that their approach is designed to explicitly preserve clinically important tensor attributes, such as MD and FA.

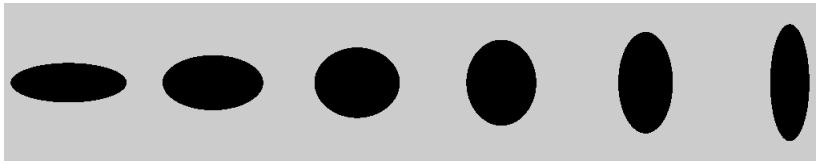

(a) Euclidean interpolation of tensors

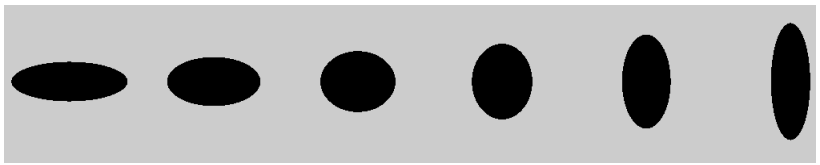

(b) Log-Euclidean interpolation of tensors

(c) Rotational interpolation of tensors

Figure 2.10: Interpolation of second order diffusion tensors.

Registration of DT-MR images is also achieved using algorithms common in scalar image registration such as cross-correlation, mutual information, sum of squared differences, etc using a proper tensor distance defined on diffusion tensor field images to optimize a cost function defined to minimize the dissimilarity of images during the registration process [126, 125, 28]. Therefore we may exploit the tensor distance measures discussed above to perform registration of 2^{nd} order diffusion tensor images. One may also perform local smoothing, commonly known as regularization of tensor field, by making use of these tesnsor distance measures.

In order to reliably reconstruct diffusion tensors, one may also perform a spatial registration on the DW-MR images so that $S_i(p)\ \forall i = 0, 1, .., N$ corresponds to the same anatomical position. Several methods have been proposed for patient motion correction in DW-MRI. Trouard et al. [106] compared three motion correction algorithms: projections onto convex sets [50], collection of navigator echoes to track phase errors [85], and radial scan data acquisition combined with a modified projection-reconstruction algorithm [59]. The authors show that while all the methods work well for correcting translational motion, the radial approach performs better when more complex rotations are involved. Anderson and Gore [4] show that while navigator echo can be used to correct the imaging data for arbitrary translations, only when the diffusion gradient is applied in the phase encode direction is there sufficient information to correct for rotations around all axes, and therefore correct for general rigid body motion. Rohde et al. [95] proposed a mutual information-based registration technique and a spatial transformation model containing parameters that correct for eddy current-induced image distortion and rigid body motion in three dimensions. The authors first define a target coordinate system, rigidly register the first S_0 volume to the target coordinate system and finally register each DW-MR images to the S_0 volume which brings the entire DW-MR images to be positioned in a standardized orientation. For an accurate and fast solution to the registration problem, the authors optimize all parameters simultaneously. Similarly, Mangin et al. [78] proposed a correction algorithm that relies on the maximization of mutual information to estimate the parameters of a geometric distortion model and then replacing the standard least squares based approach by the Geman-McClure M-estimator in order to reduce outliers related artifacts. Atkinson et al. [7] used 2**D** navigator echoes to monitor the k-space sampling which resulted from motion in ungated multi-shot DW-MR acquisitions and showed the propagation of errors in DW-MR images to the average ADC map during the tensor reconstruction stage. A least squares based automatic registration

of distorted EPI images with corresponding anatomically correct MRI images that models the deformation field (with splines while comprising the affine transform as a special case) has been proposed by Kybic et al. [66].

2.9 Conclusion

In this chapter, we have presented selected background on what has been done in the DT-MRI community with regards to processing and analysis of tensor images. In the subsequent chapters, we will utilize the tensor similarity measures described above in order to derive novel anisotropy measures using these tensor distance measures, perform segmentation of DT-MR tensor field images, and extend the ideas further for higher order tensor modeling of fiber orientations and deriving anisotropy measure from such higher order tensors. Moreover, the existing anisotropy measures will be used as bio-markers for the diagnosis of Parkinson's disease in normal and disease subjects.

Chapter 3

Tensor Distance to Anisotropy Measure

Measurement of diffusion tensors on a voxel-by-voxel basis has led to the development of scalar quantities, called indices of anisotropy, that resemble histological or physiological stains characterizing the intrinsic features of tissue microstructure and microdynamics. The most commonly used such scalar diffusion anisotropy measure is FA [17]. It is defined as the distance of a diffusion tensor from its closest isotropic tensor. It is rotationally invariant and, therefore, objective and insensitive to the choice of laboratory coordinate system. It has been widely used for revealing the white matter in brain images, as a parameter for seeding and stopping in fiber tractography, and for the diagnosis, assessment, and classification of patients and healthy subjects in clinical settings [12, 37, 123, 77, 23].

Despite the extensive use of FA in the DT-MRI community, not much attention has been given to the mathematical derivation of FA from diffusion tensors. The FA value is derived using the Euclidean norm, although it is known that the space of diffusion tensors does not form a Euclidean vector space and thus the Euclidean norm is not appropriate for tensors. In fact averaging using the Euclidean norms results in a tensor swelling effect; even worse, computations using the Euclidean norm can result in non SPD matrices which is not physically possible [5]. To this end, appropriate tensor distance measures that take into account the manifold of the space of diffusion tensors have been proposed. These distance measures include the J-divergence, Log-Euclidean and Riemannian distance metrics [112, 5, 19]. Therefore it is more consistent with the definition of FA to use these appropriate tensor

distance measures instead of Euclidean norms in deriving anisotropy measures for diffusion tensors.

In this chapter, we propose two novel and robust diffusion anisotropy measures derived using these appropriate diffusion tensor distance measures. We demonstrate qualitatively that our new anisotropy measures reveal superior white matter profiles of DT-MR brain images and analytically show that these new measures have higher SNR than FA. An interesting finding of our work is that given a diffusion tensor, its closest isotropic tensor is different for different tensor distance measures used.

3.1 Method

We start by revisiting the development of FA in order to develop the mathetical theories of our anisotropy measures. Given diffusion tensor D with eigenvalues λ_1, λ_2 and λ_3, FA is derived by first decomposing D as

$$D = D_{iso} + D_{an} \tag{3.1}$$

where $D_{iso} = \bar{\lambda}\ I$ is the isotropic part of D, $D_{an} = D - \bar{\lambda}\ I$ is the anisotropic part of D, $\bar{\lambda} = (\lambda_1 + \lambda_2 + \lambda_3)/3$ is the arithmetic mean of the eigenvalues of D and I is a 3×3 identity matrix. Clearly D_{iso} is an isotropic tensor because it has equal eigenvalues given by $\lambda_1 = \lambda_2 = \lambda_3 = \bar{\lambda}$. D_{iso} is commonly referred to as the closest isotropic tensor to D.

Having decomposed a diffusion tensor into its isotropic and anisotropic parts, we then obtain magnitudes (or lengths) of D, D_{iso} and D_{an} by taking their Euclidean norms. The diffusion tensor magnitude, also known as tensor contraction, is equivalent to the $L-2$ norm of the diffusion tensor's matrix representation and is given by

$$\begin{aligned} \|D\|_2 &= \sqrt{trace(DD^T)} \\ &= \sqrt{trace(D^2)} \end{aligned} \tag{3.2}$$

where T stands for matrix transposition.

Applying Eq.(3.2) to D, D_{iso} and D_{an}, we obtain

$$\begin{aligned} \|D_{iso}\|_2 &= \sqrt{trace(\bar{\lambda}^2 I^2)} \\ &= \sqrt{\bar{\lambda}^2\ trace(I)} \\ &= \sqrt{3}\bar{\lambda} \end{aligned} \tag{3.3}$$

$$\begin{aligned} \|D\|_2 &= \sqrt{trace(D^2)} \\ &= \sqrt{\lambda_1^2+\lambda_2^2+\lambda_3^2} \text{ .....(See section 3.1.3 for the proof.)} \end{aligned} \tag{3.4}$$

$$\begin{aligned} \|D_{an}\|_2 &= \sqrt{trace((D-\bar{\lambda}\ I)^2)} \\ &= \sqrt{trace(D^2-2\bar{\lambda}D+3\bar{\lambda}^2)\ I} \\ &= \sqrt{\lambda_1^2+\lambda_2^2+\lambda_3^2-2\bar{\lambda}(\lambda_1+\lambda_2+\lambda_3)+3\bar{\lambda}^2} \\ &= \sqrt{(\lambda_1-\bar{\lambda})^2+(\lambda_2-\bar{\lambda})^2+(\lambda_3-\bar{\lambda})^2} \end{aligned} \tag{3.5}$$

FA is then defined as:

$$\begin{aligned} FA &= \sqrt{\frac{3}{2}}\ \frac{\|D_{an}\|_2}{\|D\|_2} \\ &= \sqrt{\frac{3}{2}}\ \sqrt{\frac{(\lambda_1-\bar{\lambda})^2+(\lambda_2-\bar{\lambda})^2+(\lambda_3-\bar{\lambda})^2}{\lambda_1^2+\lambda_2^2+\lambda_3^2}} \end{aligned} \tag{3.6}$$

Notice that the choice of $D_{iso} = \bar{\lambda}\ I$ is such that it minimizes the distance between D and its closest isotropic tensor. Consider the function

$$f(x) = d(D, D_{iso}) = \|D - D_{iso}\|_2 = \|D_{an}\|_2 = \sqrt{(\lambda_1-x)^2+(\lambda_2-x)^2+(\lambda_3-x)^2} \tag{3.7}$$

Differentiating f with respect to x, we find that f takes its minimum value when $(\lambda_1 - x) + (\lambda_2 - x) + (\lambda_3 - x) = 0$ thus $x = (\lambda_1 + \lambda_2 + \lambda_3)/3$.

It is clear that FA has range [0,1) and it is scaling and rotationally invariant [120]. Moreover it has been demonstrated that the FA map has a higher SNR than other anisotropy measures such as RA for any value of anisotropy greater than zero [48, 89]. The shortcoming

with FA and which we are addressing in this work stems from the fact that FA is derived by making use of the Euclidean norm; yet diffusion tensors do not form a vector space and thus the Euclidean norm is not appropriate for diffusion tensors. In order to appreciate the need for appropriate tensor distance measures, we will start by looking at the space spanned by diffusion tensors.

3.1.1 Manifold of Diffusion Tensors

Since diffusion tensors are SPD matrices, the space spanned by diffusion tensors will be investigated by looking at the manifold of SPD matrices. Moreover, while our interest is in 3×3 SPD matrices, for better visualization and easier analysis we will restrict ourselves to the case of 2×2 SPD matrices [81, 39]. To this end, suppose that the matrix

$$D = \begin{pmatrix} a & c \\ c & b \end{pmatrix}$$

is a 2×2 SPD matrix. The eigenvalues of this matrix are λ such that

$$det(D - \lambda I) = 0 \tag{3.8}$$

where *det* denotes matrix determinant. This gives

$$\lambda^2 - (a+b)\lambda + (ab - c^2) = 0 \tag{3.9}$$

which implies

$$\lambda = \frac{(a+b) \pm \sqrt{(a+b)^2 - 4(ab - c^2)}}{2} \tag{3.10}$$

$$= \frac{(a+b) \pm \sqrt{(a-b)^2 + 4c^2}}{2} \tag{3.11}$$

In order to have SPD matrix, we must have both eigenvalues greater than zero. This implies

$$(a+b) > \sqrt{(a-b)^2 + 4c^2} \tag{3.12}$$

or

$$ab > c^2 \tag{3.13}$$

The inequality in Eq.(3.13) implies both a and b must have the same sign; both positive or negative. However if both are negative, we see that the solution $\lambda = \frac{(a+b)-\sqrt{(a-b)^2+4c^2}}{2}$ will result in a negative λ. Thus both a and b must be greater than zero.[1] Hence for any 2 $\times$ 2 SPD matrix D, we have the necessary and sufficient conditions:

$$ab > c^2, \qquad a > 0,\ b > 0 \tag{3.14}$$

It is not hard to see that the inequality Eq.(3.14) is a hyperboloid inequality. To see its geometry easily, set $0 < u = \frac{a+b}{2}$ and $v = \frac{a-b}{2}$. Then the condition $ab > c^2$ can be rewritten as $\sqrt{v^2 + c^2} < u$ which can be written as

$$v^2 + c^2 < u^2, \qquad u > 0 \tag{3.15}$$

and therefore with this parametrization, 2 $\times$ 2 SPD matrices can be seen to span the interior of an open convex second order cone [81]. Fig. 3.1.1 shows a plot generated by sampling 10,000 random 2 $\times$ 2 SPD matrices to help us visualize the manifold of SPD matrices and confirm the above conclusions.

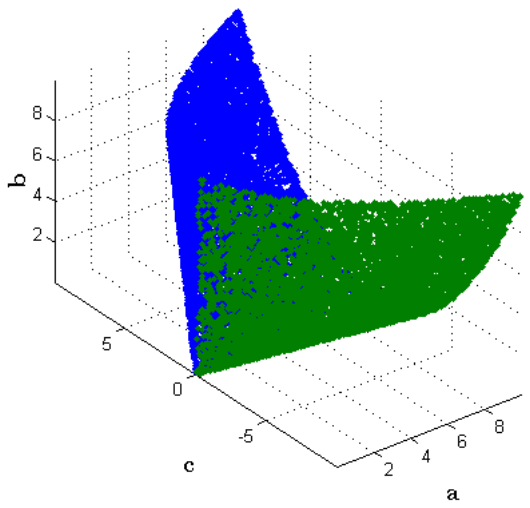

Figure 3.1: Space spanned by 2 $\times$ 2 SPD matrices. Two colors are used to help visualize the 3D nature of the space spanned by 2 $\times$ 2 SPD matrices.

[1] An *nxn* SPD matrix has all its diagonal elements greater than zero.

3.1.2 Tensor Distance Measures

J-divergence Tensor Dissimilarity Measure

Since diffusion tensors are the covariance matrices of the Gaussian distribution that model diffusion of water molecules in the body tissue, Wang and Vemuri [112] noted that the distance between such tensors can in fact be deduced from the distance between their corresponding Gaussian distributions. The most frequently used distance between Gaussian distributions is the Kullback-Leibler(KL) divergence:

$$KL(p\|q) = \int p(x) log \frac{p(x)}{q(x)} dx \tag{3.16}$$

However as this distance is not commutative which is a required criteria for dissimilarity measure, the authors symmetrize it by taking the J-divergence given by:

$$J(p,q) = \frac{1}{2}(KL(p\|q) + KL(q\|p)) \tag{3.17}$$

The tensor distance is then defined as the square root of the J-divergence. The simplification of this distance gives a closed form for the distance given by:

$$d_{JD}(D_1, D_2) = \frac{1}{2}\sqrt{trace(D_1^{-1}D_2 + D_2^{-1}D_1 - 2I)} \tag{3.18}$$

Log-Euclidean Tensor Distance Measure

The first comprehensive and mathematically sound and complete tensor distance metric in the DT-MRI community is probably the **Log-Euclidean** tensor distance [5]. This metric, motivated by the shortcomings of the $L-2$ norm and the computationally expensive nature of other affine-invariant Riemannian metrics, addresses the tensor dissimilarity problem by noting that a tensor D has a unique symmetric matrix logarithm $L = log(D)$. It verifies $D = exp(L)$ where exp is the matrix exponential. Conversely, each symmetric matrix is associated to a tensor by the exponential. L is obtained from D by changing its eigenvalues into their natural logarithms, which can be done easily in an orthonormal basis in which D (and L) is diagonal. The beauty of the space of symmetric matrices is that they form a vector space with respect to matrix addition and scalar multiplication. On the other hand, the tensor vector space with a Log-Euclidean metric is isomorphic (the algebraic structure of the vector space is conserved) and isometric (distances are conserved) with the corresponding

Euclidean space of symmetric matrices. Thus by going from the space of tensors to the space of symmetric matrices, the authors successfully transfer the matrix addition "+" and the scalar multiplication "$\cdot$" back to the tensor space with matrix exponential. This defines on tensors the logarithmic multiplication $\bigodot$ and the logarithmic scalar multiplication $\bigotimes$ given by:

$$\begin{cases} D_1 \bigodot D_2 = exp(log(D_1) + log(D_2)) \\ \lambda \bigotimes D = exp(\lambda \cdot log(D)) = D^{\lambda} \end{cases}$$

When one considers only the multiplication $\bigodot$ on the tensor space, one has a Lie group structure which exhibits distances that are invariant by multiplication and inversion. This distance measure named by the authors as the Log-Euclidean tensor distance can be written as:

$$d_{LE}(D_1, D_2) = \|log(D_1) - log(D_2)\|_2 \tag{3.19}$$

It is apparent from Eq.(3.19), matrices with null or zero eigenvalues are at infinite distance from tensors.

Riemannian Tensor Distance Measure

Finally, noting that Eq.(3.19) is a true geodesic distance only when D_1 and D_2 are commuting symmetric positive definite matrices, Bhatia [19] rectifies the metric further to get a Riemannian metric. The Riemannian metric (d_{RI}) is given by:

$$d_{RI}(D_1, D_2) = \|log(D_1^{-1/2} D_2 D_1^{-1/2})\|_2 \tag{3.20}$$

Since FA essentially measures the distance of a diffusion tensor from its closest isotropy, our aim is now to employ these distance measures in order to compute the distance of a given diffusion tensor from its closest isotropy.

3.1.3 Tensor Distance From Closest Isotropy

Given a diffusion tensor matrix D, let e_1, e_2 and e_3 be its normalized eigenvectors and λ_1, λ_2 and λ_3 be its eigenvalues so that $V = (e_1|e_2|e_3)$ denotes its normalized eigenvectors matrix such that $VV^T = V^TV = I$ and $\Lambda = diag(\lambda_1, \lambda_2, \lambda_3)$ denotes its eigenvalues matrix. Then applying spectral decomposition to D, we obtain

$$D = V\Lambda V^T \tag{3.21}$$

Such spectral decomposition is a very useful tool to prove some identities. For instance the fact that $trace(D) = \lambda_1 + \lambda_2 + \lambda_3$ can be easily proved as follows:

$$\begin{aligned} trace(D) &= trace(V\Lambda V^T) \\ &= trace(V(\Lambda V^T)) \\ &= trace((\Lambda V^T)V) \ .....(\because trace(AB) = trace(BA)) \\ &= trace(\Lambda(V^T V)) \\ &= trace(\Lambda) \ .....(\because VV^T = V^T V = I) \\ &= \lambda_1 + \lambda_2 + \lambda_3 \end{aligned} \tag{3.22}$$

Similarly, $trace(D^2) = trace((V\Lambda V^T)(V\Lambda V^T)) = trace(V\Lambda^2 V^T) = trace(\Lambda^2) = \lambda_1^2 + \lambda_2^2 + \lambda_3^2$. For D_{iso}, denoting its eigenvalues matrix as $\bar{\Lambda} = diag(\bar{\lambda}, \bar{\lambda}, \bar{\lambda}) = \bar{\lambda} I$ and using the identity $VV^T = V^T V = I$, we obtain

$$D_{iso} = \bar{\lambda} I = \bar{\lambda} VV^T = V(\bar{\lambda} I)V^T = V\bar{\Lambda}V^T \tag{3.23}$$

which shows D_{iso} has the same normalized eigenvectors matrix as D. Actually D_{iso} is degenerate (spherical), hence any set of three normalized orthogonal vectors in $\Re^3$ can be used as its eigenvectors. Choosing V as its eigenvectors, however, enables us to simplify computations considerably. For instance observe that using Eq.(3.23), it follows that $D_{an} = D - D_{iso} = V\Lambda V^T - V\bar{\Lambda}V^T = V(\Lambda - \bar{\Lambda})V^T$ which shows D_{an} has eigenvalues given by $\lambda_1 - \bar{\lambda}$, $\lambda_2 - \bar{\lambda}$, and $\lambda_3 - \bar{\lambda}$ in agreement with Eq.(3.5). Also note that the choice of $\bar{\lambda}$ that minimizes the distance between D and D_{iso} depends on the distance metric used, as will be shown in section 3.1.4.

Remark 1. *Observe that by assigning the same eigenvector matrix to a closest isotropic tensor, we are essentially enforcing the same orientation to both a given diffusion tensor and its closest isotropy. This implies the dissimilarity measure between a diffusion tensor and its closest isotropy is due to shape difference only. For this reason, we may refer to the tensor dissimilarity measure between a given diffusion tensor and its closest isotropy as Tensor Shape Dissimilarity measure. Therefore, we will also refer to anisotropy measures obtained by using different tensor distances as Shape Anisotropy (SA) measures.*

Using the identities $D^{-1} = V\Lambda^{-1}V^T$ and $log(D) = Vlog(\Lambda)V^T$, it is then easy to show that

$$\begin{aligned} d_{JD}(D, D_{iso}) &= \frac{1}{2}\sqrt{trace(D^{-1}D_{iso} + D_{iso}^{-1}D - 2I)} \\ &= \frac{1}{2}\sqrt{trace(V\Lambda^{-1}\bar{\Lambda}V^T + V\bar{\Lambda}^{-1}\Lambda V^T) - 6} \\ &= \frac{1}{2}\sqrt{\sum_{i=1}^{3}\frac{\bar{\lambda}}{\lambda_i} + \sum_{i=1}^{3}\frac{\lambda_i}{\bar{\lambda}} - 6} \\ &= \frac{1}{2}\sqrt{\sum_{i=1}^{3}\frac{(\lambda_i - \bar{\lambda})^2}{\bar{\lambda}\lambda_i}} \end{aligned} \tag{3.24}$$

$$\begin{aligned} d_{LE}(D, D_{iso}) &= \|log(D) - log(D_{iso})\|_2 \\ &= \|Vlog(\Lambda)V^T - Vlog(\bar{\Lambda})V^T\|_2 \\ &= \|V(log(\Lambda) - log(\bar{\Lambda}))V^T\|_2 \\ &= \|Vlog(\Lambda\bar{\Lambda}^{-1})V^T\|_2 \\ &= \sqrt{trace(Vlog^2(\Lambda\bar{\Lambda}^{-1})V^T)} \\ &= \sqrt{\sum_{i=1}^{3} log^2\frac{\lambda_i}{\bar{\lambda}}} \end{aligned} \tag{3.25}$$

$$\begin{aligned} d_{RI}(D, D_{iso}) &= \|log(D^{-1/2}D_{iso}D^{-1/2})\|_2 \\ &= \|log(V\Lambda^{\frac{-1}{2}}\bar{\Lambda}\Lambda^{\frac{-1}{2}}V^T)\|_2 \\ &= \|Vlog(\Lambda^{-1}\bar{\Lambda})V^T\|_2 \\ &= \sqrt{trace(Vlog^2(\Lambda^{-1}\bar{\Lambda})V^T)} \\ &= \sqrt{\sum_{i=1}^{3} log^2\frac{\lambda_i}{\bar{\lambda}}} \end{aligned} \tag{3.26}$$

The fact that Eqs.(3.19) and (3.20) simplify to the same expression (Eqs. (3.25) and (3.26) respectively) in computing the tensor distance between D and D_{iso} should not come as a surprise; after all $d_{LE}(D_1, D_2) = \|log(D_1) - log(D_2)\|_2$ is a special case of $d_{LE}(D_1, D_2) = \|log(D_1^{-1/2}D_2D_1^{-1/2})\|_2$ which holds when D_1 and D_2 are commuting matrices [19]. Indeed D and D_{iso} are commuting matrices as can be seen by: $DD_{iso} = D\bar{\lambda}I = \bar{\lambda}DI = \bar{\lambda}ID = D_{iso}D$.

3.1.4 Closest Isotropic Tensor

Consider the J-divergence tensor distance. In order to find the value of $\bar{\lambda}$ that minimizes the distance between D and its closest isotropic tensor, define the function

$$f(\bar{\lambda}) = \frac{(\lambda_1 - \bar{\lambda})^2}{\bar{\lambda}\lambda_1} + \frac{(\lambda_2 - \bar{\lambda})^2}{\bar{\lambda}\lambda_2} + \frac{(\lambda_3 - \bar{\lambda})^2}{\bar{\lambda}\lambda_3} \tag{3.27}$$

Then differentiating f with respect to $\bar{\lambda}$, we find that f takes its minimum value when

$$\bar{\lambda}^2(\frac{1}{\lambda_1} + \frac{1}{\lambda_2} + \frac{1}{\lambda_3}) = \lambda_1 + \lambda_2 + \lambda_3 \tag{3.28}$$

or

$$\bar{\lambda} = \sqrt{\frac{trace(D)}{trace(D^{-1})}} \tag{3.29}$$

Similarly, the value of $\bar{\lambda}$ that minimizes the distance between D and its closest isotropic tensor when using the Log-Euclidean and the Rimannian tensor distances is given by [18]

$$\bar{\lambda} = det(D)^{1/3} \tag{3.30}$$

3.2 Shape Anisotropy (SA)

The new anisotropy measure is developed by making the following observations about Eqs.(3.24), (3.25) and (3.26):

(i) They are functions of eigenvalues only.

(ii) They have ranges $[0, +\infty)$.

(iii) They are scale invariant and rotationally invariant.

(iv) They measure the distance of a tensor from its closest isotropic tensor.

These are the properties exhibited by FA except for the range values. Therefore we can essentially use Eqs.(3.24), (3.25) and (3.26) to measure the anisotropy of diffusion tensors. For comparisons with FA and for displaying purposes, we first normalize them using the *tanh* function and define two novel anisotropy measures as follows:

$$SA_{JD} = tanh\left(\sqrt{\sum_{i=1}^{3}\frac{(\lambda_i-\bar{\lambda})^2}{\lambda_i\bar{\lambda}}}\right) \tag{3.31}$$

$$SA_{LE} = tanh\left(\sqrt{\sum_{i=1}^{3}log^2\left(\frac{\lambda_i}{\bar{\lambda}}\right)}\right) \tag{3.32}$$

where $\bar{\lambda}$ is as shown in Eqs.(3.29) and (3.30). Of course, both Eqs.(3.25) and (3.26) give rise to the same $ShapeAnisotropy(SA)$, hence we will consider only SA_{LE}. It is easy to see that SA, just like FA, is rotationally invariant, scale invariant, sorting of eigenvalues independent and has range [0, 1).

3.3 Experimental Results

3.3.1 Qualitative Comparison of FA and SA

A qualitative comparison of FA and SA maps is shown in Fig. 3.2 using a real brain DT-MR image slice. The diffusion weighted images were acquired using a Phillips Achieva 3.0 Tesla scanner using 32 directions with slices parallel to the anterior-commissure posterior-commissure line. 60 continuous slices of 2.2 mm thickness were collected with a Field of View (FOV) of 212 mm, pixel size 0.8281 mm^2. We see from the figure that both SA_{JD} and SA_{LE} maps have brighter intensities and higher contrast than FA which can also be seen in Fig. 3.2(d) and Fig. 3.2(e) where we show the difference between SA and FA maps (i.e. $SA - FA$). The intensity values of SA_{LE} and FA maps are inspected along the white line shown and plotted in Fig. 3.2(f) which clearly shows the SA map has higher intensity values than the FA map along the line.

It is interesting to note that while the mathematical expressions of SA_{JD} and SA_{LE} seem very different, their corresponding images are very similar (see also Fig. 3.4 below). Since SA_{JD} and SA_{LE} values take consistently larger values than FA, we expect SA_{JD} and SA_{LE} maps to provide a more detailed depiction of anisotropic areas and better contrast between gray matter and white matter than FA map. This is explored in the following subsections.

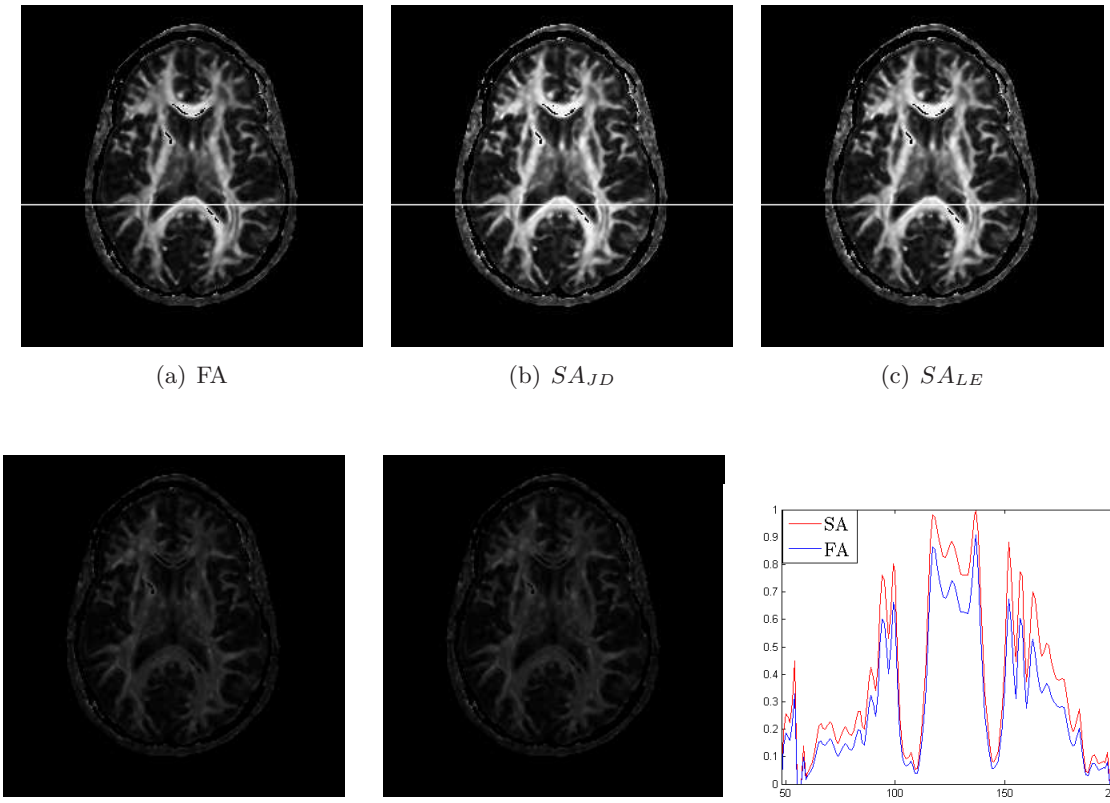

(a) FA (b) SA_{JD} (c) SA_{LE}

(d) SA_{JD} minus FA (e) SA_{LE} minus FA (f) FA and SA_{LE} profiles along the white line

Figure 3.2: Qualitative comparison of FA, SA_{JD} and SA_{LE} maps using a DT-MR brain image slice. The SA_{JD} and SA_{LE} maps show higher intensity values as shown in 3.2(b) and 3.2(c) and supported by the SA_{JD} - FA and SA_{LE} - FA maps shown in 3.2(d) and 3.2(e). The intensity values of FA and SA_{LE} maps are inspected along the white line shown in 3.2(a) and 3.2(c) and plotted in 3.2(c) again confirming SA_{LE} maps have higher intensity values than FA.

3.3.2 Tissue discrimination with FA and SA

For the task of discriminating between two tissue classes, a measure of diffusion anisotropy, A, can be evaluated using a detectability index [2],

$$d = \frac{< A_1 > - < A_2 >}{\sqrt{\sigma_1^2 - \sigma_2^2}} \tag{3.33}$$

where $(< A_1 >, \sigma_1^2)$ and $(< A_2 >, \sigma_2^2)$ are the means and variances of the anisotropy values for the two tissue classes. The anisotropy measure with the greatest detectability index should be close to optimum for the specified task. The variances depend upon a combination of tissue and subject variability, measurement noise, the encoding axes, the diffusion weighting and the pulse sequence parameters (TR, TE, etc.). It is well known that these measures of diffusion anisotropy are highly sensitive to measurement noise and as such any study of diffusion anisotropy must take noise effects into account.

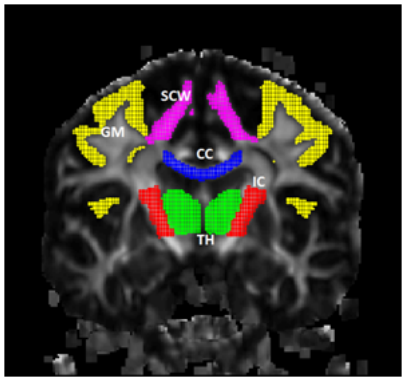

Figure 3.3: Single slice of FA map from JHU_MNI_SS DTI dataset with corresponding regions of interest segmented using JHU_MNI_SS_WMPM_TypeI white matter parcellation map: CC = corpus callosum, IC = Internal Capsule, TH = Thalamus, GM = Gray matter, and SCW = Subcortical white matter

In order to compare SA and FA in discriminating tissue classes, we calculated the detectability indices of these anisotropy measures for a publicly available DTI atlas [1] downloaded from Johns Hopkins Medical Institute Laboratory of Brain Anatomical MRI (http://lbam.med.jhmi.edu/). We also downloaded a white matter parcellation map [2] that is already registered with the atlas from the same source. Both the atlas and the white

[1] JHU_MNI_SS

[2] JHU_MNI_SS_WMPM_TypeI

matter parcellation map are in the Montreal Neurological Institute (MNI) coordinate system with 181 x 217 x 181 (1 mm isotropic) resolution. Since the white matter parcellation map was already registered with the atlas, the regions of interest were easily extracted by superimposing the white matter parcellation map onto the SA and FA anisotropy measures calculated from the atlas. Our tissue detectability results are presented in Table 3.1 where the values of d shown in bold face indicate that the anisotropy index given on that row performs best in discriminating tissue classes on the corresponding column. We observe that while FA performs better in detecting differences among tissues within the white matter; SA detects differences between white matter and gray matter regions better.

Table 3.1: Tissue detectability using FA and SA. Abbreviations of the tissue classes is as shown in Fig. 3.3.

AI\ ROI	CC vs IC	CC vs TH	CC vs GM	CC vs SCW	IC vs TH	IC vs GM	IC vs SCW	TH vs GM	TH vs SCW	GM vs SCW
FA	0.24	**0.95**	2.01	**0.52**	**1.46**	2.69	**0.86**	2.07	**0.45**	1.82
SA_{JD}	**0.39**	0.74	**2.12**	0.36	1.35	**2.89**	0.81	2.10	0.36	**1.90**
SA_{LE}	0.38	0.73	2.10	0.37	1.33	2.87	0.82	**2.11**	0.34	1.89

3.3.3 Noise Immunity Considerations

While Fig. 3.2 gives a qualitative comparison of FA and SA maps, we now analytically show that SA has higher noise immunity than FA by comparing the SNR of SA and FA. Once again, because the results obtained with SA_{JD} and SA_{LE} are very similar, here we report only the results obtained using SA_{JD}.

For any Anisotropy Index (AI) such as RA, FA and SA; assuming that all λ_i's are independent with the same standard deviation (std) of noise, the SNR of AI per unit std of noise in λ_i is given by [89]

$$SNR(AI) = \frac{AI}{\sqrt{\sum_{i=1}^{3} \left(\frac{\partial AI}{\partial \lambda_i}\right)^2}} \tag{3.34}$$

Following the approach of Papadakis et al. [89], we have calculated the values of AI and SNR of AI for FA, SA_{JD} and SA_{LE} for a prolate tensor for three types of distributions of

the principal diffusivities, $\lambda_1 \geq \lambda_2 \geq \lambda_3$:

(a) cylindrical, $\lambda_1 \geq \lambda_2 = \lambda_3$,

(b) disc-shaped, $\lambda_1 = \lambda_2 \geq \lambda_3$,

(c) symmetric about $\bar{\lambda}$, $\lambda_1 - \lambda_2 = \lambda_2 - \lambda_3$.

For all the three types of anisotropy the mean diffusivity $\bar{\lambda}$ is kept constant at $0.7 \cdot 10^{-3} mm^2/s$, in agreement with typical values of the experimentally measured value for normal cerebral tissue. In the cylindrical anisotropy, we vary λ_1 from $0.7 \cdot 10^{-3} mm^2/s$ to $2.1 \cdot 10^{-3} mm^2/s$ and keep $\lambda_2 = \lambda_3$ which ensures that $\lambda_1 \geq \lambda_2 \geq \lambda_3$ for all values of λ_1. In the disc-shaped anisotropy, we vary λ_1 from $0.7 \cdot 10^{-3} mm^2/s$ to $1.05 \cdot 10^{-3} mm^2/s$ and keep $\lambda_1 = \lambda_2$ so that once again $\lambda_1 \geq \lambda_2 \geq \lambda_3$. Similarly, λ_1 takes values from $0.7 \cdot 10^{-3} mm^2/s$ to $1.4 \cdot 10^{-3} mm^2/s$ and $\lambda_1 - \lambda_2 = \lambda_2 - \lambda_3$ in the symmetric anisotropy.

Fig. 3.4 shows plots of AI i.e. FA, SA_{JD} and SA_{LE} and SNR(AI), for each of the three types of anisotropy, as a function of the largest principal diffusivity λ_1 which has been normalized relative to $\bar{\lambda}$. We also plot RA and SNR of RA for comparison purposes.

From Figs. 3.4(a), 3.4(c) and 3.4(e), we observe once again that despite their different mathematical expressions SA_{JD} and SA_{LE} have very similar values for all types of anisotropy at all levels of anisotropy. Moreover, SA_{JD} and SA_{LE} are consistently greater than or equal to FA and they exhibit stronger non-linear relationship with λ_1 compared to FA. The gap between SA_{JD} and SA_{LE} on the one hand and FA on the other is pronounced more clearly as we move away from the isotropic case and decreases as we approach the case of linear anisotropy. Therefore, SA_{JD} and SA_{LE} maps will give increased signal intensity for cases of low anisotropy, providing an isotropic background of increased intensity. However, since SA_{JD} and SA_{LE} take consistently larger values than FA, they may provide a more detailed depiction of anisotropic areas. For the cylindrical type, both SA_{JD} and SA_{LE} remain well-bounded to their maximum value for range of values of λ_2 and λ_3 compared to FA. Therefore, SA_{JD} and SA_{LE} maps may provide darker background signal intensity, corresponding to areas of low anisotropy, and stronger contrast between low and high anisotropy area.

Figs. 3.4(b), 3.4(d) and 3.4(f) show plots of SNR(AI) as a function of the normalized dominant principal diffusivity λ_1. For small anisotropy levels, all three AI measures

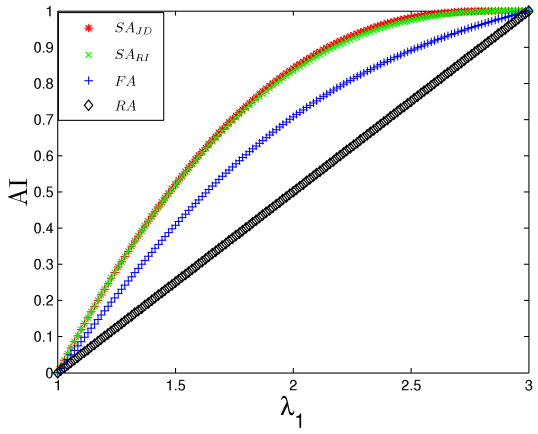

(a) AI: Cylindrical

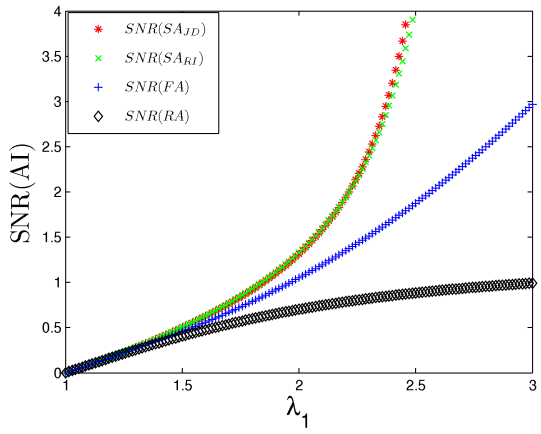

(b) SNR(AI): Cylindrical

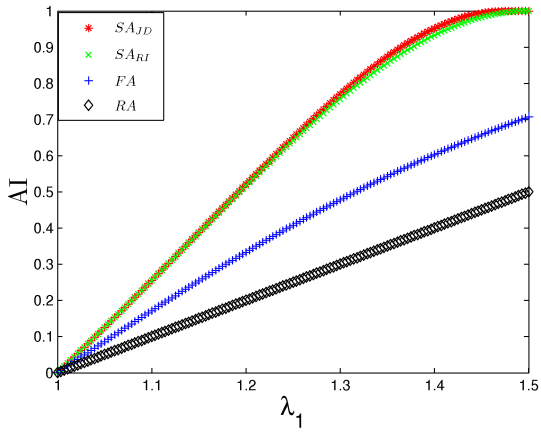

(c) AI: Disk Shaped

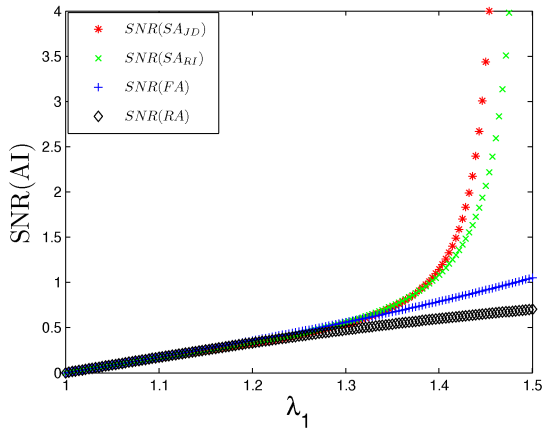

(d) SNR(AI): Disk Shaped

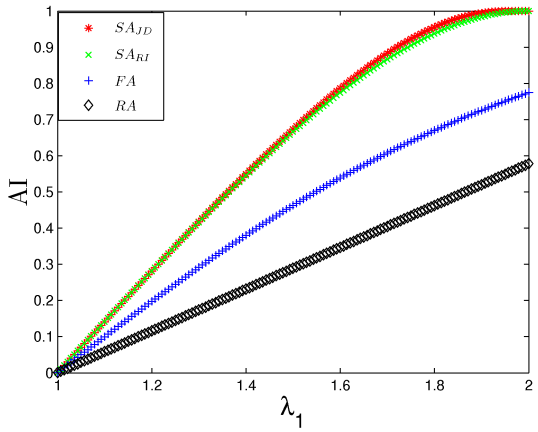

(e) AI: Symmetric

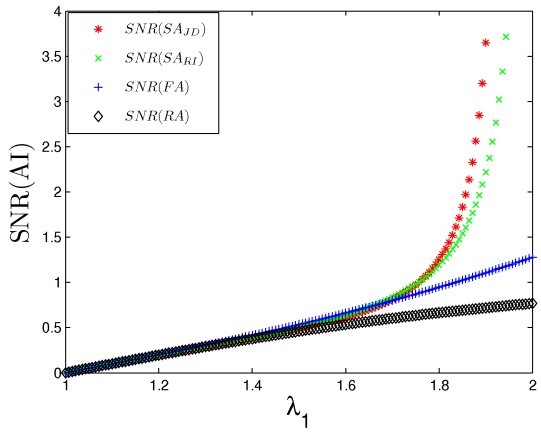

(f) SNR(AI): Symmetric

Figure 3.4: Plots of AI (RA, FA, SA_{JD} and SA_{LE}) in 3.4(a), 3.4(c) and 3.4(e) and the respective SNR(AI) in 3.4(b), 3.4(d) and 3.4(f) of prolate tensor as its anisotropy varies from 0 to 1 as a function of the dominant principal diffusivity λ_1.

have comparable SNR, but their differences in noise sensitivity becomes more prominent as anisotropy level increases, with both SA_{JD} and SA_{LE} having better SNR than FA. Therefore the SA_{JD} and SA_{LE} maps will generally be more robust to noise than the FA map, exhibiting little intensity variation within structures of uniform anisotropy. The difference in the appearance of noise between SA_{JD} and SA_{LE} on the one hand and FA on the other will be more pronounced for strongly anisotropic structures.

3.4 Conclusion

A novel anisotropy measure for DT-MRI is derived using tensor distance measures and its performance compared with existing anisotropy measures. We have shown that our anisotropy take consistently greater than or equal to FA values and they exhibit stronger non-linear relationship with the eigenvalues. The gap between our anisotropy measures on the one hand and FA on the other is pronounced more clearly as we move away from the isotropic case and decreases as we approach the case of linear anisotropy. Therefore, our anisotropy maps give increased signal intensity for cases of low anisotropy, providing an isotropic background of increased intensity. However, since they take consistently larger values than FA, they provide a more detailed depiction of anisotropic areas and give additional information by revealing more white matter structures in the image. In terms of noise immunity, our anisotropy measures have comparable SNR to FA for small anisotropy levels but better SNR than FA as anisotropy level increases. Therefore our anisotropy maps will generally be more robust to noise than the FA map, exhibiting little intensity variation within structures of uniform anisotropy. The difference in the appearance of noise between FA on the one hand and our anisotropy measures on the other are more pronounced for strongly anisotropic structures. Importantly, the significance of this work will be more evident in Chapter 6 where we propose a novel anisotropy measure for higher order tensors using appropriate tensor distance following the same approach.

3.5 Contribution

1. Yonas T. Weldeselassie, Ghassan Hamarneh, Faisal Beg, and M. Stella Atkins. Novel Decomposition of Tensor Distance into Shape and Orientation Distances. In Medical Image Computing and Computer-Assisted Intervention Workshop on Diffusion

Modeling and the Fiber Cup (MICCAI DMFC), pages 173-180, 2009.

2. Yonas T. Weldeselassie, Saba El-Hilo, and M. Stella Atkins. Shape Anisotropy: Tensor Distance to Anisotropy Measure. In SPIE Medical Imaging, Vol. 7962-159, pages 1-8, 2011.

Chapter 4

Second Order Tensor Field Segmentation

An important problem in medical image analysis is the segmentation of anatomical regions of interest. Once regions of interest are segmented, one can extract shape, appearance and structural features that can be analyzed for disease diagnosis or treatment evaluation. Image segmentation where regions of interest are delineated is necessary for performing subsequent quantitative analysis and qualitative visualization. In medical imaging applications, it is apparent that good quality segmentation helps radiologists and physicians extract shape, appearance, and other structural features that can be analyzed for disease diagnosis or treatment evaluation. Analogous to scalar image segmentation, DT-MR image segmentation can rely on:

a) identifying nearby tensors with similar diffusion properties and grouping them into one coherent structure,

b) identifying edges in the images and linking them to form separating boundaries between neighboring structures, and

c) incorporating prior knowledge about shape characteristics of the different targets to segment.

While scalar image segmentation has been studied extensively and different algorithms have been developed over a long period of time, DT-MR image segmentation is a relatively new and challenging task. Early, attempts on DT-MR image segmentation include the

method proposed by Zhukov et al. [129] where the authors extract rotationally invariant scalar diffusion anisotropy measures and use a level-set segmentation method that operates on the scalar field. However this method will fail to distinguish between regions of the same diffusion anisotropy magnitude but oriented in different directions. By incorporating the directions of diffusion in addition to the magnitude during the segmentation process, one can differentiate between regions of same anisotropic diffusion but oriented in different directions.

In order to improve the segmentation of DT-MR data, one has to exploit all the information captured by the tensors. To this end, several level-set based curve evolution techniques for DT-MR image segmentation that operate on the whole diffusion tensor fields have been developed [112, 38, 74, 76, 96]. However, these variational formulations with iterative gradient descent based solutions are sensitive to parameter settings and initialization, and hence may get stuck at suboptimal local minima of the energy functional. Further, implementing intuitive user interaction remains a challenging goal in level set based segmentation techniques. On the other hand, interactive and highly-automated segmentation techniques keep the user 'in the loop' in an attempt to bridge the gap between the clinical users' expert knowledge and the inner workings of the computational tools and algorithms.

Another approach to segment DT-MR images was proposed by Brun et al. [24] where the authors present a framework for unsupervised segmentation of white matter fiber traces obtained from DT-MR data. Fiber tracts are compared pairwise to create a weighted undirected graph which is partitioned into coherent sets using the normalized cut criterion. A simple and yet effective method for pairwise comparison of fiber traces is presented which in combination with the normalized cut criterion is shown to produce plausible segmentations of both synthetic and real fiber trace data. Similarly Wiegell et al. [121] proposed segmentation of major thalamic nuclei based on the characteristic fiber orientation of the cortico thalamic/thalamo cortical striations within each nucleus. Using an automatic clustering algorithm, the authors extracted the Talairach coordinates for the individual thalamic nuclei and claim that the center-of-mass coordinates for the segmented nuclei were found to agree strongly with those obtained from a histological atlas. While interesting, such techniques are however restricted to clustering of white matter fiber tracts and not segmentation in general.

In this chapter, we look at segmentation of second order tensor field using two popular interactive multidimensional segmentation algorithms: Graph cuts [22] and Random

Walker [47]. Our goal is in order to cluster tensor pixels to classes such that each tensor is assigned to a single class. This task is useful for parcellation of diffusion tensor brain images to anatomically distinct regions such as thalamus, corpus callosum, internal capsule, etc in order to create a brain atlas. While both these segmentation algorithms have been developed for scalar image segmentation, we extend them to operate on second order tensor field data by utilizing advances in tensor calculus and diffusion tensor distance metrics. The chapter is organized as follows. In section 4.1, we review graph cuts and optimal maximum flow algorithms for computing minimum cuts. In addition, the connection between minimizing energy functions and computation of minimum cut is discussed. After reviewing scalar image segmentation using graph cuts, we present our extension of the method to DT-MR image segmentation in section 4.1.3. We present experimental results on both synthetic and real cardiac and brain DT-MRI images in section 4.1.4. Segmentation using Random Walker is presented in section 4.2 by first presenting the Random Walker algorithm in section 4.2.1, incorporating prior models in section 4.2.2 and extending the algorithm for DT-MR images segmentation in section 4.2.3. Segmentation results using the Random Walker algorithm is presented in section 4.2.4. Finally, we summarize and draw concluding remarks in section 4.3.

4.1 Segmentation using Graph Cuts

The graph cut segmentation technique is an efficient multidimensional image segmentation algorithm that is intuitive, interactive and globally optimal. In this technique, the user first interactively selects certain tensors as object (*"obj"*) or background (*"bkg"*) to provide hard constraints for the segmentation [22]. The *obj* tensors constitute the tensors that belong to the object to be segmented and the *bkg* ones correspond to the tensors that make up the background of the DT-MR image. These *obj* and *bkg* tensors, collectively known as seed points, give clues about the location of the object of interest and the background. A graph structure is then constructed from the DT-MR image where the tensors correspond to graph vertices and edge weights are computed using similarity measures of adjacent vertices. The locations of the seed points are encoded into the graph providing hard constraints for the segmentation; additional soft constraints incorporate information about both regional tissue diffusion as well as boundaries between tissues of different diffusion properties. The graph cuts algorithm is then used to find the globally optimal segmentation of the underlying

3**D** DT-MR image among all segmentations satisfying the constraints. We emphasize that the optimality of this segmentation technique is with respect to the similarity measure used. Therefore in order to obtain a global optimal segmentation result for a particular purpose, it is required to design a similarity measure that takes into account the purpose of the segmentation so as to yield high similarity to objects that need to belong to the same class and low similarity measure to objects of different classes. The topology of the segmentation is unrestricted and both *obj* and *bkg* segments may consist of several isolated parts. Moreover, the user can interactively modify the seed points as needed in order to improve the segmentation results. We test our method on synthetic tensor field data and apply it to real DT-MR data providing segmentations of the corpus callosum in the brain and the ventricles of the heart.

4.1.1 Graph Cuts Overview

Suppose $G = (V, E)$ is an undirected graph with vertex set V and edge set E. As in the flow problem, two special terminal vertices denote the source s and the sink t. An edge in E connecting $u, v \in V$ is assigned a cost $c(u, v)$. An $s - t$ cut $C(S, T)$ partitions V into two disjoint sets S and T, such that $s \in S$ and $t \in T$. The cost of the cut is the sum of all edge costs connecting a vertex in S to a vertex in T:

$$C(S, T) = \sum_{u \in S, v \in T} c(u, v) \tag{4.1}$$

The minimum $s - t$ cut is the cut C with the smallest cost. Due to the theorem of Ford and Fulkerson [40], finding the minimum cut is equivalent to computing the maximum flow from the source to the sink, which is solvable in polynomial time [45]. While there are generalizations of the minimum $s - t$ cut problem that involve more than two terminals, such as the multiway cut problem [32], these generalizations are generally NP-hard.

Since each cut of a graph G has a cost associated with it, we may view the graph G as an energy function mapping from all cuts on G to the set of non negative real numbers. Any cut can be described by $|V|$ binary variables $x_1, ..., x_{|V|}$ corresponding to vertices in G (excluding the source and the sink), such that $x_i = 0$ when vertex $v_i \in S$, and $x_i = 1$ when $v_i \in T$. An energy ξ can be represented by G, where ξ is viewed as a function of $|V|$ binary variables $\xi(x_1, ..., x_{|V|})$, and whose value is equal to the cost of the cut defined by the configuration $x_1, ..., x_{|V|}$ ($x_i \in \{0, 1\}$). Such an energy function ξ can be efficiently

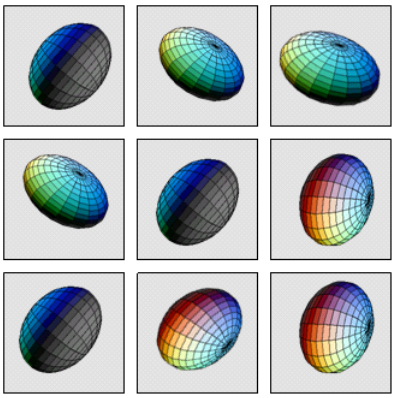

(a) Image before segmentation

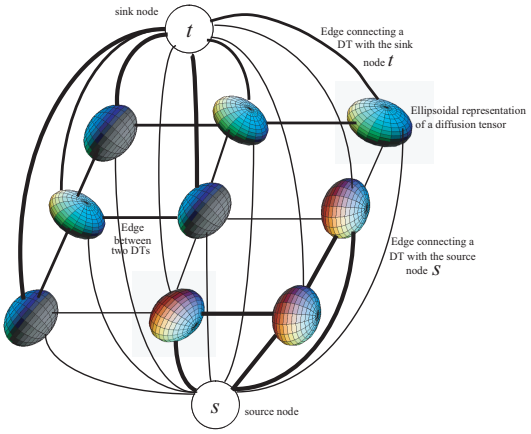

(b) Graph before minimum cut

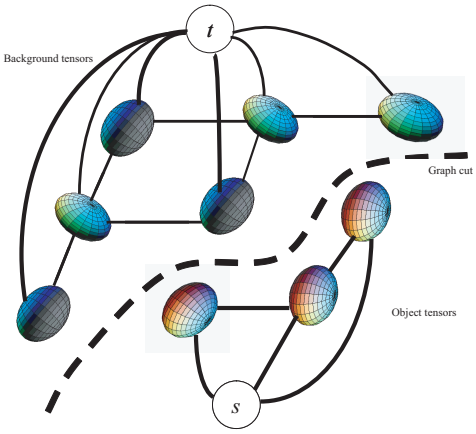

(c) Graph after minimum cut

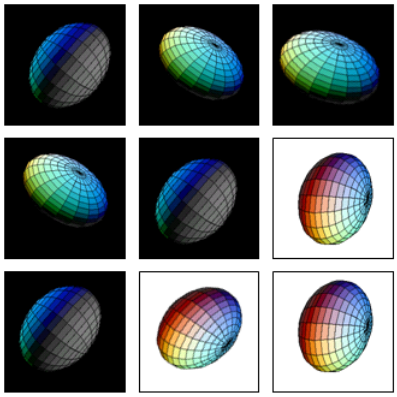

(d) Image after segmentation

Figure 4.1: (a) Simple illustration of graph construction from 2**D** 3×3 DT-MR image. (b) The cost of each edge is reflected by the edge's thickness. Low cost edges are attractive choices for the minimum cut. (c) The cut separates the tensors into object and background classes. (d) The 3**D** ellipsoids are used to visualize diffusion tensors where the directions and lengths of the major axes correspond to the eigenvectors and eigenvalues of the diffusion tensors.

minimized by computing the minimum cut of G or simply the "graph cut" [64].

The standard form of the energy function can be written as

$$\xi(x_1, ..., x_{|V|}) = \sum_{p \in \{1,2,...,|V|\}} \zeta_p(x_p) \; + \sum_{\substack{p,q \in \{1,2,...,|V|\} \\ v_q \in \mathcal{N}_p, q \neq p}} \zeta_{p,q}(x_p, x_q) \tag{4.2}$$

where $\mathcal{N}_p$ is the neighborhood of vertex v_p. The first term $\zeta_p(x_p)$ measures the cost of assigning a binary value x_p to a vertex v_p, which designates whether v_p belongs to the set S or T after the minimum cut is computed. From a segmentation point of view, this term is derived from the image data and is computed by measuring the similarity between the voxel corresponding to v_p and other known object or background voxels. The second term $\zeta_{p,q}(x_p, x_q)$ measures the cost of assigning x_p and x_q to the adjacent vertices v_p and v_q. Once again, from a segmentation point of view this cost reflects conformance to boundary properties. The cost function is computed in such a way that similar neighboring image voxels are associated with graph vertices that are connected by higher cost edges, whereas dissimilar voxels are associated with lower cost edges. At the borders of objects, adjacent voxels should have different labels and it is important that the energy function ξ does not over penalize such a labeling.

4.1.2 Scalar Image Segmentation Using Graph Cuts

As explained in the previous section, a cut is a binary partition of a graph and can be viewed as a labeling of the graph. Binary segmentation, which is a binary partition of image voxels, can therefore be performed by first creating a graph with vertices corresponding to the image voxels and edges with proper weights and then employing an efficient polynomial time minimum cut algorithms [45]. Boykov and Jolly [22] proposed an interactive technique for segmenting N-dimensional scalar images using graph cuts. In this method the user imposes hard constraints for segmentation by indicating certain pixels (seeds) that absolutely have to be part of the object and certain pixels that have to be part of the background. Intuitively, these hard constraints provide clues on what the user intends to segment. The rest of the image is segmented automatically by constructing a cost function whose minimization results in a globally optimum segmentation among all segmentations satisfying the hard constraints. The cost function is defined in terms of edges that form boundary and region properties. The boundary property ensures that voxels on either side of a boundary are

dissimilar while the region property ensures voxels belonging to the same region are similar to each other and dissimilar to voxels (seeds) known to belong to different image partitions. Similarity of voxels can be measured as differences of intensities.

4.1.3 Extending Segmentation Using Graph Cuts to DT-MR Images

In the case of DT-MR image segmentation using graph cuts, the user first selects certain tensor voxels belonging to the structure or object to be segmented and background tensor voxels belonging to the background. These seed tensors constitute hard constraints for the segmentation, i.e., after segmentation *obj* seeds must remain labeled as belonging to the object of interest while *bkg* seeds must remain labeled as background. Since typically more than one solution can satisfy these hard constraints, these conditions are considered insufficient for defining a single optimal segmentation and additional soft constraints are used to automatically label all remaining tensors in the image. The soft constraints are incorporated into the energy function through edge weights, reflecting both boundary and region properties.

Energy Function

Consider an arbitrary N-dimensional tensors field $\mathcal{T}$. Let $A = (A_1, A_2, ...A_{|\mathcal{T}|})$ be a binary vector that defines a segmentation of $\mathcal{T}$, where each element A_i specifies whether tensor D_i belongs to the object or background. This is the same as the binary labeling problem described in section 4.1 for which an energy functional can be constructed and minimized efficiently using graph cuts.

We define an energy functional $\xi(A)$ as [22]

$$\xi(A) = \lambda \cdot R(A) + B(A) \tag{4.3}$$

with

$$R(A) = \sum_{D_i \in \mathcal{T}} R_{D_i}(A_i), and \tag{4.4}$$

$$B(A) = \sum_{\substack{i,j \in \{1,2,...,|\mathcal{T}|\} \\ D_j \in \mathcal{N}_i, i \neq j}} B_{(D_i, D_j)} \tag{4.5}$$

where $\mathcal{N}_i$ is the set of tensors neighboring tensor D_i. The coefficient $\lambda \geq 0$ in Eq.(4.3) specifies a relative importance of the region properties term $R(A)$ versus the boundary properties

term $B(A)$. The boundary term $B_{(D_i,D_j)}$ is interpreted as the penalty for discontinuity between neighboring tensors (D_i, D_j). Normally $B_{(D_i,D_j)}$ is large when the neighboring tensors are similar and close to zero when they are dissimilar. The regional term $R(A)$ sums up the individual penalties $R_{D_i}(A_i)$ of assigning a tensor D_i as *obj* or *bkg* and is computed by examining the dissimilarity measure of tensor D_i compared to the *obj* and *bkg* seed tensors.

Graph Construction

We now construct a graph G as follows. Each tensor voxel of the DT-MR image corresponds to a non-terminal node in the graph. We add two terminal nodes, namely source s and sink t so that a flow is pushed from s to t (Fig. 4.1). Neighboring tensors (D_i, D_j) are connected by edges with edge weights of $B_{(D_i,D_j)}$. In our work we have considered 8-connectivity neighborhood for 2**D** data and 26-connectivity for 3**D** data. Moreover, each non-terminal node is connected to the terminal nodes with edge weights given as in table 4.1.

Table 4.1: Edge weight assignment table for the graph G

Edge	Weight	For
(D_i, D_j)	$B_{(D_i,D_j)}$	$(D_i, D_j) \in \mathcal{N}, D_j \in \mathcal{N}_i, i \neq j$
(D_i, s)	$\lambda R_{D_i}(bkg)$	$D_i \notin \mathcal{O} \cup \mathcal{B}$
	K	$D_i \in \mathcal{O}$
	0	$D_i \in \mathcal{B}$
(D_i, t)	$\lambda R_{D_i}(obj)$	$D_i \notin \mathcal{O} \cup \mathcal{B}$
	0	$D_i \in \mathcal{O}$
	K	$D_i \in \mathcal{B}$

where

$$K = 1.0 + \max_{D_i \in \mathcal{T}} \sum_{\substack{i,j \in \{1,2,\ldots,|\mathcal{T}|\} \\ D_j \in \mathcal{N}_i, i \neq j}} B_{(D_i,D_j)} \tag{4.6}$$

while $\mathcal{O}$ and $\mathcal{B}$ denote the set of *obj* and *bkg* seed tensors respectively.

The edge weight of a non-terminal tensor D_i to the source terminal node s is the penalty of assigning the tensor D_i as *bkg* tensor denoted by $R_{D_i}(bkg)$. Similarly, the edge weight of a non-terminal tensor D_i to the sink terminal node t is the penalty of assigning the tensor D_i as *obj* tensor denoted by $R_{D_i}(obj)$.

By assigning the weight K, which is greater than the sum of all edge weights of a seed tensor to its neighbors, to the edges connecting each *obj* and *bkg* seed points to s and t respectively, we ensure that the hard constraints of the segmentation will always remain

intact after segmentation. This comes from the fact that the minimum graph cut always severs the least weight edges. Moreover by definition, this cut will sever one and only one terminal link from each tensor, thus resulting in an optimal segmentation.

In order to fully utilize all the information in the tensors while computing the edge weights of the graph, the dissimilarity measure of tensors should incorporate both diffusion magnitudes and directions in the DT-MR image voxels. We utilize the Log-Euclidean tensor distance [5] and the J-divergence tensor dissimilarity measure [111] described in Chapter 3 for computing these edge weights.

We compute the boundary link weights $B_{(D_i,D_j)}$ as the inverse of tensor distance between D_i and D_j.

$$B_{(D_i,D_j)} = d^{-1}(D_i, D_j) \tag{4.7}$$

The weights of the terminal links connecting a non-seed tensor to the terminal nodes are obtained by computing the distance of each such tensor from all seed tensors and averaging these distances. Specifically, the edge weight of a non-seed tensor D_i to the source terminal node s, which is the penalty of assigning the tensor D_i as bkg tensor, is given by

$$R_{D_i}(bkg) = \frac{\sum_{D_j \in \mathcal{B}} d(D_i, D_j)}{|\mathcal{B}|} \tag{4.8}$$

Similarly, the weight of a non-seed tensors D_i to the sink terminal node t, which is the penalty of assigning the tensor D_i as obj tensor, is given by

$$R_{D_i}(obj) = \frac{\sum_{D_j \in \mathcal{O}} d(D_i, D_j)}{|\mathcal{O}|}. \tag{4.9}$$

4.1.4 Experimental Results

In this section, we present some simulation results of the proposed segmentation technique for both synthetic and real data. Both Log Euclidean and J-divergence tensor dissimilarity measures were tested and gave similar results.

Synthetic Data

Fig. 4.2 shows a noisy synthetic DT-MR image segmentation performed with the proposed technique. This example is used to demonstrate that full tensor information must be used to achieve quality segmentation for tensor fields. The inner circle contains anisotropic diffusion

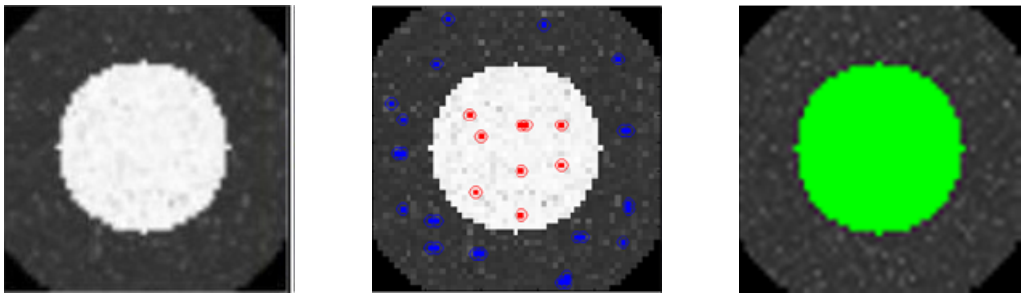

(a) Original image (b) Seeded image (c) Segmentation result

Figure 4.2: Segmentation of a noisy synthetic 2**D** DT-MR slice using graph cuts. (a) The DT-MR slice visualized using D_{xx}. The inner 'white' disk contains tensor pixels with eigenvectors $(1,0,0)$, $(0,1,0)$, and $(0,0,1)$ and corresponding eigenvalues $(10,1,1)$. The outer disk contains tensors with eigenvectors $(0,1,0)$, $(1,0,0)$, and $(0,0,1)$ and corresponding eigenvalues of $(10,1,1)$. Gaussian noise is then added to corrupt the eigenvalues and to rotate the eigenvectors. (b) Manually selected object seed points (red) and background seed points (blue). (c) Segmentation result shown in green.

with a preferred direction pointing left while the outer circle contains anisotropic diffusion tensors of the same magnitude with preferred direction of diffusion pointing downward.

In order to test the strength of our segmentation algorithm, random Gaussian noise was added independently to the three eigenvalues of the DT-MR image [119] in addition to random rotation (in azimuth and elevation) perturbing the three eigenvectors by the same amount to retain orthogonality. Scalar quantities derived from tensors such as FA would not discriminate such image as having distinct diffusion properties. By considering the diffusion direction in addition to the magnitude however, we could correctly interpret the image as having two distinct structures with entirely different diffusion properties and thus segmented the image accordingly.

In Fig. 4.3, we show that the proposed method is capable of segmenting an object of interest made up of several disconnected parts.

Real Data

While the synthetic example demonstrated the quality of segmentation results obtained by the proposed technique, the practicality of the proposed technique was evaluated using real brain and cardiac DT-MRI data as shown below. Although we present typical segmentation

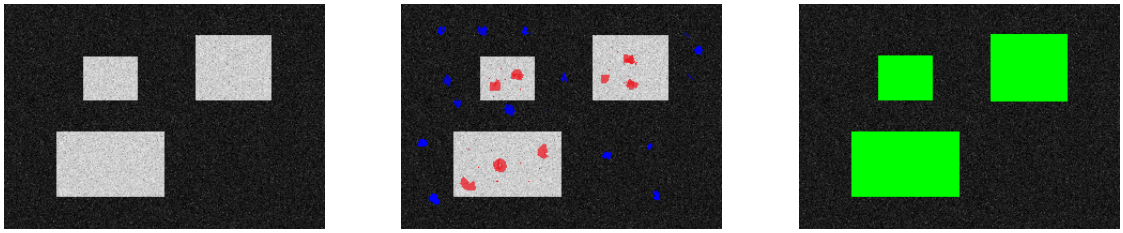

(a) Original image (b) Seeded image (c) Segmentation result

Figure 4.3: Segmentation of a synthetic noisy DT-MR slice containing an object comprising several disconnected parts using graph cuts. (a) The DT-MR slice visualized using D_{xx}. (b) Object (red) and background (blue) seed points. (c) Segmentation result in green. The tensors in the object and background were created in a manner similar to those in Fig. 4.2.

results for **2D** images, we have tested our method on several **2D** and **3D** and obtained similar results.

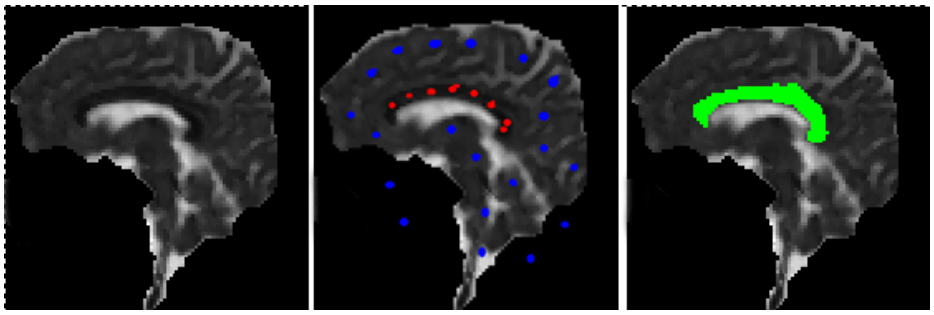

Figure 4.4: Corpus callosum (CC) segmentation using graph cuts from a DT-MR slice of the brain. From left to right: original image visualized using trace, manually selected CC seed points (red) and background seed points (blue), and CC segmentation result shown in green.

Fig. 4.4, shows the segmentation result of brain corpus callosum where white matter is segmented out from the remaining part of the brain. No regularization, smoothing or interpolation was performed prior to segmentation. Fig. 4.5 shows the segmentation result for the cardiac ventricles.

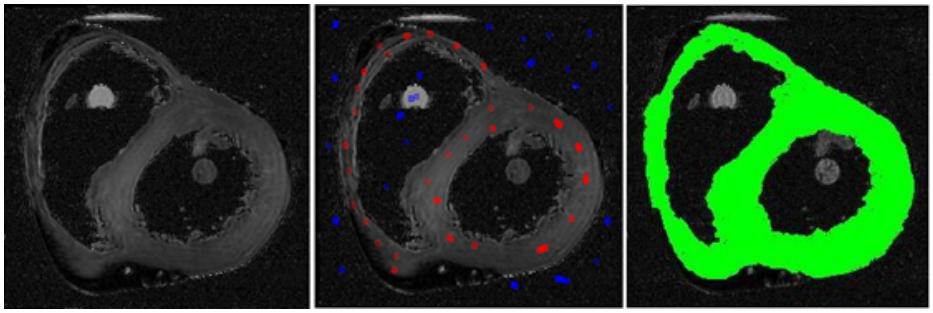

Figure 4.5: Cardiac wall segmentation from a DT-MR slice of the heart using graph cuts. From left to right: original image visualized using trace, manually selected heart seed points (red) and background seed points (blue), and cardiac segmentation result shown in green.

4.2 Segmentation using Random Walker

The Random Walker segmentation algorithm is performed by labeling each unlabeled image pixel with the label for which it has the highest probability. This is achieved by calculating the probability that a Random Walker, starting from an unlabeled pixel, first reaches a labeled pixel (seed point).

4.2.1 Random Walker Overview

Similar to graph cuts, the segmentation is carried out on a weighted graph which is constructed from the image to be segmented. A graph $G = (V, E)$ with vertices $v \in V$ and edges $e \in E$ is constructed from the image such that each vertex in the graph is a tensor voxel (D_i) from the image. Neighboring tensors (D_i, D_j) are connected by edges e_{ij} which have weights w_{ij}. As in graph cuts, the weights of the edges are computed using the Log-Euclidean and J-divergence tensor distance measures. An edge connecting two similar tensors should have a larger weight than an edge connecting two dissimilar tensors. Moreover, the user provides *obj* and *bkg* seed points that constitute hard constraints for the segmentation. Therefore, given the graph and a set of labeled vertices, the goal of the Random Walker algorithm is to label each unlabeled vertex V_U in the graph with a label s provided by the user [47]. Fig. 4.6 provides an illustration of how the graph is constructed from a DT-MR image using ellipsoids to visualize the diffusion tensors (voxels).

To find the probability x_i^s that a Random Walker starting from a vertex v_i first reaches a labeled node, the following energy functional has to be minimized [47]

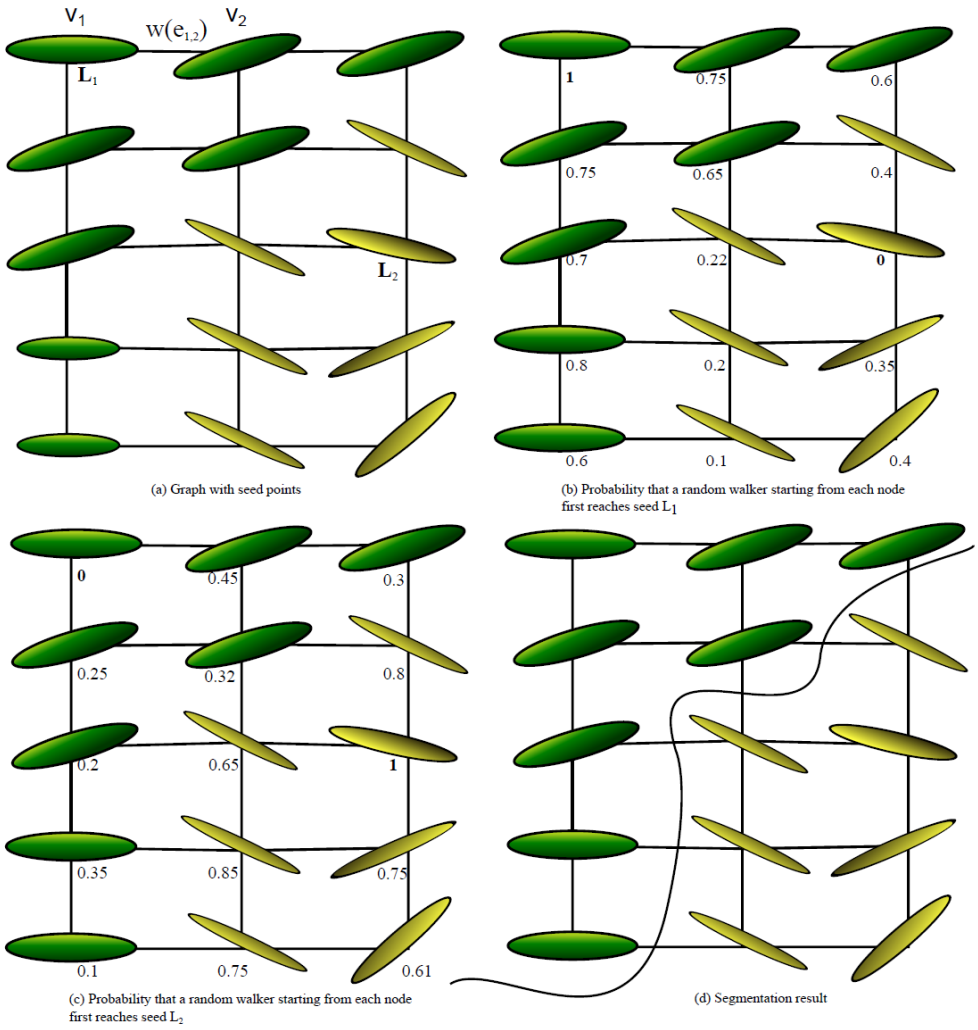

Figure 4.6: Simple illustration of the approach to segmentation using Random Walker with two seed points representing two labels (L_1, L_2). (a) Initial seed points where each node is a diffusion tensor visualized as ellipsoid. (b) and (c) Probabilities that a Random Walker starting from each node first reaches a seed. (d) Expected segmentation result.

$$E = x_U^{sT} L x_U^s \tag{4.10}$$

where s corresponds to a label and L represents the combinatorial Laplacian matrix defined as

$$L_{v_i,v_j} = \begin{cases} deg_{v_i} & \text{if } i = j \\ -w_{ij} & \text{if } v_i \text{ and } v_j \text{ are adjacent vertices} \\ 0 & \text{otherwise} \end{cases} \tag{4.11}$$

where deg_{v_i} is the degree of the vertex v_i. The Laplacian matrix can be partitioned into labeled (L) and unlabeled (U) vertices such that

$$L = \begin{bmatrix} L_L & B \\ B^T & L_U \end{bmatrix} \tag{4.12}$$

The minimization of the energy function Eq.(4.12) can then be achieved by solving the following system of equations

$$L_U x_U^s = -B f^s \tag{4.13}$$

where f^s is an indicator vector for the labeled vertices that defines the segmentation boundary.

4.2.2 Incorporating Label Priors

Without incorporating label prior models, the Random Walker formulation fails to segment disconnected objects since each segment must be connected to a seed [46]. From the user initialized *obj* and *bkg* seed regions, a tensor distribution can be calculated using a kernel density estimation, where for each tensor a nodewise prior P_i^s is calculated. The prior P_i^s represents the probability that the tensor at vertex v_i belongs to the tensor distribution of label s. Each label is assumed to be equally likely, therefore using Bayes' theorem the prior probability is given as

$$x_i{}^s = \frac{P_i{}^s}{\sum_{s=1}^k \lambda_i{}^s} \tag{4.14}$$

In vector form, this is written as

$$\left(\sum_{s=1}^{k} \Lambda^s \right) x^s = P^s \tag{4.15}$$

where Λ^s is a diagonal matrix with the values of P^s on its diagonal. This leads to the introduction of the priors into the system of equations given in Eq.(4.13) which are used to find the probabilities x_U^s. The new system of equations can be defined as

$$L_U + \gamma \sum_{r=1}^{k} diag\,(P_U^r) x_U^s = \gamma P_U^s - B f^s \tag{4.16}$$

where γ is a free parameter.

A Gaussian kernel is used to produce the probability density estimation. Given a set of k labeled tensors (seeds) $R^s = \{R_1^s, R_2^s, ..., R_k^s\}$ for each user defined label s, the probability P_i^s that a tensor D_i is generated from the seeds distribution corresponding to label s is given by

$$P_i^s = \sum_{q=1}^{k} exp\left(\frac{d^2(D_i, R_q)}{\sigma^2}\right) \tag{4.17}$$

where $d(D_i, R_q)$ is the tensor distance between a pair of tensors D_i and R_q, and σ is a free parameter.

4.2.3 Extending Random Walker Segmentation to DT-MR Images

For scalar images the following equation is used for mapping neighboring vertex intensities (I_i, I_j) to the weight of an edge connecting them

$$w_{ij} = e^{-\beta (I_i - I_j)^2} + \epsilon \tag{4.18}$$

In the case of DT-MR images, we modify the equation in order to incorporate appropriate tensor distance measures.

$$w_{ij} = e^{-\beta d^2(D_i, D_j)} + \epsilon \tag{4.19}$$

where ϵ is a small constant, β is a free scaling parameter, and $d(D_i, D_j)$ is the tensor dissimilarity measure between two tensors D_i and D_j.

4.2.4 Experimental Results

Synthetic data sets

In order to highlight the advantage of incorporating priors, we first present an experiment for a synthetic image made of several disconnected parts as shown in Fig. 4.7. Segmenting the image without the incorporation of prior models fails to detect all three disconnected

objects. Only the object that was seeded was segmented correctly. Additionally, we show the effect of changing the β parameter on the result of the segmentation. Using the same β parameter for both d_{LE} and d_{JD} metrics lead to different segmentation results.

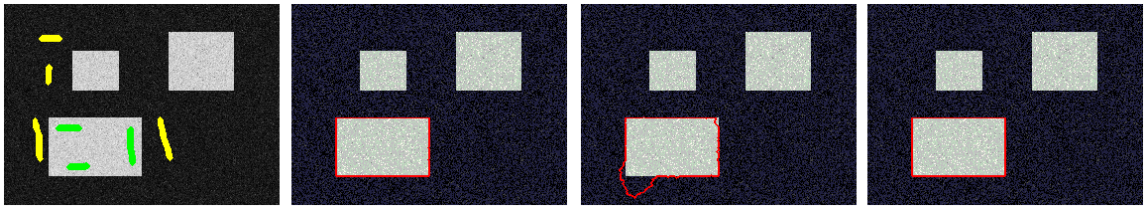

Figure 4.7: Segmentation of a noisy synthetic 2**D** DT-MR slice using Random Walker with several disconnected parts without incorporating priors. From left to right: initial image with seed points, segmentation result using Log Euclidean distance metric, segmentation result using J-divergence, and segmentation result using J-divergence after fine tuning of segmentation parameters.

The same image was segmented by incorporating prior models and the result of the segmentation is shown in Fig. 4.8. Again, only one of the disconnected objects was seeded. However, all three disconnected objects are detected and make up the result of the segmentation. Also, fewer seeds were needed as an input to obtain a correct segmentation. Only the Log Euclidean distance metric was used for the segmentations with prior models.

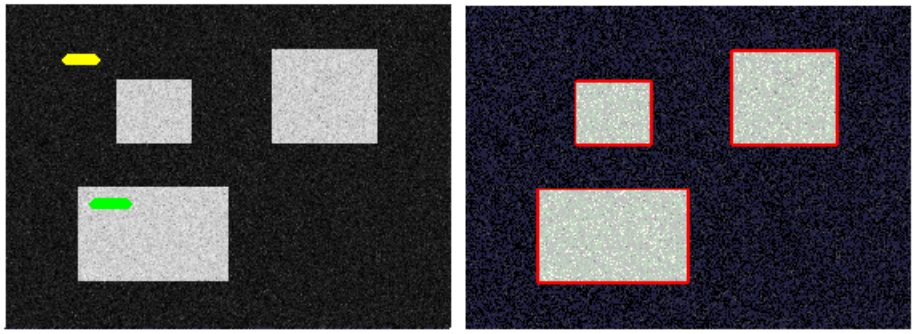

Figure 4.8: Segmentation of a noisy synthetic 2**D** DT-MR slice using Random Walker with several disconnected parts with priors.

Real data sets

In order to compare the Random Walker algorithm with Graph Cuts and highlight the advantage of priors in aiding the segmentation task, we now present results of applying the Random Walker algorithm to a DT-MR slice presented in Fig. 4.5 above. Without using prior models, the Random Walker segmentation technique failed to segment the cardiac wall accurately or needed too many seed points to give satisfactory results. When prior models are incorporated a satisfactory and expected segmentation was achieved with much fewer seed points as shown in Fig. 4.9. This demonstrates that using prior models not only makes the algorithm more resistant to noise but also fewer seed points are needed to achieve good segmentation, which makes the whole process faster.

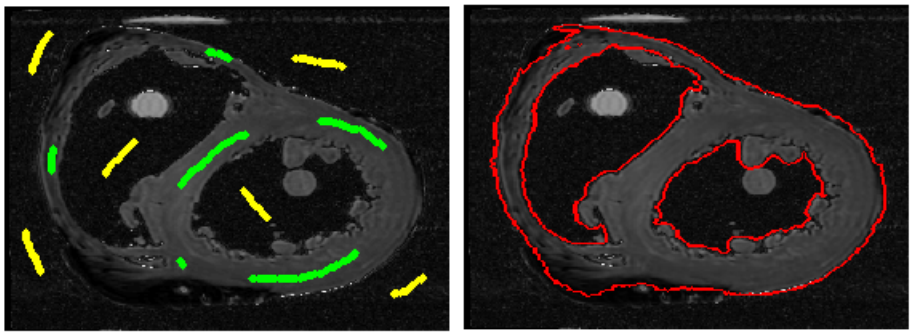

Figure 4.9: Cardiac wall segmentation from a DT-MR slice using Random Walker of the heart with prior models. Clearly fewer seed points are needed when incorporating prior models.

4.3 Conclusion

We extended the Graph Cuts and Random Walker segmentation algorithms that have been proposed for scalar images to segment DT-MR images. We made use of tensor calculus and tensor dissimilarity measures to define edge weights in the graphs. We applied the results to segmenting real and synthetic DT-MR data and obtained qualitatively satisfactory segmentations. Unlike extraction of scalar features from DT-MR images and then performing segmentation on the extracted features, our methods work directly on the tensor images.

This is useful because extracted features may be invariant to some transformation of the diffusion tensors. This is demonstrated in 4.2 where extracting FA would not distinct between the segmented regions. Moreover, graph cuts and Random Walker segmentation techniques are beneficial because they incorporate prior information in the form of hard constraints. This is useful in order to alter the segmentation task to get better results on the fly by adding more seeds. Finally, unlike level-set based methods that are sensitive to several parameter tunings and that use gradient decent based methods that may end up stuck at local optimal solutions, graph cuts and Random Walker algorithms have few parameters to tune and are guaranteed to get optimal solution for a given edge weighting tensor similarity measure. An important distinction between graph cuts and Random Walker is that the later takes into account local effects. This may give Random Walker technique an advantage in certain configurations; for example in trying to segment tensors that are configured in a slowly bending profile (say along the parameter of a circle) in to the same class. In this case, Random Walker may walk along bending tensors with ease because adjacent (local) tensors are similar although as we move further and further we may end up with completely different profile tensors. Since the far apart tensors will be dissimilar, graph cuts may not cluster them to the same class unless more seeds are added but Random Walker may be able to achieve the desired goal with fewer seeds.

4.4 Contribution

1. Yonas T. Weldeselassie and Ghassan Hamarneh. DT-MRI Segmentation Using Graph Cuts. In SPIE Medical Imaging, Vol. 6512-1K, pages 1-9, 2007.

2. Saba El-Hilo, Yonas T. Weldeselassie, and M. Stella Atkins. Second Order DT-MR Image Segmentation Using Random Walker. In SPIE Medical Imaging, Vol. 7962-162, pages 1-8, 2011.

Chapter 5

Clinical Application of DT-MRI

DT-MRI is useful for the generation and analysis of fiber-tract trajectories following the major eigenvectors of the diffusion tensors in soft fibrous tissues [16]. Combined with functional MRI, DT-MRI fiber tractography is also useful in the study of neuronal connectivity between active cortical areas in the brain [61]. Recently, DT-MRI fiber tractography has been extended for the analysis of several diseases [51, 73, 123, 25, 20].

Holodny et al. used DT-MRI to define the location and organization of cortico-spinal tracts in the posterior limb of the internal capsule [51]. Sandra et al. [73] used connectivity-based seed classification analysis to investigate the anatomical distribution of cortico-striatal pathways. In [123], Yoshikawa et al. demonstrate that patients with PD had significantly decreased FA in the region along a line between the substantia nigra and the lower part of the putamen/caudate complex, a region which includes the nigrostriatal dopaminergic pathway, a key site for degeneration in PD. Application of DTI fiber tracts was investigated in schizophrenia by Buchsbaum et al. [25] where diffusion tensor and structural MRI images were used to trace tracts from a region of interest in the anterior limb of the internal capsule to the prefrontal cortex. They concluded that patients with schizophrenia had tract paths that were significantly shorter in length from the center of the internal capsule to the prefrontal white matter.

A comprehensive quantitative analysis of change of diffusion measures and statistical analysis of healthy versus non-healthy subjects is given by Blain et al. [20]. The authors used diffusion tensor MRI to quantify and compare degeneration of the pons and cerebellar peduncles in multiple system atrophy, progressive supranuclear palsy, and Parkinson disease and to relate changes in diffusion measures to clinical features and localized atrophy. A

Region of Interest (ROI) approach was used to measure changes in FA and MD in the middle cerebellar peduncles, decussation of the superior cerebellar peduncles and pons.

Functional connectivity alterations in PD have also been demonstrated using Functional Magnetic Resonance Imaging (fMRI) [97], but demonstration of altered anatomical connectivity in vivo has only recently been made possible by the advance in diffusion tensor techniques. While the primary focus of neurodegeneration in PD is the nigrostriatal pathway, neuroimaging studies have demonstrated widespread altered function within cortico-striatal-thalamo-cortical loops in PD [33].

In this chapter, we investigate various features of white matter fiber tracts extracted from DT-MR images in the cortico-striatal region of the brain in control and PD subjects. After image acquisition, manual delineation of primary motor cortex and striatum, and generation of white matter fiber tracts connecting the primary motor cortex to the striatum, we collect features of interest and perform statistical analysis to see if such features can be used as markers in the classification of PD subjects from control subjects. In addition to the use of FA and MD, we investigate vector field measures of the major eigenvectors of the diffusion tensors namely divergence and curl. Our results show that PD subjects have significantly lower FA and MD and the major eigenvectors of control subjects have lower divergence.

5.1 Materials and Methods

Seventeen subjects were considered in this pilot study. We recruited nine PD subjects, mean age 61 years $\pm$ 9, 4 female, 5 male, 8 right handed, 1 left-handed. Patients were diagnosed with mild to moderate stage PD (Hoehn & Yahr stage 1-2.5). Data were compared to that from eight age-matched control subjects without neurological or psychiatric disorders, 4 male, 4 female, 7 right handed, 1 left handed.

We proceeded as follows: image acquisition, motion correction, DTI reconstruction, ROI delineation, fiber tracts generation, features extraction and statistical analysis of features.

5.1.1 Image Acquisition

Diffusion tensor images were acquired using a Phillips Achieva 3.0 Tesla scanner with slices parallel to the anterior-commissure posterior-comissure line. 60 continuous slices of 2.2 mm thickness were collected with a field of view (FOV) of 212 mm, pixel size 0.82 mm^2. 32 gradient directions were obtained with a total scan time of 248 seconds. Three separate DTI

scans were acquired for each subject and averaged during tensor reconstruction. Regions of interest were manually drawn on a high resolution T1-weighted structural MRI, FOV 240 mm, pixel size 1 mm^2, with 170 continuous slices acquired parallel to the commissural line.

5.1.2 Motion Correction

In order to minimize the effects of head motion during DTI image acquisition, we performed motion correction for the three DTI scans of each subject. This was done by rigidly aligning all the diffusion weighted images to the first base image S_o and rotating the gradient directions accordingly. A normalized correlation cost function, a gradient descent algorithm and sinc interpolation implemented in the CATNAP software [67] were used for this purpose. The diffusion tensors were also reconstructed using CATNAP software.

5.1.3 ROI Delineation

The ROIs, namely the primary motor cortex and striatum, were manually delineated by a trained research assistant, blinded to disease status, using Amira (Mercury Computer Systems, Berlin, Germany) on the structural MRI images for each subject. Boundaries of each ROI were selected according to a standard neurological atlas [102] and segmented using a semi-automated livewire approach.

In order to register the delineated ROIs from the structural MRI scans to the reconstructed DTI, we first co-registered the structural MRI images to scalar volumes (FA maps) extracted from the DTI volumes. For the registration, we used Amira software implementing a rigid transformation utilizing a Quasi-Newton algorithm to maximize the normalized mutual information. Once the structural MRI images are registered to the FA maps, the same spatial transformation parameters are used on the labeled ROIs in order to transform the ROIs coordinates to the DTI frame of reference.

5.1.4 Fiber Tract Generation

Fiber tracts were generated by seeding at the primary motor cortex with uniform density of one seed per voxel. The tracking is done following the major eigenvectors of the diffusion tensors using line integral convolution [80]. The tracking was stopped when either the turning angle of a fiber exceeds 45° or the diffusion approaches isotropy (FA < 0.25).

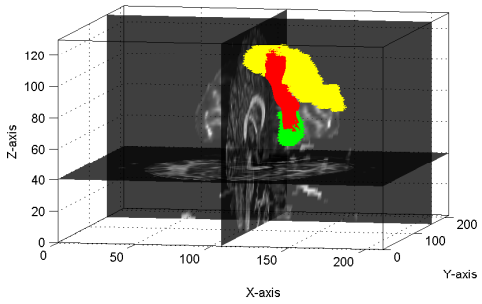

(a) Delineated left motor cortex (yellow), striatum (green) and Cortico-Striatal fiber tracts (red)

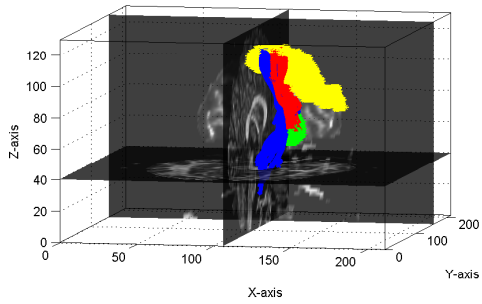

(b) Cortico-Striatal and Cortico-Spinal fiber tracts

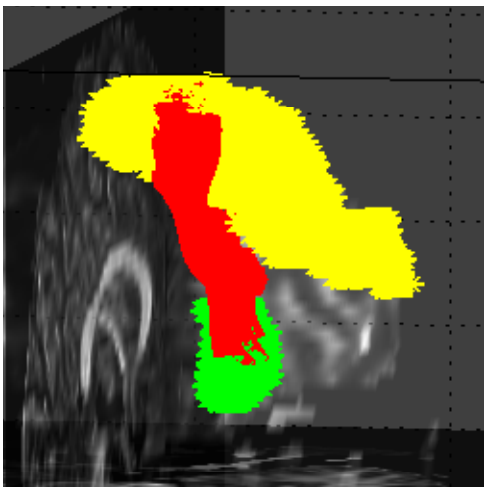

(c) Zoomed in Cortico-Striatal Fibers Bundle

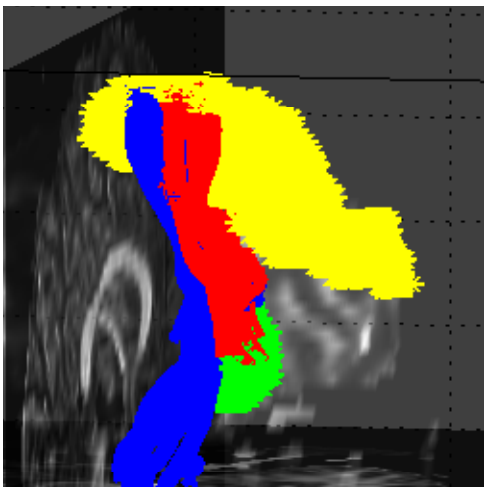

(d) Zoomed in Cortico-Striatal Fibers Bundle (Red) and Cortico-Spinal Fiber Tracts (Blue)

Figure 5.1: Delineated regions of interest and fiber tracts between the regions of interest. Cortico-Spinal fiber tracts are shown to emphasize that they are not included in the analysis.

Since fibers emanating from the motor cortex may or may not terminate at the striatum, we considered only those fibers that terminate at the striatum (cortico-striatal fibers), Fig. 5.1(a). This is done by first tracking all fibers by seeding at the motor cortex and then visually selecting those that terminate at the striatum. In Fig. 5.1(b), we show the cortico-striatal fibers together with non cortico-striatal fibers. To avoid clutter in the visualization, only cortico-striatal (red) and cortico-spinal tracts (blue) are shown.

5.1.5 Feature Extraction and Statistical Analysis

We extracted FA and MD from every point in the DTI volume through which the fiber tracts pass. Vector field features including Divergence (DIV) and curl of the major eigenvectors of the diffusion tensors are also analyzed. The curl is included to see if PD causes the geometry of fibers to change, i.e., if the curvature of tracts is changed; while the divergence quantity which measures the flux over a small boundary and indicates if a point is a source of flux or a sink is included to see if PD changes the diffusivity profile of a point in comparison with a small boundary around the given point.

Separate analyses were performed for FA, MD, major eigenvectors divergence and curl using unbalanced one-way analysis of variance (ANOVA) for comparing the means of the control and PD groups. We tested the null hypothesis that the mean values of the features extracted are drawn from the same population.

5.2 Experimental Results

The results of the one-way ANOVA test for FA, MD, DIV and Curl are shown in Fig. 5.2. We found reduced FA (p value of 0.06), reduced MD (p value of 0.04), and increased divergence (p value of 0.11) in PD compared to controls. The result of the curl feature was inconclusive.

5.3 Conclusion

We used cortico-striatal white matter fiber tracts and extracted diffusion and vector field features from DT-MR images in order to perform comparison of controls versus PD subjects. Our results show that PD subjects have significantly lower FA and MD values and their major eigenvectors have higher divergence values for tracts connecting primary motor cortex with the striatum. The changes suggest that secondary changes in the cortex, far from the

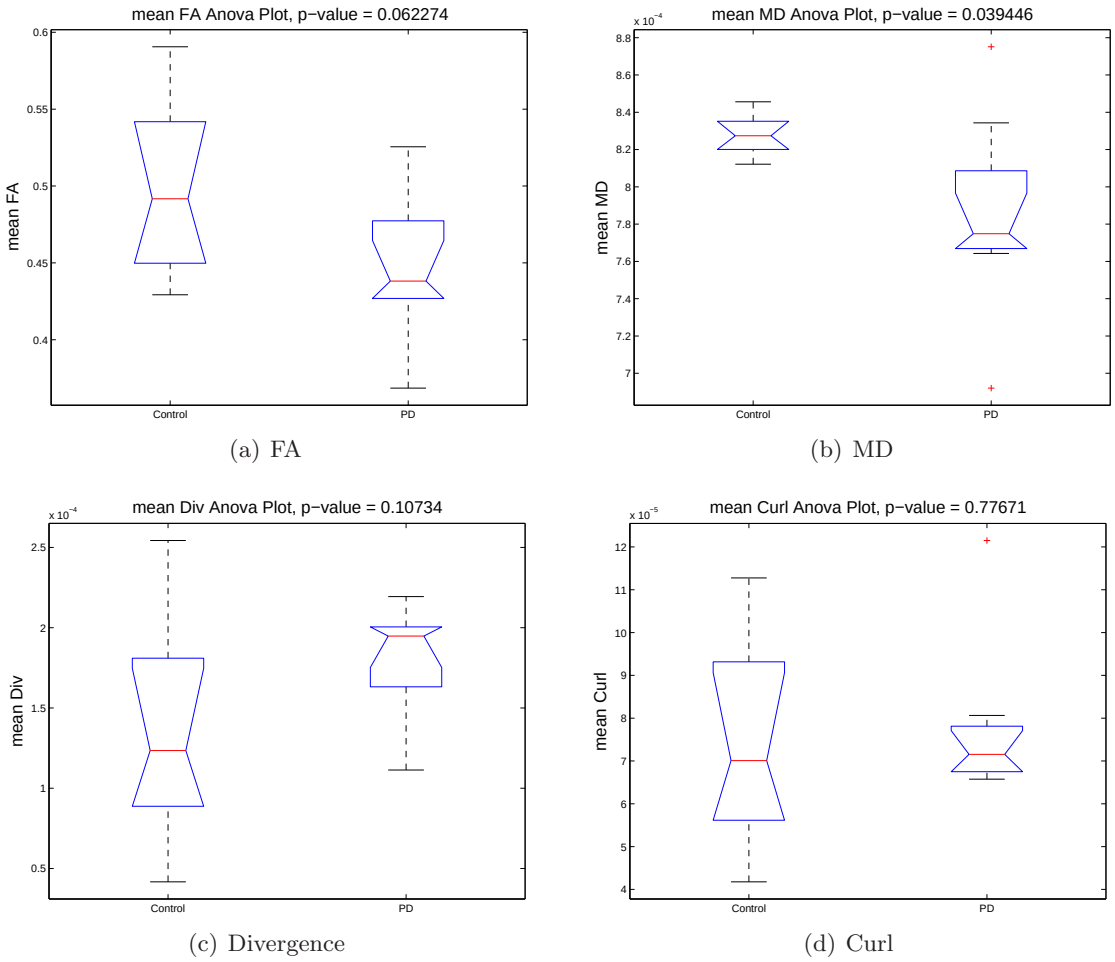

(a) FA (b) MD

(c) Divergence (d) Curl

Figure 5.2: Analysis of variance plots comparing the mean values of FA, MD, divergence and curl of the major eigenvectors between control and PD subjects

primary sites of pathology in PD, may be affected early on in the disease, possibly as a compensatory mechanism. The increase in the divergence of major eigenvectors among the PD patients may provide another sensitive marker for PD, in addition to the known significantly reduced FA and MD values. Despite the relatively small sample size, the results obtained are sufficiently encouraging to suggest that DTI features along the cortico-striatal region may be used to differentiate PD and control subjects.

5.4 Contribution

1. Yonas T. Weldeselassie, Ghassan Hamarneh, Samantha Palmer, Martin McKeown, and M. Stella Atkins. Diffusion Properties of Cortico-Striatal White Matter Tractography As Sensitive Markers of Parkinson's Disease. In The 17th Scientific Meeting and Exhibition of the International Society for Magnetic Resonance in Medicine (ISMRM), 2009.

Chapter 6

Fiber Orientation Distribution Functions

In all the previous chapters, 2^{nd}-order SPD tensors have been used to model the diffusivity profile at each voxel with the assumption of a single coherent fiber tract per voxel. This model, despite its simplicity and robustness, has been shown to be incorrect in regions containing intra-voxel orientational heterogeneity such as crossing and merging of fiber bundles [1, 3, 34, 35, 109, 108]. In order to highlight this shortcoming, we show how 2^{nd}-order and 4^{th}-order tensor models depict the ADC profiles of crossing fibers in Fig. 6.1 below. The synthetic DW-MR signals for these simulations were generated using a realistic diffusion MR simulation model proposed in [99] with b-value $= 1500s/mm2$ and 81 gradient directions. The data is of size 100×100 and contains a 40×40 box which is composed of simulated crossing fibers with orientations of $[1,\ 0,\ 0]$ and $[0,\ 1,\ 0]$. The box is surrounded by simulated crossing fibers with orientations of $[0.7071,\ 0.7071,\ 0]$ and $[0.7071,\ -0.7071,\ 0]$. The 2^{nd}-order tensor model fails to correctly represent the fiber crossings and instead shows all the tensors in the image as being planar. It fails to distinguish the inner box from the surrounding fibers. Whereas, the 4^{th}-order tensor model not only can it depict crossing fibers but it also can differentiate between both regions; albeit with wrong orientations (see section 6.3.1 and Fig. 6.3 for more details). Note that to avoid tensor cluttering, we plot the tensors at intervals of 10.

Several methods have been proposed to overcome the single fiber orientation limitation of 2^{nd}-order tensors. In [109], Tuch et al. proposed the use of diffusion imaging with diffusion

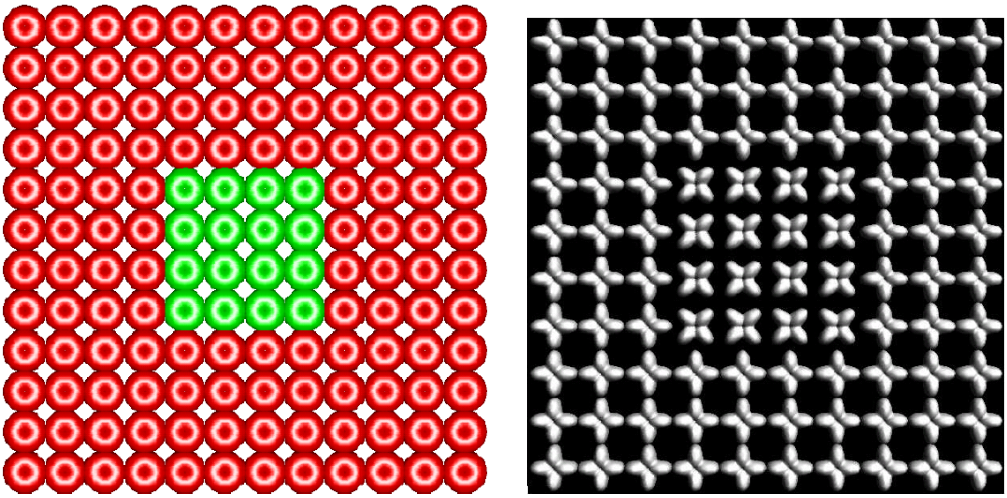

(a) 2^{nd}-order tensor model (b) 4^{th}-order tensor model

Figure 6.1: ADC profiles of crossing fibers depicted with 2^{nd}-order and 4^{th}-order tensor models visualized as spherical functions. Different colors are used in 6.1(a) to highlight the two distinct regions.

weighting gradients applied along many directions distributed almost isotropically on the surface of the unit sphere, a method known as HARDI. In contrast to rank 2 tensors, this method does not assume any a priori knowledge about the diffusivity profile. A number of approaches have been proposed to compute the ensemble-average diffusion propagator P(r, t) of HARDI data. These methods include Diffusion Spectrum Imaging (DSI) [114], Q-ball Imaging (QBI) [107], and Diffusion Orientation Transform (DOT) [87]. These methods, collectively known as q-space imaging techniques, identify multiple fiber components by calculating the Probability Distribution Function (PDF) of the diffusion process in each voxel based on the Fourier transform relationship between the PDF of diffusion displacement and the diffusion weighted signal attenuation in q-space. DSI performs a discrete Fourier transform to obtain $P(r, t)$, which requires a time intensive Cartesian sampling in q-space and hence is impractical for routine clinical use. The QBI method takes measurements on a q-space ball and approximates the radial integral of the displacement PDF by the spherical Funk-Radon transform. One problem with QBI is that the estimated diffusion Orientation Distribution Function (ODF) is modulated by a zeroth-order Bessel function that induces spectral broadening of the diffusion peaks. DOT computes the PDF at a fixed radius by expressing the Fourier transform in spherical coordinates and evaluating the radial part of

the integral analytically assuming the signals decay can be described by either a mono or a multi-exponential model. In [87], the authors show that the PDF values on a fixed radius can be reconstructed either directly or parametrically in terms of a Laplace series and claim that their technique can be regarded as a transformation of diffusivity to probability profiles whose peaks correspond to distinct fiber orientations. When the signals decay is described by a multi-exponential model, the DOT technique requires data acquisition over multiple concentric spheres, a time consuming proposition.

An important limitation of QBI methods is that they do not enforce the estimated ODF to be non-negative, which can cause the estimated ODF to have negative values; a situation that does not obey the underlying principle of diffusion. Goh et al. [44] proposed the use of spherical harmonic representations to pose the ODF estimation problem as a convex optimization problem, minimizing the cost function with a coordinate descent method. While the authors claim that their method results in sharp diffusion ODFs, the estimated ODF is constrained to be non-negative and a proper PDF (summing up to one); it remains to be seen how this method may be extended to multiple q-shell reconstruction method such as the one proposed in [1].

To overcome this limitation, Tournier et al. [105, 104] proposed a constrained spherical deconvolution method to directly estimate the FOD from DW-MRI data and reduced the occurrence of negative values, albeit not completely eliminating them. A careful distinction needs to be made between the two different concepts of diffusion ODF and fiber FOD functions, although both have similar acronyms in the DW-MRI research community. While QBI techniques model the diffusion ODF, which is the radial marginal distribution of the diffusion PDF or ensemble average propagator (EAP) which in turn is the Fourier Transform of the diffusion signal; the technique by Tournier et al. [105, 104] models FOD based on a deconvolution of a diffusion signal with a response function. The ODF model holds true when the signal is acquired using the short gradient pulse assumption. Moreover, the ODF model does not really indicate fiber orientations but rather the primary diffusion orientations and therefore is known to have broad peaks (which is also partially due to the modulation of the Bessel function). Further, the ODF model is a concept from the q-space formalism that establishes the Fourier relationship between the diffusion signal and the diffusion PDF. The FOD on the other hand is a deconvolution of the diffusion signal with a response function that indicates fiber orientations and needs to make no assumptions such as the narrow gradient pulse in the acquisition process and neither does it require a Fourier relationship

between the diffusion signal and the diffusion PDF. The FOD can also be computed by first computing an ODF from a QBI acquisition scheme and then deconvolving the ODF with a response function that represents the ODF for a single fiber [36].

Another approach for multi-fiber reconstruction is to describe the ADC by HOT (e.g. 4^{th} and 6^{th}) that generalize the 2^{nd} order tensors and have the ability to approximate multi-lobed functions [86]. Several methods have been proposed for estimating 4^{th} order tensors with positive definite constraints [9, 10, 42] as well as for processing HOT fields [122]. This approach is attractive not only because the rich set of processing and analysis algorithms developed for 2^{nd}-order tensor fields can be extended for HOT, but also the local maxima of HOT can easily be computed due to their simple polynomial form. The polynomial form of spherical functions represented as HOT gives a significant algorithmic benefit to compute the local maxima and minima, compared to the equivalent spherical harmonics basis that need techniques such as finite difference, spherical Newtons method or Powell's conjugate gradient descent method. With the exception of the finite difference method, whose accuracy is limited to the mesh size, these methods are numerical minimization problems and thus care must be taken to avoid small local maxima and to ensure convergence [21, 98, 43]. See also [56] for more detailed descriptions of diffusion MRI and the methods described above.

Unfortunately, the use of HOT has been confined so far to the estimation of tensor ADC profiles, although the local maxima of ADC profiles estimated using HOT generally do not match the underlying fiber bundle orientations for the intravoxel crossing fibers [3, 110, 124]. See also Fig. 6.1 above. In this chapter, we propose the use of SPD HOT to model FOD profiles and present a novel method for estimating the tensor field of FOD profiles from a given set of DW-MR images. Moreover, we extend our method of tensor distance induced diffusion anisotropy measures developed in Chapter 3 in order to derive anisotropy measure computed directly from Cartesian Tensor Fiber Orientation Distribution (CT-FOD) profiles with the use of appropriate HOT distance measure. The novelty of this chapter is therefore to use HOT to model the FOD functions and derive anisotropy measure directly computed from FOD functions.

In our technique the FOD is modeled by a Cartesian tensor basis using a parametrization that explicitly enforces the positive definite property to the computed FOD functions. The computed CT-FOD are SPD tensors whose coefficients can be efficiently estimated by solving a linear system with non-negative constraints. We evaluate our method qualitatively and quantitatively to demonstrate the superiority of the proposed technique over several existing

multi-fiber reconstruction methods. It is also recently reported that estimating positive semidefinite 4^{th}-order tensor ODFs can be achieved by minimizing an objective function subject to linear constraints by solving a linear programming problem that enforces non-negativity to computed ODFs [55].

There are three main contributions in this chapter:

- We present a novel method for positive-definite CT-FOD estimation from DW-MR images. To the best of our knowledge there is no existing FOD model in the literature that imposes explicitly the positivity property to the estimated FOD, which is naturally a positive-valued spherical function.

- We present a useful application of our method for converting HOT ADC profiles to CT-FOD. We should emphasize that this is an essential task since the maxima of HOT do not correspond to the underlying fiber orientations. On the other hand, our method computes CT-FOD whose maxima can be computed analytically and correspond to the true diffusion orientations.

- We derive a rotationally invariant AI with range [0,1) defined directly on CT-FOD which consolidates the whole analysis pipeline of diffusion imaging using solely CT-FOD.

6.1 Method

6.1.1 Symmetric Positive-Definite Cartesian Tensors of Even Orders

Any spherical function $f(\mathbf{g})$ can be approximated by an $L-th$ order Cartesian tensor as:

$$f(\mathbf{g}) \approx \sum_{i_1=1}^{3} \sum_{i_2=1}^{3} \cdots \sum_{i_L=1}^{3} g_{i_1} g_{i_2} \cdots g_{i_L} \mathbf{C}_{i_1,i_2,\cdots,i_L} \tag{6.1}$$

where g_i is the $i-th$ component of the 3-dimensional unit vector $\mathbf{g}$, and $\mathbf{C}_{i_1,i_2,\cdots,i_L}$ are the coefficients of an $L-th$ order tensor.

When approximating certain spherical functions in DT-MRI, we are interested in tensors of even orders with full symmetry, due to the antipodal symmetric nature of the DW-MR signal acquisition. In this case of symmetry, those tensor coefficients which correspond to the same monomial $g_1^a g_2^b g_3^c$ are equal to each other (e.g. $\mathbf{C}_{2,2,2,1} = \mathbf{C}_{2,2,1,2} = \mathbf{C}_{2,1,2,2} =$

$\mathbf{C}_{1,2,2,2}$, since they all correspond to the monomial $g_1 g_2^3$).

Notation:- *The Einstein's notation of $L-th$ order tensors as $C_{i_1,i_2,\cdots,i_L}$ has been commonly used in literature. But in this notation, one needs to explicitly specify the constraints of symmetry as in the case of $C_{2,2,2,1} = C_{2,2,1,2} = C_{2,1,2,2} = C_{1,2,2,2}$ above. In order to avoid such explicit specification of symmetry constraints, we will adopt an alternative notation that incorporates such symmetry constraints more naturally. In this new notation, the coefficient of an $L-th$ order tensor corresponding to the monomial $g_1^i g_2^j g_3^k$ is denoted by a single term $C_{i,j,k}$ with $i+j+k = L$ and the spherical function in Eq.(6.1) can more naturally be written as:*

$$f(\mathbf{g}) \approx \sum_{i+j+k=L} g_1^i g_2^j g_3^k \mathbf{C}_{i,j,k} \qquad i,j,k \ \in \ \{0,1,...,L\} \tag{6.2}$$

Using this alternative notation, the fifteen unique coefficients of 4^{th}-order SPD tensors are $\boldsymbol{C}_{400}$, $\boldsymbol{C}_{310}$, $\boldsymbol{C}_{301}$, $\boldsymbol{C}_{220}$, $\boldsymbol{C}_{211}$, $\boldsymbol{C}_{202}$, $\boldsymbol{C}_{130}$, $\boldsymbol{C}_{121}$, $\boldsymbol{C}_{112}$, $\boldsymbol{C}_{103}$, $\boldsymbol{C}_{040}$, $\boldsymbol{C}_{031}$, $\boldsymbol{C}_{022}$, $\boldsymbol{C}_{013}$, and $\boldsymbol{C}_{004}$. Their corresponding terms using Einstein's notation are $\boldsymbol{C}_{1111}$, $\boldsymbol{C}_{1112}$, $\boldsymbol{C}_{1113}$, $\boldsymbol{C}_{1122}$, $\boldsymbol{C}_{1123}$, $\boldsymbol{C}_{1133}$, $\boldsymbol{C}_{1222}$, $\boldsymbol{C}_{1223}$, $\boldsymbol{C}_{1233}$, $\boldsymbol{C}_{1333}$, $\boldsymbol{C}_{2222}$, $\boldsymbol{C}_{2223}$, $\boldsymbol{C}_{2233}$, $\boldsymbol{C}_{2333}$, and $\boldsymbol{C}_{3333}$ respectively. More importantly, note the correspondence that $\boldsymbol{C}_{i,j,k} = 4!/(i!j!k!)C_{i_1,i_2,\cdots,i_L}$. Example $\boldsymbol{C}_{400} = \boldsymbol{C}_{xxxx}$ but that $\boldsymbol{C}_{130} = 4\boldsymbol{C}_{xyyy}$ etc.

Furthermore, if the approximated function $f(\mathbf{g})$ is a positive-valued function, the Cartesian tensor should be positive-definite, i.e. $f(\mathbf{g}) > 0 \ \forall \ \mathbf{g} \in S_2$. Therefore Eq.(6.2) needs to be re-parametrized such that this positivity property is adhered to. In order to achieve this goal, we use the SPD HOT parametrization that has been recently proposed in [10, 8]. According to this parametrization, any non-negative spherical function can be approximated by a positive-definite L^{th} order homogeneous polynomial in 3 variables expressed as a sum of squares of $(L/2)^{th}$ order homogeneous polynomials $p(g_1, g_2, g_3; \mathbf{u})$, where $\mathbf{u}$ is a vector that contains the polynomial coefficients.

$$f(\mathbf{g}) = \sum_{j=1}^{M} \lambda_j p(g_1, g_2, g_3; \mathbf{u}_j)^2 \tag{6.3}$$

The parameters λ_j in Eq.(6.3) are non-negative weights. This parametrization approximates any given symmetric positive function and the approximation accuracy depends on

the order L and on how well the set of vectors $\mathbf{u}_j$ sample the space of unit vectors $\mathbf{u}$. It has been shown that by constructing a large enough set of well sampled vectors $\mathbf{u}_j$, we can achieve any desired level of accuracy [10].

6.1.2 Positive-Definite Cartesian Tensor FOD Profiles

The DW-MR signal for a given magnetic gradient orientation $\mathbf{g}$ and gradient weighting b, can be modeled using the standard multi-fiber reconstruction framework as follows

$$S(\mathbf{g}, b) = \int_{S_2} w(\mathbf{v}) B(\mathbf{v}, \mathbf{g}, b) d\mathbf{v} \tag{6.4}$$

where the integration is over all unit vectors $\mathbf{v}$, $B(\mathbf{v}, \mathbf{g}, b)$ is a basis function, and $w(\mathbf{v})$ is a non-negative spherical function that can be seen as a mixing/weighting function. There have been several proposed models for the basis function $B()$ such as a Rigaut-type function [54], von Mises-Fisher distribution [65] and others. The main problem with all of these models is that the integral in Eq.(6.4) cannot be computed analytically. Therefore, one needs to approximate the space of unit vectors $\mathbf{v}$ by a discrete set of vectors $\mathbf{v}_1, \cdots, \mathbf{v}_K$ in which case Eq.(6.4) is correctly discretized by $S(\mathbf{g}, b) = \sum_{k=1}^{K} w_k B(\mathbf{v}_k, \mathbf{g}, b)$ if and only if there are at most K underlying neural fibers that are oriented necessarily along the vectors $\mathbf{v}_k$. Another problem with the aforementioned discretization is that the function $w()$ is no more continuous over the sphere (it equals to w_k for $\mathbf{v}_k$ and it is zero everywhere else).

The main idea in this work is to avoid the above unnatural discretization of the space of orientations, by using a blending function $w()$, which can be appropriately decomposed so that:

1. $w()$ is positive-definite, and

2. $w()$ is continuous over the sphere.

In this work, we model such a blending function as an L^{th} order SPD tensor (say 4^{th}) by plugging Eq.(6.3) into Eq.(6.4) as follows

$$S(\mathbf{g}, b) = \int_{S_2} \sum_{j=1}^{M} \lambda_j p(v_1, v_2, v_3; \mathbf{u}_j)^2 B(\mathbf{v}, \mathbf{g}, b) d\mathbf{v} \tag{6.5}$$

where v_1, v_2, v_3 are the three components of the unit vector $\mathbf{v}$.

Given a data set of DW-MR signal attenuations S_i/S_0 associated with magnetic gradient orientations $\mathbf{g_i}$ and diffusion weighting b-value b, the coefficients of an L^{th} order positive-definite CT-FOD can be estimated by minimizing the following energy function with respect to the unknown polynomial-weighting coefficients λ_j

$$E = \sum_{i=1}^{N} \Big(S_i/S_0 - \sum_{j=1}^{M} \lambda_j \int_{S_2} p(v_1, v_2, v_3; \mathbf{u}_j)^2 B(\mathbf{v}, \mathbf{g}_i, b) d\mathbf{v} \Big)^2 \tag{6.6}$$

In order for the basis function $B()$ to reflect the signal attenuation of a single and highly oriented fiber response, we require the basis function to be a Gaussian that represents the diffusion process which is highly restricted perpendicular to the orientation $\mathbf{v}$. A common choice is the single fiber response which is described by the bipolar Watson function [31]

$$B(\mathbf{v}, \mathbf{g}, b) = \lim_{\delta \to +\infty} e^{-\delta(\mathbf{v}^T \mathbf{g})^2} \tag{6.7}$$

Here we should emphasize that the model in Eq.(6.7) agrees with the properties of the DW-MR signal response, i.e. it takes maximum and minimum values for diffusion sensitizing gradient orientations $\mathbf{g}$ that are perpendicular and parallel to the underlying fiber orientation $\mathbf{v}$ respectively. Moreover, δ is such that it captures information about b and mean diffusivity (D) and can be adjusted by altering either b or D. So this 'symmetry' can be simplified by using only δ in Eq.(6.7).

In order to compute the CT-FOD, we need to solve the minimization problem Eq.(6.6) for $\lambda_j' s$. This problem can be rewritten into an equivalent linear system problem $\mathbf{Bx} = \mathbf{y}$ where $\mathbf{x}$ is an M-dimensional vector of the unknown λ_j, $\mathbf{y}$ is an N-dimensional vector containing the given signal attenuations S/S_i and $\mathbf{B}$ is a matrix of size $N \times M$ with the elements $\mathbf{B}_{i,j} = \int_{S_2} p(v_1, v_2, v_3; \mathbf{u}_j)^2 B(\mathbf{v}, \mathbf{g}_i, b) d\mathbf{v}$. This linear system is solved for the non-negative $\mathbf{x}$ using the efficient Non-Negative Least Squares (NNLS) algorithm given in [68]. We can then easily compute the CT-FOD coefficients by multiplying the solution vector with a matrix $\mathbf{U}$, (i.e. $\mathbf{Ux}$), where the matrix $\mathbf{U}$ is of size $\frac{(2+L)!}{2(L!)} \times M$ that contains monomials formed by the vectors $\mathbf{u}_j$. Note that L is the order of the CT-FOD and $\frac{(2+L)!}{2(L!)}$ is the number of the unique coefficients in an L^{th}-order Cartesian tensor. In the case of 4^{th}-order CT-FOD, the multiplication $\mathbf{Ux}$ gives the 15 unique coefficients of a positive-definite tensor.

An interesting property of the NNLS optimization algorithm is that it produces sparse solution vectors and the sparsity depends on the rank of the basis matrix. In our particular case, although the problem seems significantly unconstrained, the solution vector contains at

most as many non-zero weights as the unknown tensor coefficients, which correspond to the rank of our polynomial basis matrix. Therefore if the finitely-generated set of polynomial basis contains a few thousand bases, the NNLS algorithm by definition will select only up to 6, 15, 28 for tensors of order 2, 4, and 6 respectively. Moreover the number of non-zero weights in the solution vector equals to the number of the unique unknown parameters of the symmetric tensor in each case. The sparsity of NNLS in comparison with other optimization techniques for modeling the DW-MR signal has also been studied in [53]. Therefore the degrees of freedom of our method is equal to the number of unknown tensor coefficients and it does not increase by the number of polynomial basis M but by the number of the unknown tensor coefficients.

We applied our proposed method for estimating 4^{th}-order CT-FOD ($L = 4$), using a set of $M = 321$ polynomial coefficients $\mathbf{u}_j$ and $\delta = 200$. Regarding the parameter δ, we performed several experiments using different values $\delta > 100$ and we obtained similar fiber orientations density profiles, which shows that our method is not sensitive to the selection of the value of δ.

6.1.3 Computing CT-FOD from HOT

Now, we present an application of our proposed framework for computing the coefficients of a CT-FOD from a given HOT and diffusion weighting b-value b, which is an essential task since the maxima of HOT do not correspond to the underlying fiber orientations. Given a HOT, the coefficients of the corresponding CT-FOD are computed by using the technique we presented in the previous section as follows

$$\mathbf{U}\mathbf{B}^{-1}exp(-b\mathbf{G}\mathbf{t}) \tag{6.8}$$

where the matrices $\mathbf{U}$ and $\mathbf{B}$ are as defined in the previous section, $\mathbf{G}$ is of size $N \times \frac{(2+L)!}{2(L!)}$ and contains only monomials constructed from N unit vectors $\mathbf{g}_i$ uniformly distributed on the unit sphere, and $\mathbf{t}$ is a vector of size $\frac{(2+L)!}{2(L!)}$ that contains the unique coefficients of the given HOT. For example, in the case of 4^{th}-order tensors, the 15 unique coefficients are given in the vector $\mathbf{t}$, and $\mathbf{G}$ is of size $N \times 15$. Also notice that $\mathbf{B}$ is not a square matrix and the matrix inverse $\mathbf{B^{-1}}$ corresponds to the solution provided by the NNLS algorithm and therefore is a specifically non-negative constrained solution, in contrast to the general pseudo-inverse solution.

6.2 Distance and Anisotropy measures of CT-FOD

6.2.1 Distance Measure

After estimating CT-FOD, it is important that we define a distance measure between pairs of CT-FOD, for example, in order to impose smoothness across the image lattice or to compute anisotropy measures. Since our CT-FOD are modeled as HOT (say 4^{th} order) SPD tensors which are isomorphic to homogeneous polynomial functions of the same order, one way to get a distance measure between CT-FOD $\mathbf{C}_i$ and $\mathbf{C}_j$ is to define the distance as the L_2 distance between the corresponding spherical functions $f_i(\mathbf{g})$ and $f_j(\mathbf{g})$ as follows:

$$d^2(\mathbf{C}_i, \mathbf{C}_j) = \frac{1}{4\pi} \int_{S_2} (f_i(\mathbf{g}) - f_j(\mathbf{g}))^2 dg \tag{6.9}$$

where $f_i(\mathbf{g})$ and $f_j(\mathbf{g})$ are defined as given in Eq.(6.2) and the integral is over all unit vectors $\mathbf{g}$, i.e., the unit sphere S_2.

Observe that this distance measure has the same mathematical form as the tensor distance measure defined between HOT in [9] when $f_i(\mathbf{g})$ and $f_j(\mathbf{g})$ are substituted with diffusivity functions. Denoting the fifteen components of $C_i - C_j$ by Δ_{xyz}, we get

$$\begin{aligned} d^2(\mathbf{C}_i, \mathbf{C}_j) = \frac{1}{315} \quad & \Big[(\Delta_{400} + \Delta_{040} + \Delta_{004} + \Delta_{220} + \Delta_{022} + \Delta_{202})^2 + \\ & 4[(\Delta_{400} + \Delta_{220})^2 + (\Delta_{400} + \Delta_{202})^2 + (\Delta_{040} + \Delta_{220})^2 + \\ & (\Delta_{040} + \Delta_{022})^2 + (\Delta_{004} + \Delta_{022})^2 + (\Delta_{004} + \Delta_{202})^2] + \\ & 24(\Delta_{400}^2 + \Delta_{040}^2 + \Delta_{004}^2) - 6(\Delta_{220}^2 + \Delta_{022}^2 + \Delta_{202}^2) + \\ & 2(\Delta_{400} + \Delta_{040} + \Delta_{004})^2 + (\Delta_{211} + \Delta_{031} + \Delta_{013})^2 + \\ & (\Delta_{121} + \Delta_{301} + \Delta_{103})^2 + (\Delta_{112} + \Delta_{310} + \Delta_{130})^2 + \\ & 2[(\Delta_{310} + \Delta_{130})^2 + (\Delta_{301} + \Delta_{103})^2 + (\Delta_{031} + \Delta_{013})^2] + \\ & 2(\Delta_{310}^2 + \Delta_{301}^2 + \Delta_{130}^2 + \Delta_{031}^2 + \Delta_{103}^2 + \Delta_{013}^2)\Big] \end{aligned} \tag{6.10}$$

6.2.2 Closest Isotropy

Given a CT-FOD $\mathbf{C}$, its closest isotropic CT-FOD $\mathbf{C}_{iso}$ is defined such that the distance $d(\mathbf{C}, \mathbf{C}_{iso})$ is minimum among all isotropic CT-FOD. The conditions for isotropy in the case of 4^{th}-order CT-FOD is:

$$\mathbf{C}_{iso} = \bar{\lambda}\, \mathbf{I}^s \tag{6.11}$$

for some $\bar{\lambda} \in \mathbb{R}^+$ and where $\mathbf{I}^s$ is a totally symmetric 4^{th}-order identity tensor [82]. In terms of components, $\mathbf{I}^s$ is given by

$$\begin{aligned} \mathbf{I}^s{}_{400} = \mathbf{I}^s{}_{040} = \mathbf{I}^s{}_{004} = 1 \\ \mathbf{I}^s{}_{220} = \mathbf{I}^s{}_{202} = \mathbf{I}^s{}_{022} = 2 \end{aligned} \tag{6.12}$$

and all remaining components equal to zero. Using this result and minimizing the distance $d(\mathbf{C}, \mathbf{C}_{iso})$ with respect to $\bar{\lambda}$, we obtain [83]

$$\bar{\lambda} = \frac{1}{5}(\mathbf{C}_{400} + \mathbf{C}_{040} + \mathbf{C}_{004}) + \frac{1}{15}(\mathbf{C}_{220} + \mathbf{C}_{202} + \mathbf{C}_{022}) \tag{6.13}$$

Observe that $\bar{\lambda}$ is actually the mean FOD of the CT-FOD $\mathbf{C}$ which is the same as saying the zeroth order CT-FOD that is closest to $\mathbf{C}$.

6.2.3 Anisotropy Measure

We now present an anisotropy measure derived from 4^{th}-order CT-FOD. This is important in order to consolidate the work of diffusion tensor imaging towards CT-FOD. Similar to the definition of FA for 2^{nd}-order tensors, we propose the use of the distance of a given CT-FOD from its closest isotropy normalized by the norm of the CT-FOD as our measure of AI. Defining the norm of a given CT-FOD as its L_2 distance from **ZERO**, we see that the non-negative function $d(\mathbf{C}, \mathbf{C}_{iso})/d(\mathbf{C}, \mathbf{0})$ can be used to infer AI. It is easy to see that this expression takes its minimum value of 0 when $\mathbf{C}$ is isotropic. In order to find its upper bound, it suffices to look at the limiting, but physically impossible, case of a non-zero diffusivity in only one direction, say along the direction $\mathbf{v} = (1, 0, 0)^T$ and zero diffusivities along all directions perpendicular to $\mathbf{v}$. In this case, all components of C except $\mathbf{C}_{400}$ will be zero and its mean FOD will be $\mathbf{C}_{400}/5$ resulting in an upper bound of $AI = 4/5$. In order to have an AI in the range $[0, 1)$, we would like to find a monotonic function that will map the interval $[0, \frac{4}{5})$ to $[0, 1)$. While several mapping functions can achieve this, in this work we chose a linear mapping and defined our anisotropy measure as

$$AI = \frac{5}{4}\Big(\frac{d(\mathbf{C}, \mathbf{C}_{iso})}{d(\mathbf{C}, \mathbf{0})}\Big) \tag{6.14}$$

We simulated several synthetic diffusion profiles comprising of isotropic, planar, linear and crossing fiber profiles in order to see the behavior of this anisotropy measure and compare it with existing measures.

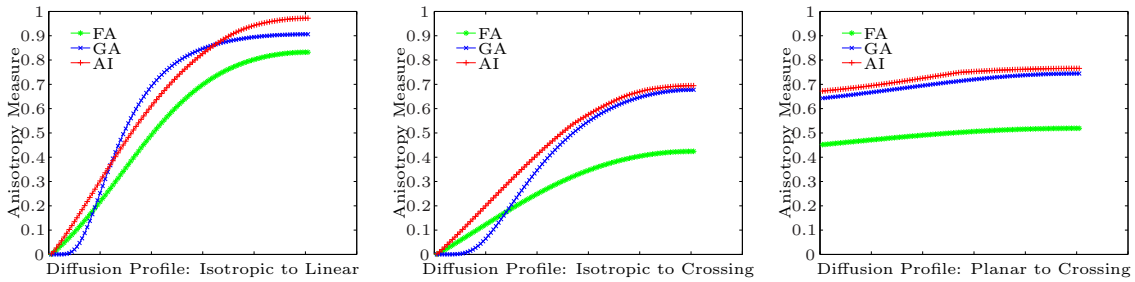

Figure 6.2: Comparison of FA, GA and our AI as diffusion profiles range from isotropic to linear (*left*), isotropic to two perpendicular crossing fibers (*middle*), and planar to two crossing fibers on the plane (*right*).

Fig. 6.2 shows anisotropy measures obtained by our AI, FA and Generalized Anisotropy (GA) as defined in [86]. The DW-MR signals for these simulations were generated using a realistic diffusion MR simulation model proposed in [99]. For the case of isotropic to linear diffusion profile (Fig. 6.2 *left*), we started with 321 crossing fiber orientations that uniformly sample the unit hemisphere with equal diffusivities and then gradually (*in 100 time steps*) restricted the diffusion in all directions except along one fiber orientation. In this configuration, while both FA and our AI show monotonically increasing values as we move from isotropic to linear diffusion, GA shows little changes at both isotropic and anisotropic regions with larger changes in the intermediate regions. As a result while the contrast of GA is concentrated between low and high anisotropies, the contrast in both FA and our AI is more or less uniform at all regions. Similarly, for the case of isotropic to two crossing fibers (Fig. 6.2 *middle*), we started with the same 321 fiber orientations with equal diffusivities and then gradually restricted diffusion in all directions except two perpendicular fiber orientations. The important observation in this case is the fact that both GA and our anisotropy measure give rise to larger values for crossing fibers while FA does not, which highlights the limitation of the 2^{nd}-order tensor model in regions of crossing fibers. Finally in the case of planar to two crossing fibers (Fig. 6.2 *right*), we started with 16 crossing fiber orientations on a plane that sample a circle uniformly and then restricted diffusion in all but

two perpendicular directions on the plane. As expected not only does FA gave rise to more or less uniform values in this configuration, but surprisingly both GA and our AI did so too, albeit with higher values. In other words, even though both 4^{th}-order tensor ADC and FOD models are able to model two crossing fibers, they do not distinguish as such between only two or more than two crossing fibers. This of course is the limitation of a 4^{th}-order tensor model when there are more than two crossing fibers. From the tractography point of view, where the AI is used for seeding and stopping criteria, both GA and our AI will be good indicators of presence of fibrous structures because they show a high anisotropy value in such regions (close to 0.7).

6.3 Experimental Results

In this section, we present experimental results of the proposed method applied to simulated, phantom, as well as a real DW-MR image from a human brain dataset.

6.3.1 Synthetic Dataset

In order to highlight the accuracy with which the maxima of estimated CT-FOD profiles coincide with the actual underlying fiber orientations, we first present qualitative results for the case of a synthetic dataset comprising of two crossing fiber bundles modeled as 4^{th}-order CT-FOD as shown in Fig. 6.3. We also include the results of ADC profiles modeled as 4^{th}-order tensors in order to highlight the performance of CT-FOD over ADC tensors of the same order. In this experiment, we start with two fiber bundles crossing at 90° degrees and then rotate one of the fiber orientations gradually until it aligns with the second fiber orientation resulting to a single fiber. The DW-MR signals for this simulated experiment were generated by simulating the MR signals using the model described in [99] with $b{-}value = 1500 s/mm^2$ and 81 gradient directions. Fig. 6.3(a) shows the result for a noise free case and Fig. 6.3(b) shows the results obtained when a Rician noise with std. dev.=0.02 is added to the simulated DW-MR signals. It is evident from these results that not only do CT-FOD profiles model the underlying structure better but they also have better noise immunity.

Next, we present quantitative results by presenting the deviation angles of the maxima of estimated CT-FOD with respect to the actual underlying fiber orientations. We consider the case of two crossing fibers whose orientations are $(\cos 20°,\ \sin 20°,\ 0)$ and $(\cos 100°,\ \sin 100°,\ 0)$ and the DW-MR signals are generated as described above. Six distinct Rician

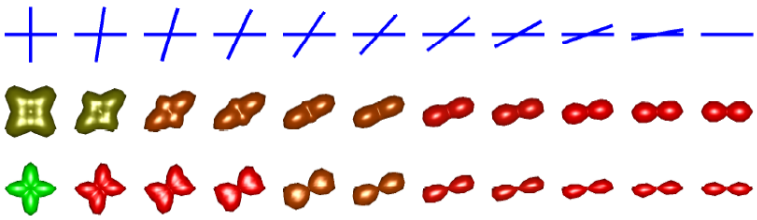

(a) Noise free. Top to bottom: schematic diagram of orientations, ADC profiles and FOD profiles.

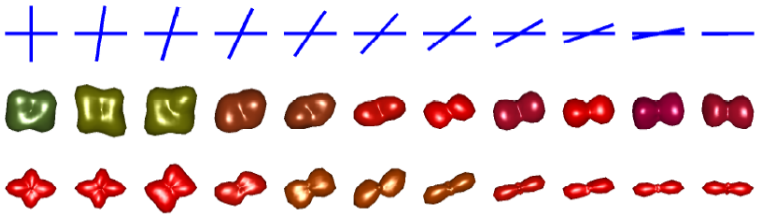

(b) Rician noise, std. dev.=0.02. Top to bottom: schematic diagram of orientations, ADC profiles and FOD profiles.

Figure 6.3: Alignment of maxima of estimated ADC and CT-FOD profiles with underlying fiber orientations.

noise levels were added to the simulated data and for each noise level the experiments were repeated 100 times. Fig. 6.4 shows a plot of the means and standard deviations of deviation angles between the actual fiber orientations and the maxima of estimated CT-FOD. In order to compare our results with spherical deconvolution techniques, we also include the results obtained using the MOW [54], QBI [107], DOT [87] and MOVMF [65] methods by computing the maxima of either the PDF or FOD profiles of the corresponding methods. For the particular noise level with std. dev.=0.08 the deviation angles for all the methods are reported in the adjacent table. Also notice that in this experiment the deviation angle of the computed orientations is compared to its closest actual fiber orientation because the crossing fibers are weighted equally in generating the MR signals. The results demonstrate the superiority of the proposed method over QBI, DOT, MOVMF and MOW methods.

Although we don't perform any explicit comparison here, it is worth mentioning that the least deviation angle result obtained using the spherical deconvolution method proposed by Tournier et al. [104] is about 7° - 8° on wider crossing fiber orientations while our method has achieved a least deviation angle result of 4.79°. Our method therefore performs as well as, or better than, Tournier's method.

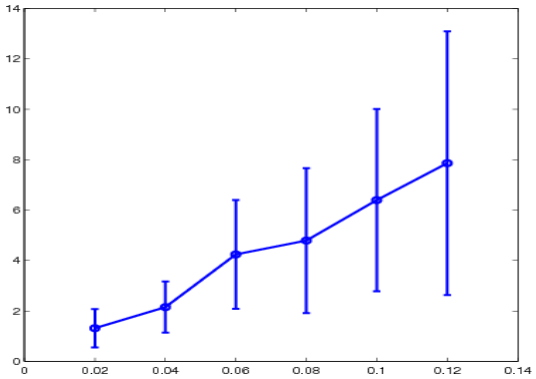

Table of errors (deg.)
noise st. dev. = 0.08

Method	Mean	St. dev.
QBI	9.13	±4.55
DOT	6.65	±3.72
MOVMF	5.62	±3.51
MOW	5.01	±2.96
CT-FOD	4.79	±2.87

Figure 6.4: Deviation angle in degrees ($y - axis$) between actual fiber orientations and maxima of estimated CT-FOD using a simulated 2-fiber crossing data with orientations ($\cos 20°$, $\sin 20°$, 0) and ($\cos 100°$, $\sin 100°$, 0) at different levels of Rician noise ($x - axis$).

6.3.2 Phantom Dataset

Here, we present our results for the publicly available HARDI phantom dataset whose ground truth fibers are known and was used in the MICCAI 2009 Fiber Cup contest [93]. The dataset consisted of 64 diffusion weighted images and one S_o volume acquired in two different spatial resolutions: $3 \times 3 \times 3mm^3$ and $6 \times 6 \times 6mm^3$ and three different b-values: 650, 1500 and 2650 $s/mm2$. We used the $3 \times 3 \times 3mm^3$ resolution dataset with a b-value of $650s/mm2$. Fig. 6.5(a) shows generalized anisotropy while Fig. 6.5(b) gives a zoomed in visualization of 4^{th}-order CT-FOD computed for the box shown in red. Clearly the 4^{th}-order CT-FOD correctly depicts the fiber organization of crossings as well as single fiber orientations.

6.3.3 Real Dataset

Here, we present CT-FOD computed from a real dataset consisting of a human brain dataset. The dataset consists of 63 continuous slices of 2.0 mm thickness with a FOV of $256 \times 256mm^2$ and pixel size of $2 \times 2mm^2$. 10 images were collected without diffusion weighting ($b \sim 0s/mm^2$) which were averaged during the CT-FOD reconstruction for a single average So image, and 99 diffusion weighted images are acquired in 99 gradient directions. Each of these image sets used different diffusion gradients with b values of approximately $3000s/mm^2$. Fig. 6.6(a) and Fig. 6.6(b) respectively show the proposed AI and 4^{th}-order CT-FOD field computed using our method. For comparison purposes, included are GA and 4^{th}-order

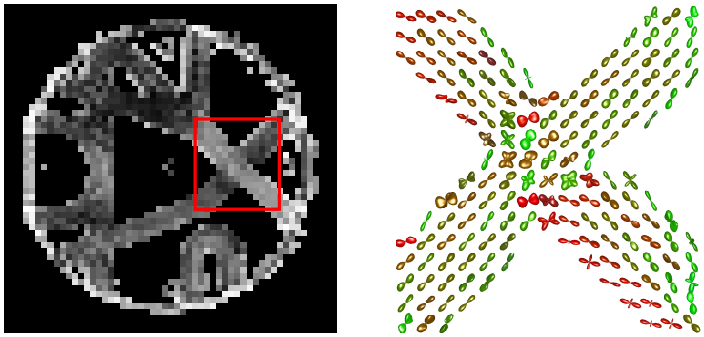

(a) Generalized anisotropy. (b) 4^{th}-order CT-FOD.

Figure 6.5: Generalized anisotropy and 4^{th}-order CT-FOD for the fibercup phantom data. Crossing of fiber orientations is clearly depicted as expected.

ADC fields as shown in Fig. 6.6(c) and Fig. 6.6(d) respectively. As can be verified in the anisotropy images, the branching, bending and crossing of tracts are better depicted by the computed CT-FOD field as compared to the ADC field. Moreover, unlike the GA map which reveals the white matter region with higher contrast but fails to distinguish the gray matter from the background, the proposed anisotropy map reveals both white matter and gray matter regions more clearly, albeit with less contrast.

Based on our preliminary CT-FOD results [117] and in conjunction with their techniques, Jiao et al. [55] have already shown that the proposed CT-FOD model improves tractography results and accurately detects fiber crossings, splits and kisses. Another potential fiber tracking algorithm that may be used in conjunction with CT-FOD is the spin glass based framework to untangle fiber crossings [29].

6.3.4 Tissue discrimination with GA and AI

Finally, we present a quantitative comparison of the anisotropy index derived from CT-FOD with generalized anisotropy in discriminating different tissue classes in a brain image. For the task of discriminating between two tissue classes, a measure of diffusion anisotropy, A, can be evaluated using a detectability index [2],

$$d = \frac{< A_1 > - < A_2 >}{\sqrt{\sigma_1^2 - \sigma_2^2}} \tag{6.15}$$

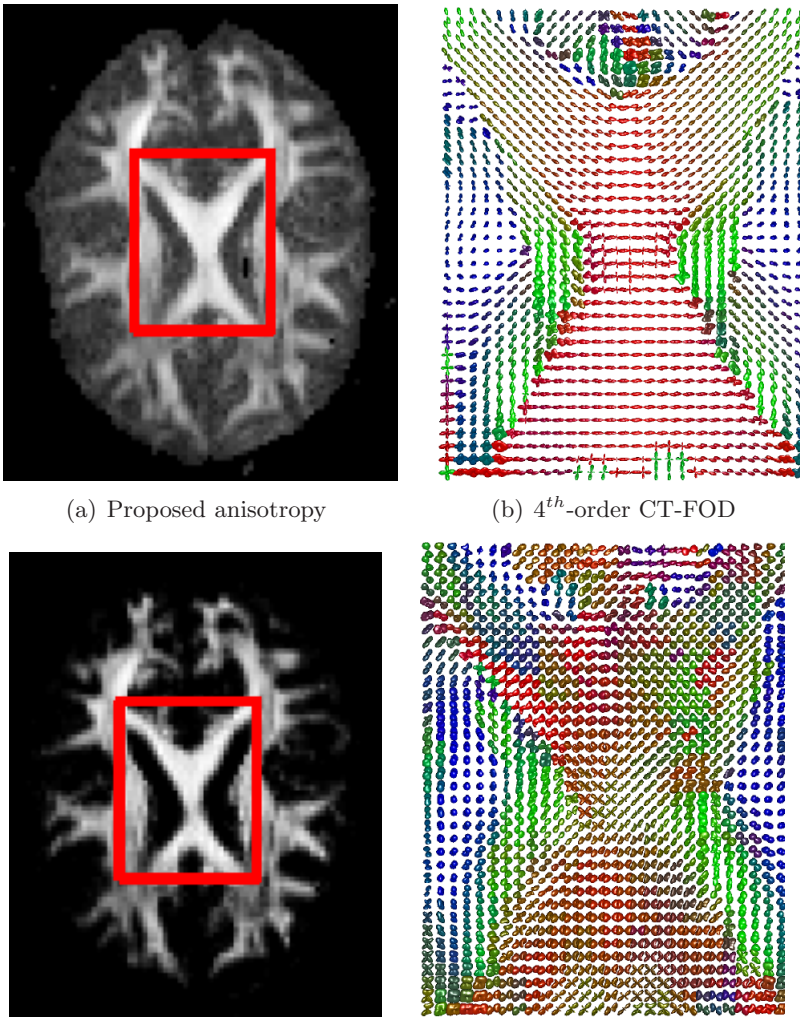

(a) Proposed anisotropy (b) 4^{th}-order CT-FOD

(c) GA (d) 4^{th}-order ADC

Figure 6.6: 4^{th}-order CT-FOD and ADC tensor fields computed from human brain slice and their corresponding anisotropy measures.

where ($< A_1 >$, σ_1^2) and ($< A_2 >$, σ_2^2) are the means and variances of the anisotropy values for the two tissue classes. The anisotropy measure with the greatest detectability index should be close to optimum for the specified task.

In order to compare GA and AI in discriminating tissue classes, we calculated the detectability indices of these anisotropy measures for the dataset described in section 6.3.3 above. The brain was parcellated using a publicly available white matter parcellation map (JHU_MNI_SS_WMPM_TypeI) downloaded from Johns Hopkins Medical Institute Laboratory of Brain Anatomical MRI. The GA and AI maps of our dataset were registered to the white matter parcellation map using FA map that was came with the parcellation map and was already registered to it. An affine registration was performed using the DiffeoMap software downloaded from the same source. Figure 6.7 shows the publicly available FA map with five regions of interest segmented. Our tissue detectability results for the regions of

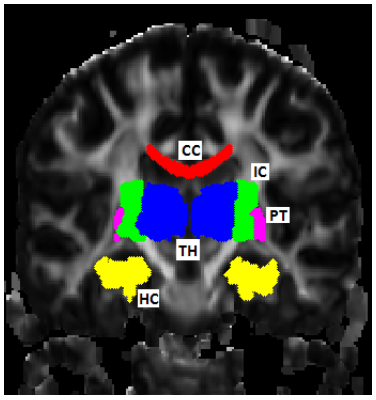

Figure 6.7: Single slice of FA map from JHU_MNI_SS DTI dataset with corresponding regions of interest segmented using JHU_MNI_SS_WMPM_TypeI white matter parcellation map: CC = Corpus Callosum, IC = Internal Capsule, TH = Thalamus, HC = Hippocampus, and PT = Putamen

interest are presented in Table 6.1 where the values of d shown in bold face indicate that the anisotropy index given on that row performs best in discriminating tissue classes on the corresponding column. We observe that our anisotropy index generally performs better in detecting differences among the tissues presented.

Table 6.1: Tissue detectability using GA and AI. The tissue name abbreviations are as described in Fig. 6.7

AI\ ROI	CC vs IC	CC vs TH	CC vs HC	CC vs PT	IC vs TH	IC vs HC	IC vs PT	TH vs HC	TH vs PT	HC vs PT
GA	0.69	0.74	0.53	0.77	**0.42**	**0.21**	0.54	**0.39**	0.36	0.56
AI	**0.81**	**1.48**	**0.73**	**0.96**	0.09	0.18	**0.59**	0.07	**0.44**	**0.63**

6.4 Conclusion

We presented a novel technique to model FOD fields as SPD HOT and estimated from DW-MRI data. The performance of the proposed method was compared against several existing FOD/ODF measures on a synthetic dataset with different noise levels and outperformed the other methods. We also demonstrated the use of our method on a real DT-MRI data obtained from a human brain dataset. Our results clearly demonstrate the superiority with which the organizational structure of an underlying diffusion process is neatly modeled with the CT-FOD field as compared to the ADC field and the fact that crossing, merging and bending of fibers are correctly depicted with the CT-FOD model. By deriving an anisotropy map directly from CT-FOD fields, we have consolidated the analysis of diffusion imaging towards the use of solely CT-FOD.

6.5 Contribution

1. Yonas T. Weldeselassie, Angelos Barmpoutis, and M. Stella Atkins. Symmetric Positive-Definite Cartesian Tensor Orientation Distribution Functions (CT-ODF). Medical Image Computing and Computer Assisted Intervention (MICCAI 2010). In Lecture Notes in Computer Science (LNCS), Vol. 6361, pages 582-589.

2. Yonas T. Weldeselassie, Angelos Barmpoutis, and M. Stella Atkins. Symmetric Positive-Definite Cartesian Tensor Fiber Orientation Distributions (CT-FOD). Submitted for review in the Journal of Medical Imaging.

Chapter 7

Conclusion

The field of medical image analysis has increased rapidly in importance over the past few years. New imaging modalities and improved technologies now allow the acquisition and measurement of ever more data of the human body. DW-MRI is one result of this rapid progress in medical imaging which is progressing toward clinical reality and which promises to have a major effect on the study of brain connectivity patterns in vivo. It is also a promising tool for the study of brain development.

In this thesis, we have developed theoretical and applied tools and algorithms for the processing and analysis of DT-MR images. The contributions of the thesis include better feature extraction using appropriate tensor similarity measures such as the development of our new anisotropy measure coined Shape Anisotropy, an extension of the graph cuts and Random Walker scalar image segmentation techniques to work directly on diffusion tensor field images, and a clinical application of DT-MRI to investigate various features of white matter fiber tracts extracted from DT-MR images in the cortico-striatal region of the brain in control and PD subjects.

We have shown that our shape anisotropy measures take consistently larger values than FA, providing a more detailed depiction of anisotropic areas. This implies the shape anisotropy measure provides additional information by revealing more white matter structures in the image which is also useful for fiber tractography purposes. In terms of noise immunity, the shape anisotropy measure gives comparable SNR to that of FA for small anisotropy levels but better SNR than FA as anisotropy level increases. Therefore shape anisotropy maps will generally be more robust to noise than the FA map, exhibiting little intensity variation within structures of uniform anisotropy. Importantly, the significance of

tensor distance based anisotropy measures is that it is straightforward to extend to higher order tensors.

Unlike extracting scalar features from DT-MR images and then performing segmentation on the extracted features, our graph cuts and Random Walker based segmentation tasks are performed directly on tensor images. This is useful because extracted features may be invariant to some transformation of the diffusion tensors. Graph cuts and Random Walker segmentation techniques are beneficial because they incorporate prior information in the form of hard constraints. This is useful in order to alter the segmentation task to get better results on the fly by adding more seeds. Moreover, unlike level-set based methods that are sensitive to several parameter tunings and that use gradient descent based methods that may end up stuck at local optimal solutions, graph cuts and Random Walker algorithms have few parameters to tune and are guaranteed to find the optimal solution for a given edge weighting tensor similarity measure.

Being part of the medical imaging research community, we also included a chapter on clinical application of DT-MRI and showed that we can extract useful features from diffusion tensors for the diagnosis of brain diseases such as PD. These features included anisotropy measures, diffusivity measures, geometric features of fiber tracts, and vector field features of major eigenvector directions along given fiber tracts.

In this rapidly expanding and exciting research field, it was not long before we noticed that the tools and algorithms developed earlier were not adequate and needed further work to model crossing, fanning, splitting and merging of fiber tracts. For this reason, we went a step further and developed a Cartesian tensor based FOD model to correctly depict crossing, fanning, splitting and merging of fiber tracts. The performance of our FOD method was compared against several existing FOD/ODF functions by measuring the deviation angles of computed fiber orientations from underlying ground truth orientations computed from a synthetic dataset with different noise levels and outperformed the other methods. Finally, we extended the classical anisotropy measures derived from 2^{nd} order diffusion tensors with one that is directly inferred from FOD utilizing appropriate tensor distance measures. Our anisotropy measure was compared against existing generalized anisotropy measures for the task of discriminating different tissues of a brain image and resulted in a better discrimination of tissues from different classes.

The future prospects of DW-MRI can not be overstated. It has already proved useful in the investigation of various brain diseases such as multiple sclerosis, schizophrenia, and PD.

Its ability to map brain neuronal connectivity in vivo holds the future of understanding the complex structure and functionality of human brain. Considering the speed at which the field is progressing, it won't be surprising to see a complete understanding of human brain anatomy and functionality using DW-MRI in the near future.

Bibliography

[1] I. Aganj, C. Lenglet, G. Sapiro, E. Yacoub, K. Ugurbil, and N. Harel. Reconstruction of the orientation distribution function in single-and multiple-shell q-ball imaging within constant solid angle. *Magnetic Resonance in Medicine*, 64(2):554–566, 2010.

[2] A.L. Alexander, K. Hasan, G. Kindlmann, D.L. Parker, and J.S. Tsuruda. A geometric analysis of diffusion tensor measurements of the human brain. *Magnetic Resonance in Medicine*, 44(2):283–291, 2000.

[3] D. C. Alexander, G. J. Barker, and S. R. Arridge. Detection and modeling of non-gaussian apparent diffusion coefficient profiles in human brain data. *Magnetic Resonance in Medicine*, 48(2):331–340, 2002.

[4] A.W. Anderson and J.C. Gore. Analysis and correction of motion artifacts in diffusion weighted imaging. *Magnetic Resonance in Medicine*, 32(3):379–387, 1994.

[5] V. Arsigny, P. Fillard, X. Pennec, and N. Ayache. Log-euclidean metrics for fast and simple calculus on diffusion tensors. *Magnetic Resonance in Medicine*, 56(2):411–421, 2006.

[6] H.E. Assemlal, D. Tschumperlé, L. Brun, and K. Siddiqi. Recent advances in diffusion mri modeling: Angular and radial reconstruction. *Medical image analysis*, 15(4):369–396, 2011.

[7] D. Atkinson, D.A. Porter, D.L.G. Hill, F. Calamante, and A. Connelly. Sampling and reconstruction effects due to motion in diffusion-weighted interleaved echo planar imaging. *Magnetic Resonance in Medicine*, 44(1):101–109, 2000.

[8] A. Barmpoutis, J. Ho, and B.C. Vemuri. Approximating symmetric positive semidefinite tensors of even order. *SIAM Journal on Imaging Sciences*, 5:434–464, 2012.

[9] A. Barmpoutis, M.S. Hwang, D. Howland, J.R. Forder, and B.C. Vemuri. Regularized positive-definite fourth order tensor field estimation from dw-mri. *Neuroimage*, 45(1):153–162, 2009.

[10] A. Barmpoutis and B.C. Vemuri. A unified framework for estimating diffusion tensors of any order with symmetric positive-definite constraints. In *IEEE International Symposium on Biomedical Imaging–ISBI*, pages 1385–1388. IEEE, 2010.

[11] A. Barmpoutis, B.C. Vemuri, T.M. Shepherd, and J.R. Forder. Tensor splines for interpolation and approximation of dt-mri with applications to segmentation of isolated rat hippocampi. *IEEE Transactions on Medical Imaging*, 26(11):1537–1546, 2007.

[12] P.J. Basser. Fiber-tractography via diffusion tensor mri (dt-mri). In *Proceedings of the 6th Annual Meeting ISMRM, Sydney, Australia*, volume 1226, 1998.

[13] P.J. Basser and D.K. Jones. Diffusion-tensor mri: theory, experimental design and data analysis–a technical review. *NMR in Biomedicine*, 15(7-8):456–467, 2002.

[14] P.J. Basser, J. Mattiello, and D. Le Bihan. Estimation of the effective self-diffusion tensor from the nmr spin echo. *Journal of Magnetic Resonance-Series B*, 103(3):247–254, 1994.

[15] P.J. Basser, J. Mattiello, and D. LeBihan. Mr diffusion tensor spectroscopy and imaging. *Biophysical Journal*, 66(1):259–267, 1994.

[16] P.J. Basser, S. Pajevic, C. Pierpaoli, J. Duda, and A. Aldroubi. In vivo fiber tractography using dt-mri data. *Magnetic Resonance in Medicine*, 44(4):625–632, 2000.

[17] P.J. Basser and C. Pierpaoli. Microstructural and physiological features of tissues elucidated by quantitative-diffusion-tensor mri. *Journal of Magnetic Resonance-Series B*, 111(3):209–219, 1996.

[18] P.G. Batchelor, M. Moakher, D. Atkinson, F. Calamante, and A. Connelly. A rigorous framework for diffusion tensor calculus. *Magnetic Resonance in Medicine*, 53(1):221–225, 2005.

[19] R. Bhatia. *Positive Definite Matrices*. Princeton University Press, 2007.

[20] C.R.V. Blain, G.J. Barker, J.M. Jarosz, N.A. Coyle, S. Landau, R.G. Brown, K.R. Chaudhuri, A. Simmons, D.K. Jones, and S.C.R. Williams. Measuring brain stem and cerebellar damage in parkinsonian syndromes using diffusion tensor mri. *Neurology*, 67(12):2199–2205, 2006.

[21] L. Bloy and R. Verma. On computing the underlying fiber directions from the diffusion orientation distribution function. In *Proceedings of Medical Image Computing and Computer-Assisted Intervention–MICCAI*, pages 1–8. Springer, 2008.

[22] Y.Y. Boykov and M.P. Jolly. Interactive graph cuts for optimal boundary and region segmentation of objects in n-d images. In *Proceedings of Eighth IEEE International Conference on Computer Vision–ICCV*, volume 1, pages 105–112. IEEE, 2001.

[23] M. Bozzali, A. Falini, M. Franceschi, M. Cercignani, M. Zuffi, G. Scotti, G. Comi, and M. Filippi. White matter damage in alzheimer's disease assessed in vivo using diffusion tensor magnetic resonance imaging. *Journal of Neurology, Neurosurgery & Psychiatry*, 72(6):742–746, 2002.

[24] A. Brun, H. Knutsson, H.J. Park, M. Shenton, and C.F. Westin. Clustering fiber traces using normalized cuts. *Medical Image Computing and Computer Assisted Intervention–MICCAI*, pages 368–375, 2004.

[25] M.S. Buchsbaum, P. Schoenknecht, Y. Torosjan, R. Newmark, K.W. Chu, S. Mitelman, A.M. Brickman, L. Shihabuddin, M.M. Haznedar, and E.A. Hazlett. Diffusion tensor imaging of frontal lobe white matter tracts in schizophrenia. *Annals of General Psychiatry*, 5:19, 2006.

[26] C. ChefdHotel, D. Tschumperlé, R. Deriche, and O. Faugeras. Constrained flows of matrix-valued functions: Application to diffusion tensor regularization. *Proceedings of European Conference on Computer Vision (ECCV)*, pages 251–265, 2002.

[27] T.L. Chenevert, J.A. Brunberg, and JG Pipe. Anisotropic diffusion in human white matter: demonstration with mr techniques in vivo. *Radiology*, 177(2):401, 1990.

[28] M.C. Chiang, A.D. Leow, A.D. Klunder, R.A. Dutton, M. Barysheva, S.E. Rose, K.L. McMahon, G.I. De Zubicaray, A.W. Toga, and P.M. Thompson. Fluid registration of diffusion tensor images using information theory. *IEEE Transactions on Medical Imaging*, 27(4):442–456, 2008.

[29] Y. Cointepas, C. Poupon, D. Le Bihan, and J.F. Mangin. A spin glass based framework to untangle fiber crossing in mr diffusion based tracking. *Medical Image Computing and Computer Assisted Intervention–MICCAI)*, pages 475–482, 2002.

[30] T.E. Conturo, N.F. Lori, T.S. Cull, E. Akbudak, A.Z. Snyder, J.S. Shimony, R.C. McKinstry, H. Burton, and M.E. Raichle. Tracking neuronal fiber pathways in the living human brain. *Proceedings of the National Academy of Sciences*, 96(18):10422, 1999.

[31] P.A. Cook, D.C. Alexander, and G.J.M. Parker. Modelling noise-induced fibre-orientation error in diffusion-tensor mri. In *IEEE International Symposium on Biomedical Imaging–ISBI*, pages 332–335. IEEE, 2004.

[32] E. Dahlhaus, D.S. Johnson, C.H. Papadimitriou, P.D. Seymour, and M. Yannakakis. The complexity of multiterminal cuts. *Journal of Society for Industrial and Applied Mathematics–SIAM on Computing*, 23(4):864–894, 1994.

[33] R. De La Fuente-Fernandez and A.J. Stoessl. The placebo effect in parkinson's disease. *Trends in Neurosciences*, 25(6):302–306, 2002.

[34] M. Descoteaux, E. Angelino, S. Fitzgibbons, and R. Deriche. A fast and robust odf estimation algorithm in q-ball imaging. In *Proceedings of the 3rd IEEE International Symposium on Biomedical Imaging–ISBI*, pages 81–84, 2006.

[35] M. Descoteaux, E. Angelino, S. Fitzgibbons, and R. Deriche. Regularized, fast, and robust analytical q-ball imaging. *Magnetic Resonance in Medicine*, 58(3):497–510, 2007.

[36] M. Descoteaux, R. Deriche, T.R. Knosche, and A. Anwander. Deterministic and probabilistic tractography based on complex fibre orientation distributions. *IEEE Transactions on Medical Imaging*, 28(2):269–286, 2009.

[37] A.G. Droogan, C.A. Clark, D.J. Werring, G.J. Barker, W.J. McDonald, and D.H. Miller. Comparison of multiple sclerosis clinical subgroups using navigated spin echo diffusion-weighted imaging. *Journal of Magnetic Resonance Imaging*, 17(5):653–661, 1999.

[38] C. Feddern, J. Weickert, and B. Burgeth. Level-set methods for tensor-valued images. In *Proceedings of Second IEEE Workshop on Variational, Geometric and Level Set Methods in Computer Vision*, pages 65–72, 2003.

[39] P. Fletcher and S. Joshi. Principal geodesic analysis on symmetric spaces: Statistics of diffusion tensors. *Computer Vision and Mathematical Methods in Medical and Biomedical Image Analysis*, pages 87–98, 2004.

[40] L.R. Ford and D.R. Fulkerson. Flow in networks. *Princeton University Press, Princeton, NJ*, 1962.

[41] A. Ghosh and R. Deriche. From second to higher order tensors in diffusion-mri. *Tensors in Image Processing and Computer Vision*, pages 315–334, 2009.

[42] A. Ghosh, R. Deriche, and M. Moakher. Ternary quartic approach for positive 4th order diffusion tensors revisited. In *Proceedings of the 6th IEEE International Symposium on Biomedical Imaging–ISBI*, pages 618–621, 2009.

[43] A. Ghosh, D. Wassermann, and R. Deriche. A polynomial approach for maxima extraction and its application to tractography in hardi. In *Information Processing in Medical Imaging–IPMI*, pages 723–734. Springer, 2011.

[44] A. Goh, C. Lenglet, P. Thompson, and R. Vidal. Estimating orientation distribution functions with probability density constraints and spatial regularity. *Medical Image Computing and Computer-Assisted Intervention–MICCAI*, pages 877–885, 2009.

[45] A.V. Goldberg and R.E. Tarjan. A new approach to the maximum-flow problem. *Journal of the Association for Computing Machinery (JACM)*, 35(4):921–940, 1988.

[46] L. Grady. Multilabel random walker image segmentation using prior models. In *IEEE Computer Society Conference on Computer Vision and Pattern Recognition–CVPR*, volume 1, pages 763–770. IEEE, 2005.

[47] L. Grady. Random walks for image segmentation. *IEEE Transactions on Pattern Analysis and Machine Intelligence*, 28(11):1768–1783, 2006.

[48] K.M. Hasan, A.L. Alexander, and P.A. Narayana. Does fractional anisotropy have better noise immunity characteristics than relative anisotropy in diffusion tensor mri? an analytical approach. *Magnetic Resonance in Medicine*, 51(2):413–417, 2004.

[49] K.M. Hasan, P.J. Basser, D.L. Parker, and A.L. Alexander. Analytical computation of the eigenvalues and eigenvectors in dt-mri. *Journal of Magnetic Resonance*, 152(1):41–47, 2001.

[50] M. Hedley, H. Yan, and D. Rosenfeld. Motion artifact correction in mri using generalized projections. *IEEE Transactions on Medical Imaging*, 10(1):40–46, 1991.

[51] A.I. Holodny, D.M. Gor, R. Watts, P.H. Gutin, and A.M. Uluğ. Diffusion-tensor mr tractography of somatotopic organization of corticospinal tracts in the internal capsule: Initial anatomic results in contradistinction to prior reports. *Radiology*, 234(3):649–653, 2005.

[52] T. Hosey, G. Williams, and R. Ansorge. Inference of multiple fiber orientations in high angular resolution diffusion imaging. *Magnetic Resonance in Medicine*, 54(6):1480–1489, 2005.

[53] B. Jian and B.C. Vemuri. Multi-fiber reconstruction from diffusion mri using mixture of wisharts and sparse deconvolution. In *Proceedings of the 20th International Conference on Information Processing in Medical Imaging-IPMI*, pages 384–395. Springer-Verlag, 2007.

[54] B. Jian, B.C. Vemuri, E. Özarslan, P.R. Carney, and T.H. Mareci. A novel tensor distribution model for the diffusion-weighted mr signal. *NeuroImage*, 37(1):164–176, 2007.

[55] F. Jiao, Y. Gur, C. Johnson, and S. Joshi. Detection of crossing white matter fibers with high-order tensors and rank-k decompositions. In *Information Processing in Medical Imaging–IPMI*, pages 538–549. Springer, 2011.

[56] D.K. Jones. *Diffusion MRI: Theory, methods, and applications*. Oxford University Press, 2010.

[57] DK Jones, MA Horsfield, and A. Simmons. Optimal strategies for measuring diffusion in anisotropic systems by magnetic resonance imaging. *Magnetic Resonance in Medicine*, 42:515–525, 1999.

[58] D.K. Jones, A. Simmons, S.C.R. Williams, and M.A. Horsfield. Non-invasive assessment of axonal fiber connectivity in the human brain via diffusion tensor mri. *Magnetic Resonance in Medicine*, 42(1):37–41, 1999.

[59] K.J. Jung and Z.H. Cho. Reduction of flow artifacts in nmr diffusion imaging using view-angle tilted line-integral projection reconstruction. *Magnetic Resonance in Medicine*, 19(2):349–360, 1991.

[60] J. Kärger, H. Pfeifer, and W. Heinik. Principles and application of self-diffusion measurements by nuclear magnetic resonance. *Advances in Magnetic Resonance*, 12:1–89, 1988.

[61] D. Kim and M. Kim. Combining functional and diffusion tensor mri. *Annals of the New York Academy of Sciences*, 1064(1):1–15, 2005.

[62] G. Kindlmann, R.S.J. Estepar, M. Niethammer, S. Haker, and C.F. Westin. Geodesic-loxodromes for diffusion tensor interpolation and difference measurement. In *Proceedings of the 10th international conference on Medical Image Computing and Computer Assisted Intervention*, volume I, pages 1–9. Springer-Verlag, 2007.

[63] M.A. Koch, D.G. Norris, and M. Hund-Georgiadis. An investigation of functional and anatomical connectivity using magnetic resonance imaging. *Neuroimage*, 16(1):241–250, 2002.

[64] V. Kolmogorov and R. Zabin. What energy functions can be minimized via graph cuts? *IEEE Transactions on Pattern Analysis and Machine Intelligence*, 26(2):147–159, 2004.

[65] R. Kumar, A. Barmpoutis, B.C. Vemuri, P.R. Carney, and T.H. Mareci. Multi-fiber reconstruction from dw-mri using a continuous mixture of von mises-fisher distributions. In *Proceedings of IEEE Computer Society Conference on Computer Vision and Pattern Recognition–CVPR*, pages 1–8, 2008.

[66] J. Kybic, P. Thévenaz, A. Nirkko, and M. Unser. Unwarping of unidirectionally distorted epi images. *IEEE Transactions on Medical Imaging*, 19(2):80–93, 2000.

[67] B.A. Landman, J.A.D. Farrell, C.K. Jones, S.A. Smith, J.L. Prince, and S. Mori. Effects of diffusion weighting schemes on the reproducibility of dti-derived fractional anisotropy, mean diffusivity, and principal eigenvector measurements at 1.5 t. *Neuroimage*, 36(4):1123–1138, 2007.

[68] C.L. Lawson and R.J. Hanson. *Solving Least Squares Problems, Chapter 23*, volume 15. Society for Industrial Mathematics, 1974.

[69] D. Le Bihan and P.J. Basser. Molecular diffusion and nuclear magnetic resonance. *Diffusion and Perfusion Magnetic Resonance Imaging*, pages 5–17, 1995.

[70] D. Le Bihan, J.F. Mangin, C. Poupon, C.A. Clark, S. Pappata, N. Molko, and H. Chabriat. Diffusion tensor imaging: concepts and applications. *Journal of Magnetic Resonance Imaging*, 13(4):534–546, 2001.

[71] D. Le Bihan, R. Turner, and P. Douek. Is water diffusion restricted in human brain white matter? an echo-planar nmr imaging study. *Neuroreport*, 4(7):887, 1993.

[72] A. Leemans, B. Jeurissen, J. Sijbers, and D.K. Jones. Exploredti: a graphical toolbox for processing, analyzing, and visualizing diffusion mr data. *17th Annual Meeting of International Society for Magnetic Resonance in Medicine (ISMRM)*, page 3537, 2009.

[73] S.E. Leh, A. Ptito, M.M. Chakravarty, and A.P. Strafella. Fronto-striatal connections in the human brain: a probabilistic diffusion tractography study. *Neuroscience Letters*, 419(2):113–118, 2007.

[74] C. Lenglet, M. Rousson, and R. Deriche. Segmentation of 3d probability density fields by surface evolution: Application to diffusion mri. *Medical Image Computing and Computer-Assisted Intervention–MICCAI*, pages 18–25, 2004.

[75] C. Lenglet, M. Rousson, R. Deriche, and O. Faugeras. Statistics on the manifold of multivariate normal distributions: Theory and application to diffusion tensor mri processing. *Journal of Mathematical Imaging and Vision*, 25(3):423–444, 2006.

[76] C. Lenglet, M. Rousson, R. Deriche, O. Faugeras, S. Lehericy, and K. Ugurbil. A riemannian approach to diffusion tensor images segmentation. *Proceedings of the 19th International Conference on Information Processing in Medical Imaging–IPMI*, pages 591–602, 2005.

[77] K.O. Lim, M. Hedehus, M. Moseley, A. de Crespigny, E.V. Sullivan, and A. Pfefferbaum. Compromised white matter tract integrity in schizophrenia inferred from diffusion tensor imaging. *Archives of General Psychiatry*, 56(4):367, 1999.

[78] J.F. Mangin, C. Poupon, C. Clark, D. Le Bihan, and I. Bloch. Distortion correction and robust tensor estimation for mr diffusion imaging. *Medical Image Analysis*, 6(3):191–198, 2002.

[79] J.F. Mangin, C. Poupon, Y. Cointepas, D. Riviere, D. Papadopoulos-Orfanos, CA Clark, J. Régis, and D. Le Bihan. A framework based on spin glass models for the inference of anatomical connectivity from diffusion-weighted mr data–a technical review. *NMR in Biomedicine*, 15(7-8):481–492, 2002.

[80] T. McGraw, B.C. Vemuri, Y. Chen, M. Rao, and T. Mareci. Dt-mri denoising and neuronal fiber tracking. *Medical Image Analysis*, 8(2):95–111, 2004.

[81] M. Moakher. A differential geometric approach to the geometric mean of symmetric positive-definite matrices. *SIAM Journal on Matrix Analysis and Applications*, 26(3):735–747, 2005.

[82] M. Moakher. Fourth-order cartesian tensors: Old and new facts, notions and applications. *The Quarterly Journal of Mechanics and Applied Mathematics*, 61(2):181–203, 2008.

[83] M. Moakher and A.N. Norris. The closest elastic tensor of arbitrary symmetry to an elasticity tensor of lower symmetry. *Journal of Elasticity*, 85(3):215–263, 2006.

[84] S. Mori, W.E. Kaufmann, G.D. Pearlson, B.J. Crain, B. Stieltjes, M. Solaiyappan, and P. Van Zijl. In vivo visualization of human neural pathways by magnetic resonance imaging. *Annals of Neurology*, 47(3):412–414, 2000.

[85] R.J. Ordidge, J.A. Helpern, Z.X. Qing, R.A. Knight, and V. Nagesh. Correction of motional artifacts in diffusion-weighted mr images using navigator echoes. *Journal of Magnetic Resonance Imaging*, 12(3):455–460, 1994.

[86] E. Özarslan and T.H. Mareci. Generalized diffusion tensor imaging and analytical relationships between diffusion tensor imaging and high angular resolution diffusion imaging. *Magnetic Resonance in Medicine*, 50(5):955–965, 2003.

[87] E. Özarslan, T.M. Shepherd, B.C. Vemuri, S.J. Blackband, and T.H. Mareci. Resolution of complex tissue microarchitecture using the diffusion orientation transform (dot). *NeuroImage*, 31(3):1086–1103, 2006.

[88] E. Özarslan, B.C. Vemuri, and T.H. Mareci. Generalized scalar measures for diffusion mri using trace, variance, and entropy. *Magnetic Resonance in Medicine*, 53(4):866–876, 2005.

[89] N.G. Papadakis, D. Xing, G.C. Houston, J.M. Smith, M.I. Smith, M.F. James, A.A. Parsons, C.L.H. Huang, L.D. Hall, and T.A. Carpenter. A study of rotationally invariant and symmetric indices of diffusion anisotropy. *Magnetic resonance imaging*, 17(6):881–892, 1999.

[90] X. Pennec, P. Fillard, and N. Ayache. A riemannian framework for tensor computing. *International Journal of Computer Vision*, 66(1):41–66, 2006.

[91] C. Pierpaoli, A. Barnett, S. Pajevic, R. Chen, L.R. Penix, A. Virta, and P. Basser. Water diffusion changes in wallerian degeneration and their dependence on white matter architecture. *Neuroimage*, 13(6):1174–1185, 2001.

[92] C. Pierpaoli, P. Jezzard, P.J. Basser, A. Barnett, and G. Di Chiro. Diffusion tensor mr imaging of the human brain. *Radiology*, 201(3):637–648, 1996.

[93] C. Poupon, B. Rieul, I. Kezele, M. Perrin, F. Poupon, and J.F. Mangin. New diffusion phantoms dedicated to the study and validation of high-angular-resolution diffusion imaging (hardi) models. *Magnetic Resonance in Medicine*, 60(6):1276–1283, 2008.

[94] W.H. Press, B.P. Flannery, S.A. Teukolsky, and W.T. Vetterling. *Numerical Recipes*, volume 547. Cambridge University Press, 1986.

[95] G.K. Rohde, A.S. Barnett, P.J. Basser, S. Marenco, and C. Pierpaoli. Comprehensive approach for correction of motion and distortion in diffusion-weighted mri. *Magnetic Resonance in Medicine*, 51(1):103–114, 2004.

[96] M. Rousson, C. Lenglet, and R. Deriche. Level set and region based surface propagation for diffusion tensor mri segmentation. *Computer Vision and Mathematical Methods in Medical and Biomedical Image Analysis*, pages 123–134, 2004.

[97] J. Rowe, K.E. Stephan, K. Friston, R. Frackowiak, A. Lees, and R. Passingham. Attention to action in parkinson's disease. *Brain*, 125(2):276, 2002.

[98] T. Schultz and H. Seidel. Estimating crossing fibers: A tensor decomposition approach. *IEEE Transactions on Visualization and Computer Graphics–TVCG*, 14(6):1635–1642, 2008.

[99] O. Söderman and B. Jönsson. Restricted diffusion in cylindrical geometry. *Journal of Magnetic Resonance. Series A*, 117(1):94–97, 1995.

[100] P. Staempfli, T. Jaermann, G.R. Crelier, S. Kollias, A. Valavanis, and P. Boesiger. Resolving fiber crossing using advanced fast marching tractography based on diffusion tensor imaging. *Neuroimage*, 30(1):110–120, 2006.

[101] E.O. Stejskal and J.E. Tanner. Spin diffusion measurements: spin echoes in the presence of a time-dependent field gradient. *The Journal of Chemical Physics*, 42(1):288, 1965.

[102] J. Talairach and P. Tournoux. Co-planar stereotaxic atlas of the human brain: 3-dimensional proportional system: an approach to cerebral imaging, 1988.

[103] H.C. Torrey. Bloch equations with diffusion terms. *Physical Review*, 104(3):563, 1956.

[104] J. Tournier, F. Calamante, and A. Connelly. Robust determination of the fibre orientation distribution in diffusion mri: non-negativity constrained super-resolved spherical deconvolution. *NeuroImage*, 35(4):1459–1472, 2007.

[105] J. Tournier, F. Calamante, D.G. Gadian, and A. Connelly. Direct estimation of the fiber orientation density function from diffusion-weighted mri data using spherical deconvolution. *NeuroImage*, 23(3):1176–1185, 2004.

[106] T.P. Trouard, Y. Sabharwal, M.I. Altbach, and A.F. Gmitro. Analysis and comparison of motion-correction techniques in diffusion-weighted imaging. *Journal of Magnetic Resonance Imaging*, 6(6):925–935, 1996.

[107] D.S. Tuch. Q-ball imaging. *Magnetic Resonance in Medicine*, 52(6):1358–1372, 2004.

[108] D.S. Tuch, T.G. Reese, M.R. Wiegell, and Van J.W. Diffusion mri of complex neural architecture. *Neuron*, 40(5):885–895, 2003.

[109] D.S. Tuch, R.M. Weisskoff, J.W. Belliveau, and V.J. Wedeen. High angular resolution diffusion imaging of the human brain. In *7th Annual Meeting of International Society for Magnetic Resonance in Medicine–ISMRM*, page 321, 1999.

[110] E.A.H. Von dem Hagen and R.M. Henkelman. Orientational diffusion reflects fiber structure within a voxel. *Magnetic Resonance in Medicine*, 48(3):454–459, 2002.

[111] Z. Wang and B.C. Vemuri. An affine invariant tensor dissimilarity measure and its applications to tensor-valued image segmentation. *Proceedings of IEEE Computer Society on Computer Vision and Pattern Recognition–CVPR*, 1:228–233, 2004.

[112] Z. Wang and B.C. Vemuri. Dti segmentation using an information theoretic tensor dissimilarity measure. *IEEE Transactions on Medical Imaging*, 24(10):1267–1277, 2005.

[113] Z. Wang, B.C. Vemuri, Y. Chen, and T.H. Mareci. A constrained variational principle for direct estimation and smoothing of the diffusion tensor field from complex dwi. *IEEE Transactions on Medical Imaging*, 23(8):930–939, 2004.

[114] V.J. Wedeen, P. Hagmann, W.Y.I. Tseng, T.G. Reese, and R.M. Weisskoff. Mapping complex tissue architecture with diffusion spectrum magnetic resonance imaging. *Magnetic Resonance in Medicine*, 54(6):1377–1386, 2005.

[115] V.J. Wedeen, T.G. Reese, D.S. Tuch, M.R. Weigel, J.G. Dou, R.M. Weiskoff, and D. Chessler. Mapping fiber orientation spectra in cerebral white matter with fourier transform diffusion mri. In *Proceedings of the 8th Annual Meeting of ISMRM, Denver*, page 82, 2000.

[116] J. Weickert and T. Brox. Diffusion and regularization of vector and matrix-valued images. *Contemporary Mathematics*, 313:251–268, 2002.

[117] Y.T. Weldeselassie, A. Barmpoutis, and M. S. Atkins. Symmetric positive-definite cartesian tensor orientation distribution functions (ct-odf). In *Medical Image Computing and Computer Assisted Intervention–MICCAI*, pages 582–589. Springer-Verlag, 2010.

[118] Y.T. Weldeselassie, G. Hamarneh, M.F. Beg, and M.S. Atkins. Novel decomposition of tensor distance into shape and orientation distances. In *Medical Image Computing and Computer-Assisted Intervention Workshop on Diffusion Modelling and the Fibre Cup (MICCAI DMFC)*, pages 173–180, 2009.

[119] M. Welk, C. Feddern, B. Burgeth, and J. Weickert. Median filtering of tensor-valued images. *Pattern Recognition*, pages 17–24, 2003.

[120] C.F. Westin, S.E. Maier, H. Mamata, A. Nabavi, F.A. Jolesz, and R. Kikinis. Processing and visualization for diffusion tensor mri. *Medical Image Analysis*, 6(2):93–108, 2002.

[121] M.R. Wiegell, D.S. Tuch, H.B.W. Larsson, and V.J. Wedeen. Automatic segmentation of thalamic nuclei from diffusion tensor magnetic resonance imaging. *NeuroImage*, 19(2):391–401, 2003.

[122] I. Yassine and T. McGraw. 4th order diffusion tensor interpolation with divergence and curl constrained bézier patches. In *Proceedings of the 6th IEEE International Symposium on Biomedical Imaging–ISBI*, pages 634–637, 2009.

[123] K. Yoshikawa, Y. Nakata, K. Yamada, and M. Nakagawa. Early pathological changes in the parkinsonian brain demonstrated by diffusion tensor mri. *Journal of Neurology, Neurosurgery & Psychiatry*, 75(3):481, 2004.

[124] W. Zhan, E.A. Stein, and Y. Yang. Mapping the orientation of intravoxel crossing fibers based on the phase information of diffusion circular spectrum. *NeuroImage*, 23(4):1358–1369, 2004.

[125] H. Zhang, P.A. Yushkevich, D.C. Alexander, and J.C. Gee. Deformable registration of diffusion tensor mr images with explicit orientation optimization. *Medical Image Analysis*, 10(5):764–785, 2006.

[126] H. Zhang, P.A. Yushkevich, and J.C. Gee. Registration of diffusion tensor images. In *Computer Vision and Pattern Recognition, 2004. CVPR 2004. Proceedings of the 2004 IEEE Computer Society Conference on*, volume 1, pages I–842. Ieee, 2004.

[127] S. Zhang and D. Laidlaw. Elucidating neural structure in diffusion tensor mri volumes using streamtubes and streamsurfaces. volume 9, pages 1–1, 2001.

[128] B. Zheng and J.C. Rajapakse. Time efficient dt-mri acquisition parameters for robust estimation of fiber tracts. *Journal of Signal Processing Systems*, 54(1):25–31, 2009.

[129] L. Zhukov, K. Museth, D. Breen, A.H. Barr, and R. Whitaker. Level set modeling and segmentation of diffusion tensor magnetic resonance imaging brain data. *Journal of Electronic Imaging*, 12:125–133, 2003.